# IMAGING A HYDRAULICALLY FRACTURED BAKKEN SHALE RESERVOIR USING 4D-TOMOGRAPHY AND REVERSE VSP TECHNIQUES WITH PERFORATION SHOT SOURCES

---

A Dissertation Presented to

the Faculty of the Department of Earth and Atmospheric Sciences

University of Houston

---

In Partial Fulfilment

of the Requirements for the Degree

Doctor of Philosophy

---

By

Alexandre Augusto Cardoso da Silva

August 2018

IMAGING A HYDRAULICALLY FRACTURED BAKKEN SHALE RESERVOIR USING 4D-TOMOGRAPHY AND REVERSE VSP TECHNIQUES WITH PERFORATION SHOT SOURCES

Alexandre Augusto Cardoso da Silva

APPROVED:

Dr. Robert R. Stewart, Committee Chair
Department of Earth and Atmospheric Sciences

Dr. Hua-Wei Zhou, Committee member
Department of Earth and Atmospheric Sciences

Dr. Aibing Li, Committee member
Department of Earth and Atmospheric Sciences

Dr. Guan Qin, Committee member
Petroleum Engineering Department

Dean
College of Natural Sciences and Mathematics

# Acknowledgements

In this journey of five years, I had the opportunity of meeting several generous and knowledgeable people to whom I am very grateful. Here, I acknowledge the importance that they had in my achievement.

First, I would like to thank my advisor Dr. Robert R. Stewart. Teaching is an act of generosity and devotion to the future generations and Dr. Stewart represents this class of professional who conjugates knowledge and kindness in this mission. Thank you, Dr. Stewart, for your patience and dedication.

Also, I would like to thank my company, the Petróleo Brasileiro S.A., for the financial support. Here, I should mention the names of my last 3 bosses: Mauro Becker, Daniel Steagall, and Jose Fernando Rosalba. They were very supportive and I appreciate their confidence in my work. Also, I would like to thank Vera Lucia Silva for her administrative support.

I also want to express my appreciation to the Hess Corporation for providing the Bakken Formation dataset used in my dissertation, especially Dr. Ted Dohmen, Dr. Keith Katahara, and Ms. Michele Simon. They were always ready for discussion and for helping all students that developed their studies using this dataset.

In this period, I also had the chance of making new friends. Most of them I met in the Allied Geophysics Laboratories (AGL). I would like to say thank you to them: Li, Jingjing, Andrea, Wenyuan, Suresh, Anoop, Jiannan, Hum, Nikolay, Joan, Yukai, Andrew, Ezzedeen, Carl, and Michael. All discussions that I had with them about my dissertation were very useful. Moreover, their friendships were remarkable.

I also would like to thank the members of my committee: Dr. Aibing Li, Dr. Hua-Wei Zhou, and Dr. Guan Qin. I really appreciate their time and the knowledge they shared with me throughout their comments.

I would like to thank some software companies. Their software packages were important tools in the construction of the dissertation: Ikon Science, Emerson-Paradigm, Schlumberger, and Matlab. I also used the codes developed by the Center for Wave Phenomena of the Colorado School of Mines and the Madagascar package. Especially, I would like to thank Dr. Edip Baysal, Gabriel Yelin, Orly Kletenik, Eyal Cohen (Emerson-Paradigm), and Sue Pritchett (Ikon Science).

We are always using the knowledge produced by other researchers to accomplish our own research. That been said, I would like to thank the former UH students Long Huang, Corbin Willian Crews II, and Duo Yuan. They worked with the same Bakken Formation dataset that I used and their findings were very helpful in the interpretation of my results.

I want to thank Elita Selmara de Abreu for sharing this journey with me as well.

Also, I want to thank my second family in the U.S.: Andrea e Odival. Their generosity and kindness are rare nowadays.

Also, I want to express how grateful I am to Karen Nogueira. She was the solid base which supported me through the hardest time that I had during my research. She renounced a lot of things to help me.

And this dissertation is dedicated to my father, mother, and brothers. Their role in my life goes much beyond my career. My resilience to accomplish all goals in my life comes from what I learned with them.

# IMAGING A HYDRAULICALLY FRACTURED BAKKEN SHALE RESERVOIR USING 4D-TOMOGRAPHY AND REVERSE VSP TECHNIQUES WITH PERFORATION SHOT SOURCES

---

An Abstract of a Dissertation

Presented to

the Faculty of the Department of Earth and Atmospheric Sciences

University of Houston

---

In Partial Fulfilment

of the Requirements for the Degree

Doctor of Philosophy

---

By

Alexandre Augusto Cardoso da Silva

August 2018

# Abstract

Hydrocarbon production from shale reservoirs varies considerably from one location to another in the same well. This variation can be due to geologic factors but also due to variabilities in the reservoir' stimulation. Seismic images may be inconclusive in identifying areas where hydraulic fractures have penetrated and microseismic events can have uncertainties in their location and description. I propose the use of perforation shots to map regions where hydraulic stimulation was more effective using P- and SV-wave direct arrivals emitted by the shots.

First, I introduce a method to calculate the moment when shots were triggered, the zero-time. For that, I use shot depths, velocity variance, and P- and SV-wave direct-arrival traveltime differences with an approximates a hyperbolic moveout solution.

After testing this method with synthetic data, it was applied to real data acquired in the Bakken Formation of the Williston Basin (North Dakota). Using eighty shots triggered in two producer wells and recorded by six vertical wells, I calculated the P-wave fastest azimuth yielding approximately N70$^{o}$E using a reverse VSP walkaround technique. Two high-frequency 2D seismic images of the overburden layers with a dominant frequency of roughly 300 Hz were obtained. Their dimensions are about 600 m high and 1200 m long. In stacked oil shale plays, the perforation shots can provide high-frequency images with a clear gain in seismic resolution and interpretability.

A 3D grid-based anisotropic tomography procedure was conducted to estimate P-velocity variations. The variations point to a reduction of 3% in the P-velocity after fracturing and suggest that fracturing causes seismically observable changes. The region where the P-velocity was reduced is irregularly distributed but, apparently, the areas with the largest P-velocity reduction are more productive. Stages associated with natural fractures show almost no P-velocity reduction. Thus, perforation shots can provide compelling opportunities to seismically identify hydraulically fractured regions.

# Contents

# List of Figures

# List of Tables

# Chapter 1

# Introduction

## 1.1 MOTIVATION

The rise of oil prices during the 2000s and early 2010s spurred the exploration of oil in tight reservoirs which under lower prices would not be economically feasible due to their low permeability and porosity. The unproven reserves of oil and gas associated with black shale (i.e. shales with high organic matter content) is widespread in the world. Figure 1.1 shows the distribution of various shale formations which potentially can be explored (U.S. Energy Information Administration, 2013). According to the Energy Information Administration of U.S., with data range from 2013 to 2015, available for 46 countries, the unproved technically recoverable reserves of wet shale gas and tight oil in the world were 7,576.6 Tcf and 418.9 billion bbl, respectively. From these total reserves, 622.6 Tcf and 78.2 billion bbl were located in U.S. Although the shale extent in the world is promising regards to the possibility of production, in 2014, only four countries were

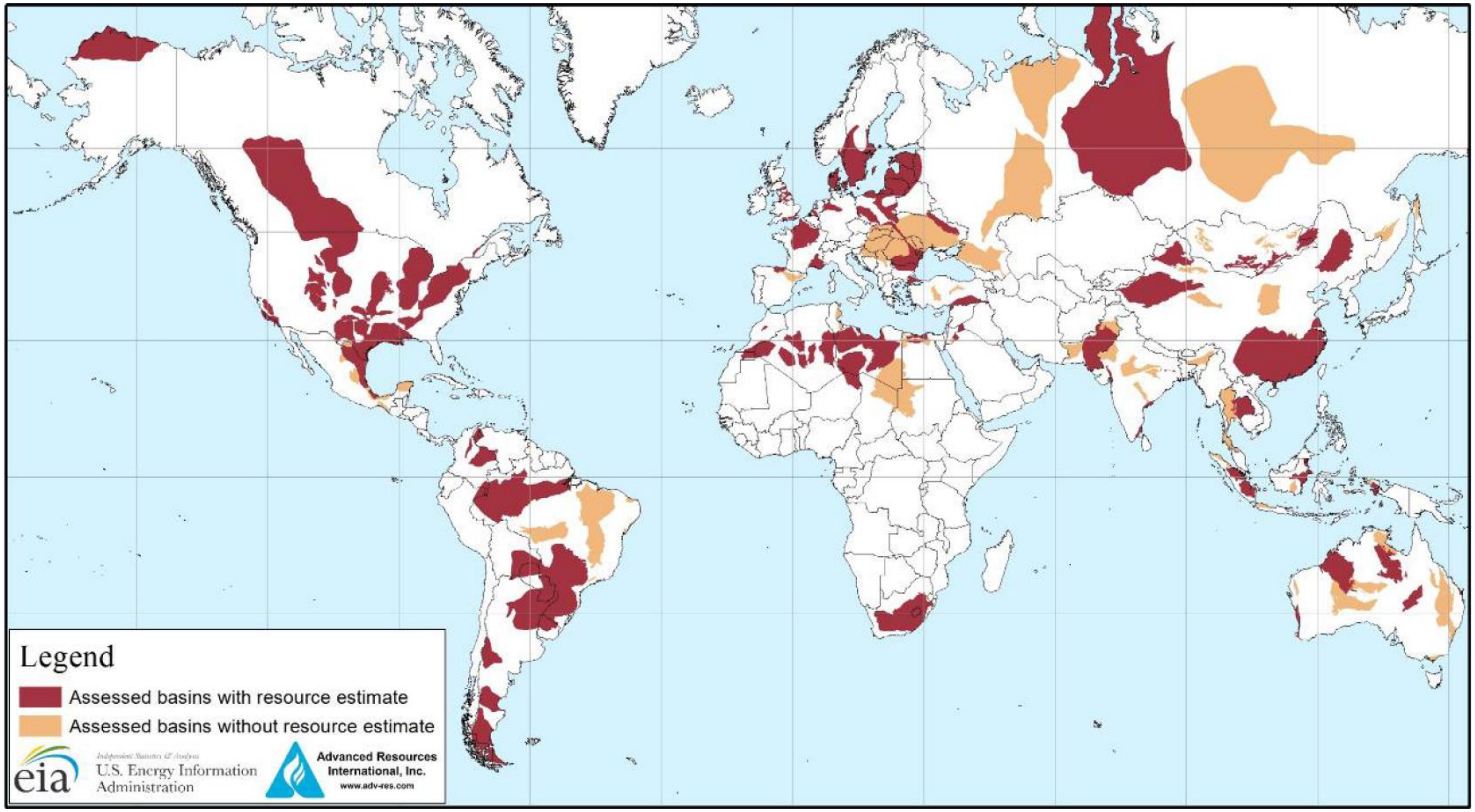


Figure 1.1: World assessed basin map with and without shale oil and shale gas resource estimate (modified from U.S. Energy Information Administration, Technically Recoverable Shale Oil and Shale Gas Resources, 2013).

commercially producing hydrocarbons, either of shale gas or tight oil, namely: United States, Canada, China, and Argentina. Figure 1.2 shows their production at that time (U.S. Energy Information Administration, 2015). The reasons for the concentration of production in these countries lie, mainly, in the presence of the infrastructure and logistics needed to support a high level of activity which requires the ability to rapidly drill and complete a large number of wells. Therefore, the capacity to access drilling equipment quickly and to deliver the final product to consumers seems to be essential for economic shale production, as evidenced in the United States, Canada, and China, and to some extent, Argentina but not in other countries.

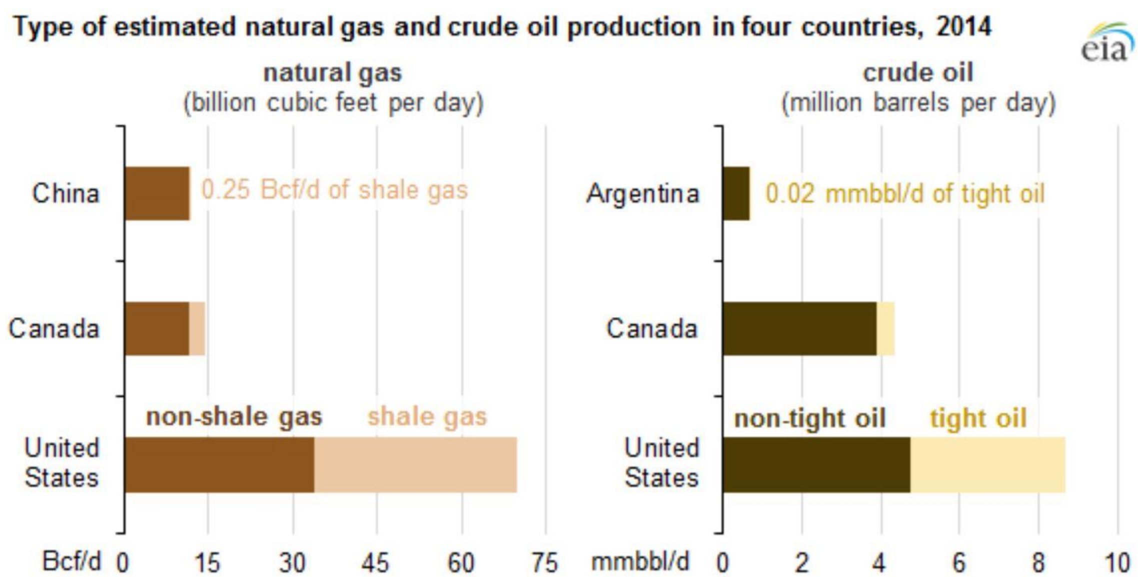


Figure 1.2: Natural gas and crude oil production in shale or tight formations of the only four countries producing commercially in 2014 (modified from U.S. Energy Information Administration, Shale gas and tight oil are commercially produced in just four countries, 2015).

Figure 1.3 shows the current and prospective shale plays, associated with sandstones or carbonates in 48 lower states of the United States. The production of the three more prolific basins, Eagle Ford, Bakken, and Permian regions, as they were in early 2018, is shown. The production from tight oil and shale gas has increased in USA

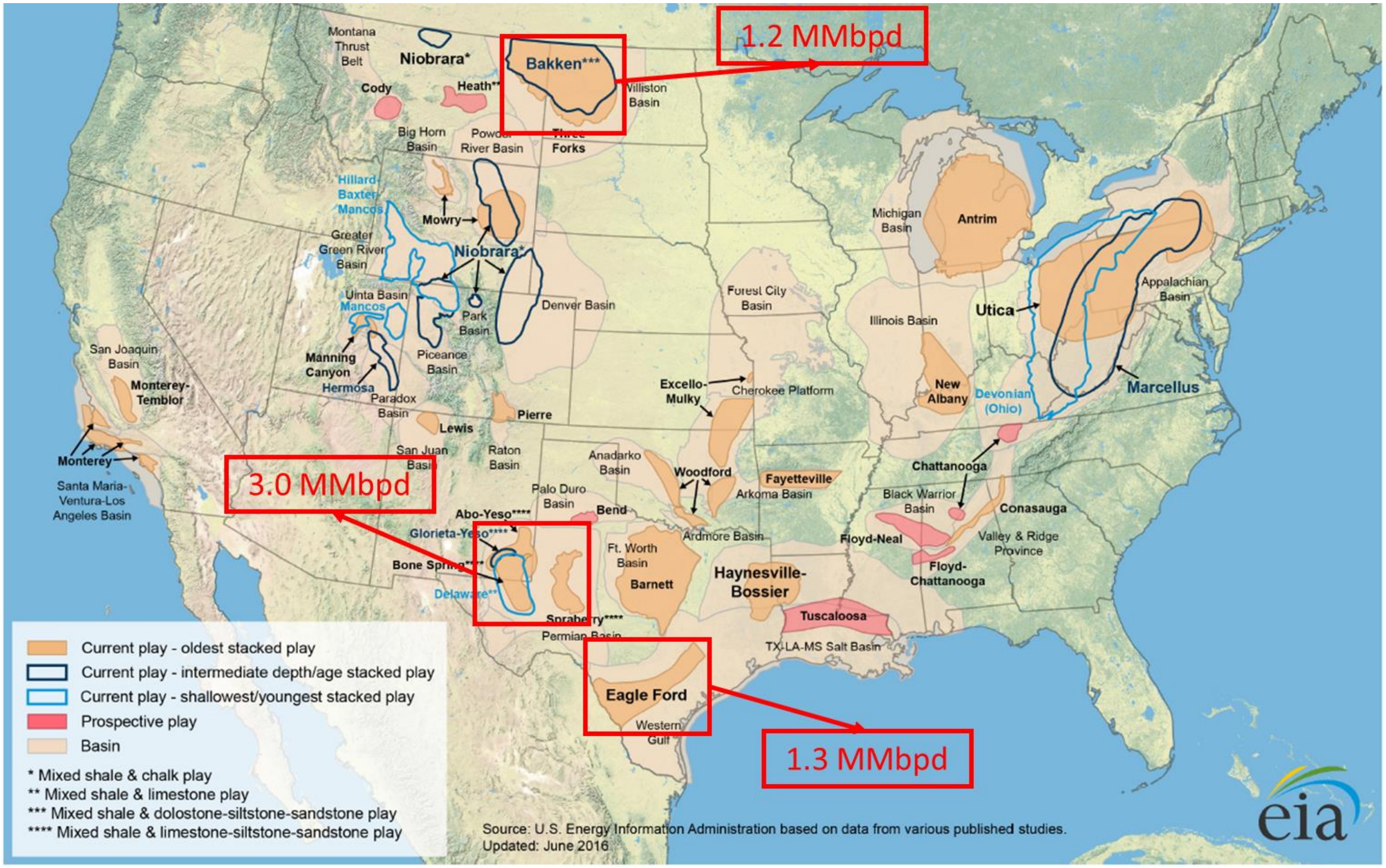


Figure 1.3: Shale gas and tight oil plays in the lower 48 states of U.S. with the production levels in early 2018 within the Bakken, Eagle Ford, and Permian basins (modified from U.S. Energy Information Administration, 2016).

(Figure 1.4). At the beginning of 2018, 53% of the crude oil production within the USA came from tight oil resources (U.S. Energy Information Administration, 2018). Three basins contribute around 85% of the tight oil production: the Western Gulf (Eagle Ford Formation), Williston (Bakken Formation), and Permian basins (mainly Wolfcamp, Bonespring, and Spraberry formations). The low porosity and permeability that

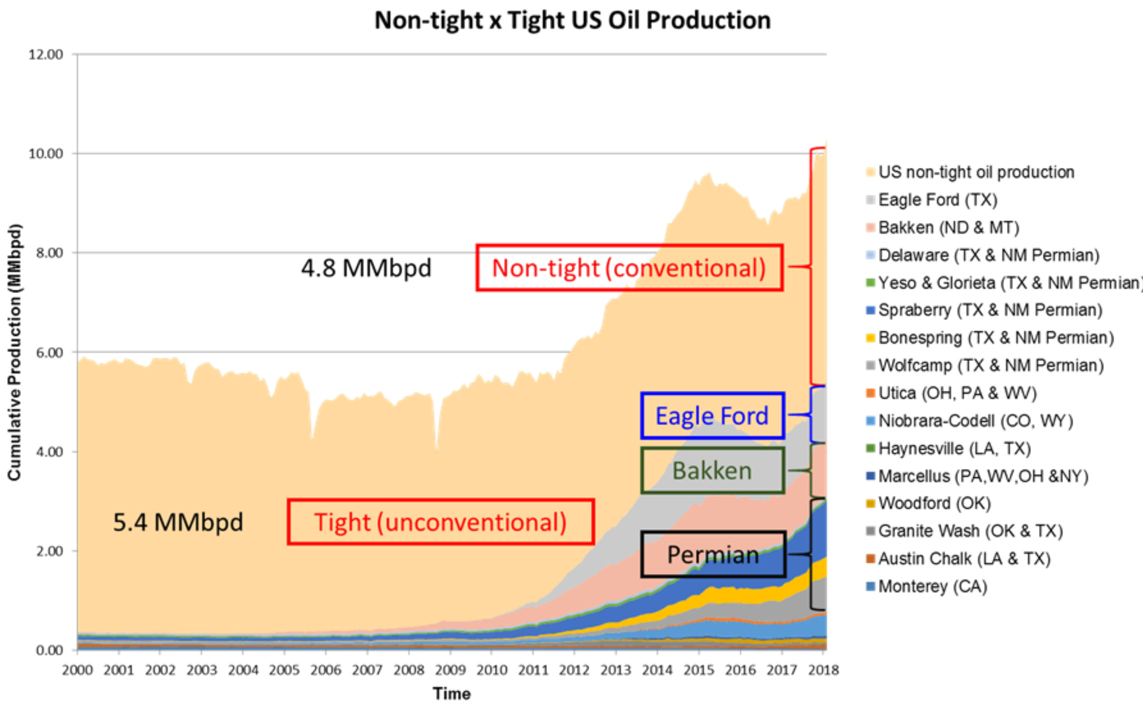


Figure 1.4: Plot shows the U.S. total oil production split between non-tight and tight reservoirs, considering the lower 48 states and Alaska. Most of the tight reservoir production is concentrated in 3 basins: Eagle Ford, Bakken, and Permian basins (modified from U.S. Energy Information Administration, 2018).

characterize these reservoirs (King, 2010; Maxwell, 2014) makes necessary the stimulation of these tight formations to improve their hydrocarbon productivity. Figure 1.5 shows the increase in the productivity of the wells within their first month of production in the three basins already mentioned. The Figure shows the production of an average rig considering only the first month of production of all wells which came online

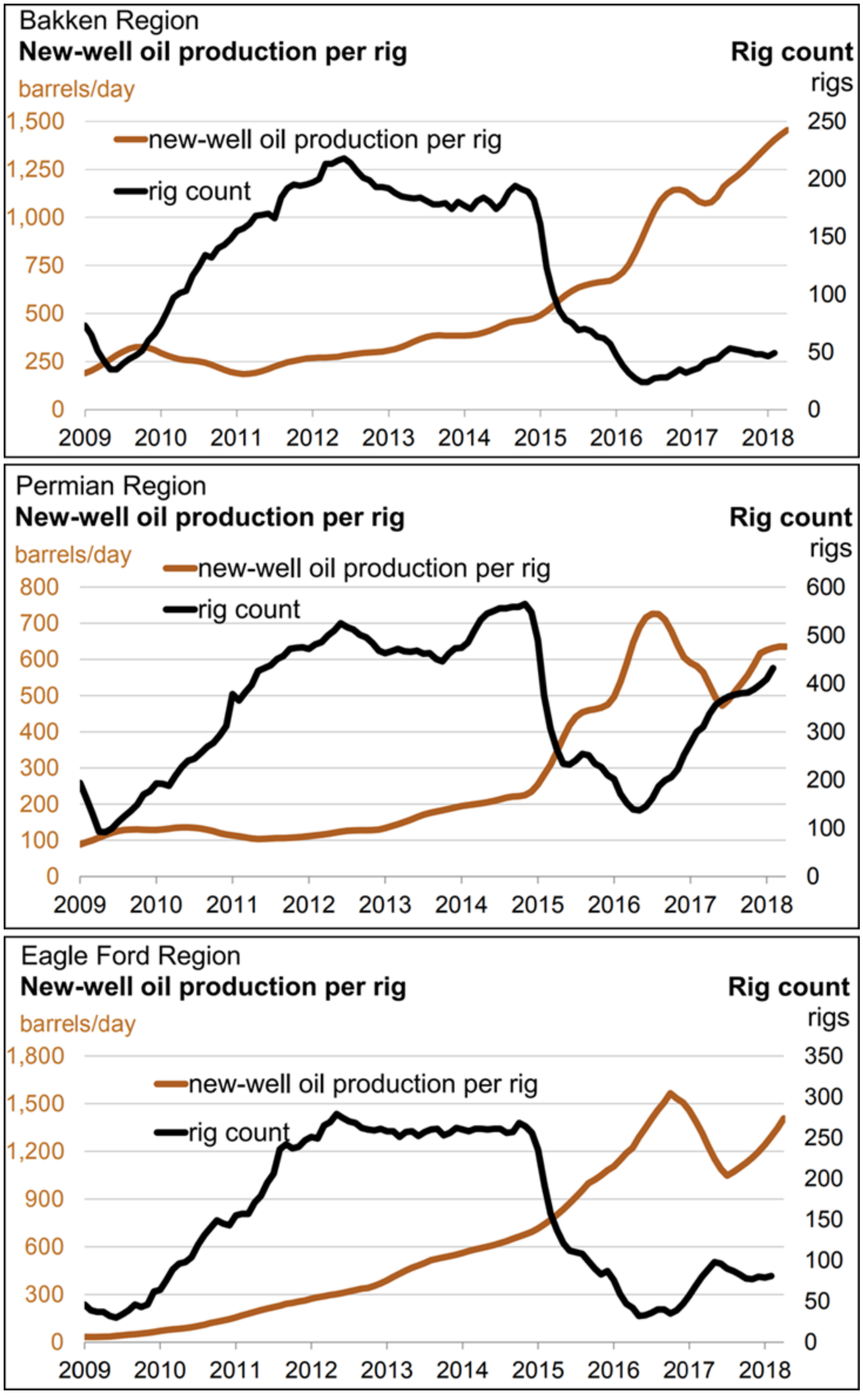


Figure 1.5: Plot showing the average amount of barrels produced per day per rig of the average well's first-month production in Bakken, Permian, and Eagle Ford regions from 2009 to 2018. The number of rigs is also shown (modified from U.S. Energy Information Administration, Drilling Productivity Report – April/2018, 2018a).

during that month. Year by year, the initial production per rig in Bakken, Permian, and Eagle Ford regions has steadily increased. The exception is the period after the drop of the oil's price in 2014 which caused the decrease in the number of rigs, leading to the reduction of productivity between 2016 and 2017 (U.S. Energy Information Administration, 2018a). Two techniques have been responsible for the enhancement of

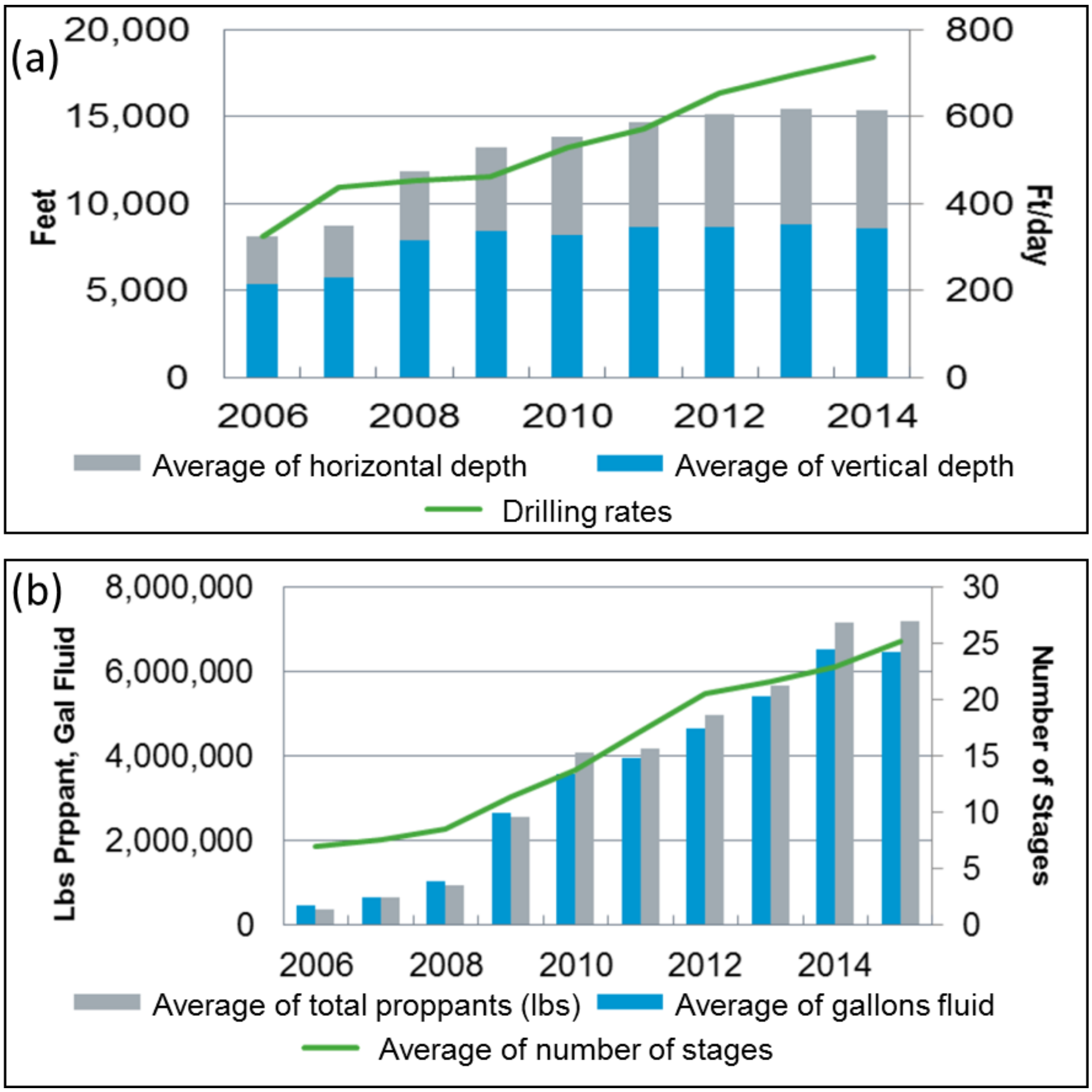


Figure 1.6: a) Average of horizontal and vertical length drilled per well and the drilling rates from 2006 to 2014. b) Average of proppant, gallons of fluids, and number of stages per well from 2006 to 2015 (modified from U.S. Energy Information Administration, Trends in U.S. oil and Natural gas upstream costs, 2016a).

this productivity: the drilling of longer horizontal wells and the hydraulic fracturing of the shale formation along these lateral wells. Figures 1.6a and 1.6b show the increase in the length of the horizontal section of the producers, also called lateral, and the increase of the number of hydraulically fractured stages within the laterals from 2006 to 2015 (U.S. Energy Information Administration, 2016a). These techniques increase the permeability of the rocks allowing the hydrocarbons to flow.

Figure 1.7 shows a schematic diagram of the horizontal drilling and the hydraulic fracturing process. After the drilling, wells are cased and the completion carries out the perforation of the casing, putting the formation in contact with the tubing which allows for the hydraulic fluids and proppant to penetrate the formation, fracturing it, and stimulating of the reservoir. It is not well understood yet how the fractures hydraulically created and the proppant (sand grains, well selected, of a specific grain size which is typically made of silica or ceramic) injected into the shale formation are distributed along the rocks, how exactly they increase the rock permeability, and how they would change the elastic properties of these rocks.

Perforation shots are small explosive charges, triggered at each well stage of treatment, which are used to perforate the casing creating a communication between the inner area of the tubing and the oil/gas bearing formation. This path is used to conduct the hydraulic fluids and proppants into the formation, promoting the initial break in the rocks helping to propagate the fractures into the shale. After stimulation of the formation, the hydrocarbons flow into the tubing through this communication.

To better understand how the shale formations and surrounding areas change as consequence of the hydraulic fracturing, I use the perforation shots to map possible changes in the P-wave rock velocity before and after the formation has been fractured.

My objective is to relate these changes in velocities with the stimulated area around the hydraulic fractured stages.

Perforation shots are widely used to calibrate P and S velocity models for microseismic location events (Maxwell, 2014; Akram and Eaton, 2013). These shots, in

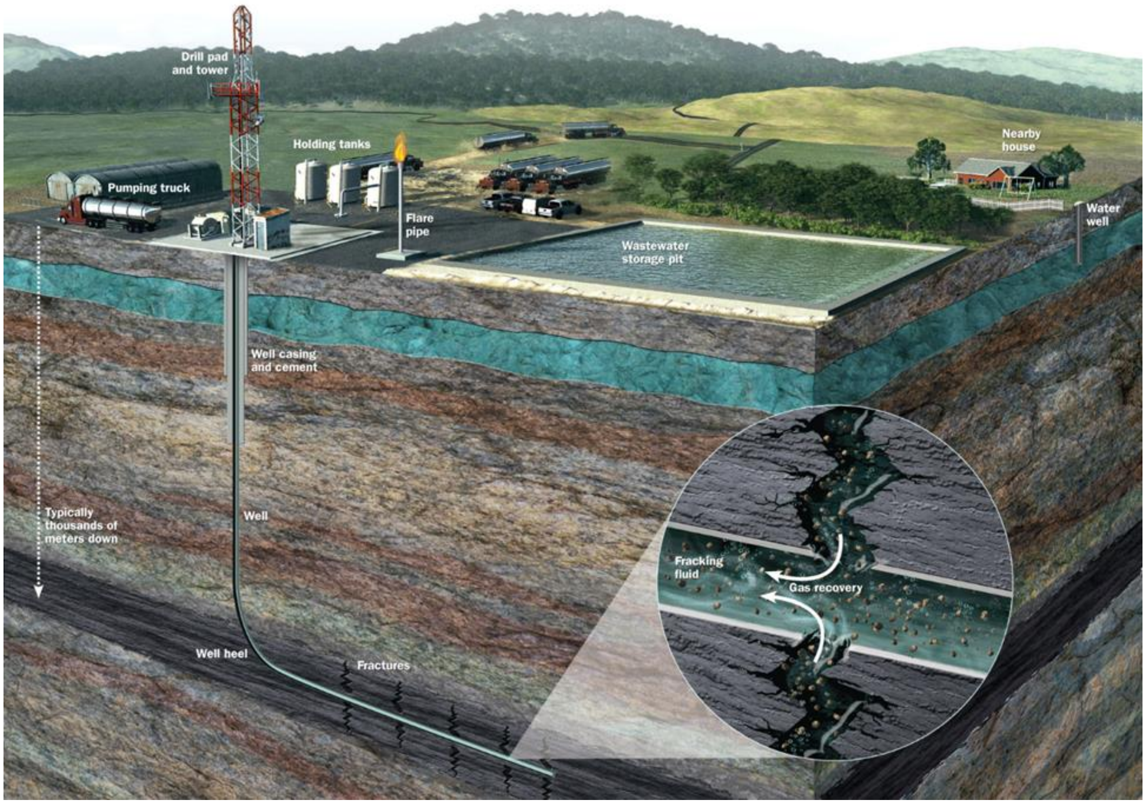


Figure 1.7: Schematic diagram of a perforation and drilling of a horizontal well. The fracturing process and the proppant placement are highlighted. Facilities, as the pumping trucks and wastewater storage pit, are also represented (modified from Green Plug District, 2016).

general, are used simultaneously to constrain an iterative inversion process in which an original velocity model, derived from well logs, is modified until a minimal threshold error in the spatial positions of the shots is achieved. Since the origin time of the perforation shots (the time when the perforation shots were triggered) are not accurately measured, their use to calibrate the velocity model may introduce uncertainties due to the characteristic trade-off between time and velocity within the inversion process. In the second chapter, I introduce a new method to calculate their origin times using one modified version of hyperbolic moveout correction equation (Taner and Koehler, 1969) which is a good approximation, even for anisotropic media, if shots are approximately located sub-vertically below the receivers, i. e. when shot and receivers show a small horizontal distance between them compared to the vertical distance between them (Tsvankin and Grechka, 2011).

Obtaining the origin time allows us to use the absolute traveltime of the P-wave created by perforation shots as seismic sources. In Chapter 3, I show the results of 2D Vertical Seismic Profile (VSP) walk-away and 3D VSP walk-around studies, using 80 perforation shots as seismic sources triggered in a microseismic acquisition survey conducted in Bakken shale, located in Williston Basin, North Dakota. They were recorded by six vertical observation wells during the fracturing of several stages of two horizontal wells. The results helped to characterize the anisotropic behavior of the overlying layers in the study area, showing changes in the anisotropic parameters which can be associated with the hydraulic fracturing of the horizontal wells. Also, the preferential fast velocity (P-wave) direction was calculated.

In Chapter 4, an anisotropic tomography study is conducted using the perforation shots located in one of the horizontal wells. The use of the tomographic technique is adequate to spatially pinpoint velocity variations that can be correlated to the fractures created in the hydraulic fracturing or natural fractures that may have been reactivated in the study area. Also, the microseismic events within the study area can be correlated with local velocity variations. These correlations and sections of velocity changes after the hydraulic fracturing jobs have been carried out and are shown in this chapter.

In Chapter 5, the perforation shots are used to image the overburden reflectors just above the reservoir, processing the data according to 2D VSP walkaway processing flow. Two 2D images were produced using the perforation shots of one horizontal well recorded simultaneously by two other vertical wells. One of the images showed discontinuities similar to fractures, located close to microseismic events which were identified within the overburden. Moreover, the dominant frequency of the images obtained using the perforation shots showed a value 3 times higher (approximately 300 Hz) compared to the dominant frequency achieved by the surface seismic acquisition in the area. Although only a limited area was imaged with the perforation shots, this area is of fundamental importance since geomechanical modeling of near overburden layers requires mapping of faults/fractures and thickness of thin layers which may have an important role in the hydraulic fractures propagating upwards.

The characterization of the overburden velocity model and the imaging of fractures near the reservoir can help to calculate an accurate velocity to locate the microseismic events triggered during the hydraulic fracturing of the stages and also help to identify zone where natural fractures may be present, diverting the hydraulic fluids to the upper formations, decreasing the efficiency of the formation fracturing.

## 1.2 DATASET AND SOFTWARE

The dataset used in this study includes eighty perforation shots in two horizontal wells, H2 and H3. The well logs include the P- and S-sonic (fast and slow), the gamma-ray, and the density logs from six vertical wells. In addition, the pore pressure profiles of the Bakken Formation collected in the six vertical wells and the horizontals H2 and H3 were available. The full-stack 3D surface P-wave seismic data and the P-wave zero-offset Vertical Seismic Profile (VSP) data acquired at the vertical well V3 were used for velocity calibration and interpretation purposes. Microseismic events acquired during the hydraulic fracturing of 29 and 38 stages in the wells H2 and H3, respectively, were used for interpretation. An early horizontal producer well, H1, had produced in the area, for 2.5 years, before the other two producers were drilled.

In the development of the algorithm for the origin time calculation of the perforation shots, the main software used was Matlab (Chapter 2). The calculation of the P-wave fast direction and the Thomsen anisotropic parameters via VSP walkaround and walkaway techniques were carried out using the RokDoc software from Ikon Science Company (Chapter 3). For the VSP anisotropic tomography studies, the main software used was the VSP 3D Grid-based Anisotropic Tomography algorithm, from Emerson-Paradigm Company (Chapter 4). For the VSP walkaway seismic images results, the software used was the VISTA Desktop Seismic Data Processing software from Schlumberger Company (Chapter 5). For data visualization and initial tomography models of the P- and S-waves and density data, the software used was Petrel, also from Schlumberger. For seismic modeling, both Emerson-Paradigm Software Suite and Madagascar open-source package were used (Chapter 3 and 5).

### 1.3 DISSERTATION OUTLINE

This dissertation is divided into four main chapters plus a final chapter with the conclusions summarizing the results. In Chapter 2, I develop a new method to calculate the zero-time of the perforation shots. After a theoretical review of the development of the hyperbolic and nonhyperbolic equations for the moveout correction of seismic data, I show the derivation of my method and its use with synthetic data to evaluate how accurate it is when applied to isotropic and anisotropic synthetic models. In Chapter 3, perforation shots of Bakken shale field data were used, after have their zero-time calculated, to perform the 2D walk-away analysis, searching for the $\epsilon$, and $\delta$ Thomsen parameters before and after the hydraulic fracturing along one of the horizontal wells and the 3D walk-around analysis to calculate the P-wave velocity fast direction which may be correlated to the fracture strike of the natural or hydraulic fractures. In the fourth chapter, a tomography study is conducted in order to identify P-velocity variations which were correlated to the presence of natural or hydraulic created fractures within the overburden of the study area. In the fifth chapter, the perforation shots were used to image the overlying layers in search of fractures which may be correlated to microseismic events identified within the overburden. Two 2D images were produced showing a high-frequency content than the surface seismic acquired at the area. In Chapter 6, I summarize the results achieved in the other chapters and stating some conclusions about them.

# Chapter 2

## Finding the zero-time of the perforation shots

The use of perforation shots to communicate the well´s tubing to the formation's fluids is a method widely adopted in the completion of producer wells in unconventional reservoirs. The actual explosion times of the perforation shots are not routinely measured. However, the zero-time of each perforation shot is needed in our analyses.

The calculation of the zero-time of the perforation shot using the hyperbolic moveout equation, presented here, lies in its capacity to predict accurately the relationship between the squared two-way traveltime and the squared offset (equation 2.3), at least for offset values similar to the target depth values (Tsvankin, 2005). Among other issues, two aspects can reduce the accuracy of hyperbolic moveout equation, namely, the vertical heterogeneity and anisotropy. In this chapter, I will present the method used to calculate zero-time of the perforation shots and test it in different conditions of anisotropy and offset values with two layered models to assess how reliable it is. Another noteworthy aspect is that the hyperbolic moveout equation was initially thought to solve reflection data, not the direct arrival data provided by the perforation shots (Figure 2.1). Although this does not change the hyperbolic relationship between the traveltime and offset, for sake of simplicity, a multiplication by two of the traveltime and offset values is necessary to keep the equation applicable. Of course, the division of the results of the zero-time values found has to be done to convert the final results to one-way traveltime values.

The next sections will cover some theoretical background of the derivation of the hyperbolic normal moveout (NMO) equation and show how the Vertical Transverse Isotropic (VTI) model affects the NMO equation. Thereafter, I show the effects of vertical heterogeneity on the NMO equation. Some tests using synthetic data show the accuracy

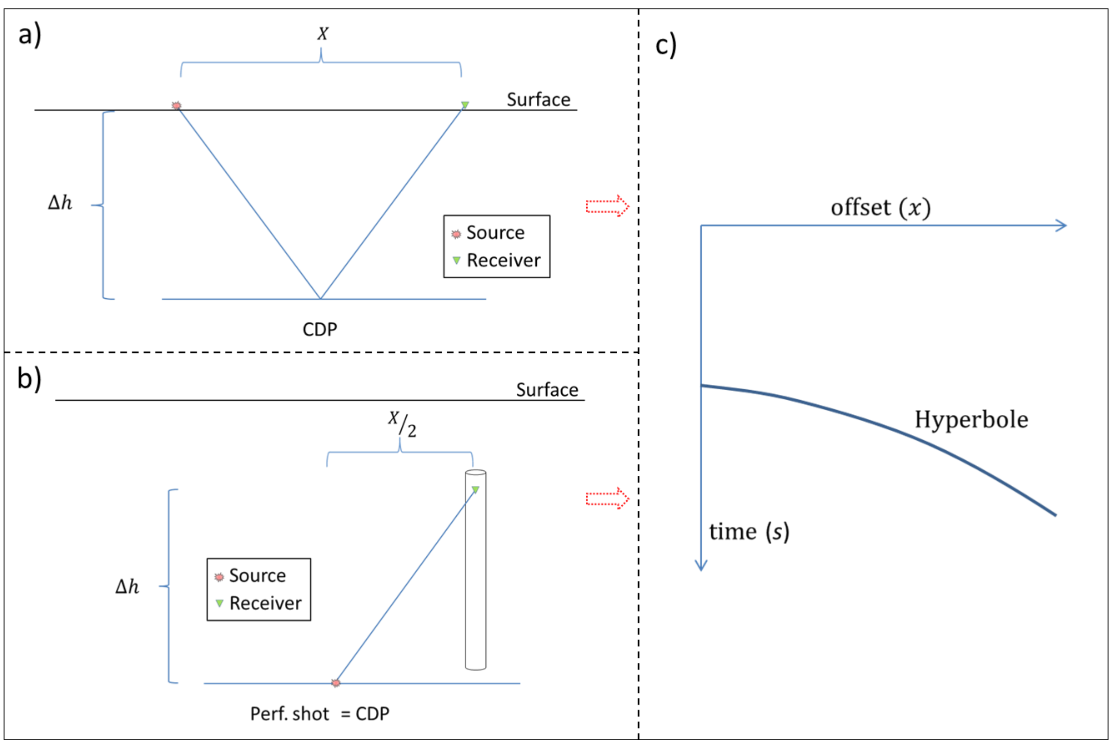


Figure 2.1: Scheme of the surface seismic acquisition (a), the perforation shot acquisition (b), and the characteristic hyperbole curve which is obtained when several traveltime and offset combinations are cross plotted in both cases. The hyperbolic correlation is exact for a homogeneous and isotropic medium. The elements in the scheme are the offset (*x*), the depth of the target (*Δh*), and the common depth point (CDP) which represents the imaged point in the surface seismic acquisition case.

of the zero-time calculation for perforation shots located at distinct offsets from the receiver array. The synthetic examples include one isotropic horizontally layered model and four different scenarios of VTI horizontally layered model.

## 2.1 HYPERBOLIC EQUATION AND THE NORMAL MOVEOUT CORRECTION

The time normal moveout (NMO) correction in an isotropic medium for pure modes (P- or S-waves which do not show any conversion from one mode to another) can be approximated by a Taylor series expansion near the vertical with the seismic data organized in common-midpoint (CMP) gathers (Taner and Koehler, 1969):

$$t^2 = A_0 + A_2 x^2 + A_4 x^4 + \cdots, \tag{2.1}$$

where $x$ is the source-receiver offset and the other terms are described as

$$A_0 = t_0^2, \qquad A_2 = \left.\frac{d(t^2)}{d(x^2)}\right|_{x=0}, \qquad A_4 = \left.\frac{1}{2}\frac{d}{d(x^2)}\left[\frac{d(t^2)}{d(x^2)}\right]\right|_{x=0}; \tag{2.2}$$

where the $t_0$ is the two-way zero-offset traveltime.

As described in Tsvankin and Thomsen (1994), for the isotropic case with horizontal layering, and source-receiver offset smaller than depth of the imaged reflector, Equation 2.1 can be simplified, dropping the quartic term and assuming that the second term is equal to the reciprocal of the NMO velocity ($V_{nmo}$) which leads to the hyperbolic function below:

$$t_{hyp}^2 = t_0^2 + \frac{x^2}{V_{nmo}^2}, \tag{2.3}$$

$$V_{nmo}^2 = \frac{1}{A_2} = \left.\frac{d(x^2)}{d(t^2)}\right|_{x=0} . \tag{2.4}$$

For isotropic media and source-receiver offset limited to the depth of the imaged reflector, the NMO hyperbolic Equation 2.3 is accurate enough to describe the squared reflection time as a function of the squared value of source-receiver offset ($t^2 - x^2$).

For anisotropic media, if the anisotropy of the formation is strong, the hyperbolic equation may not describe accurately enough the $(t^2 - x^2)$ relationship for source-receiver offset larger than the reflector depth. Next, the effects of anisotropy on the hyperbolic equation and on the $V_{nmo}$, for P- and S-wave modes, are explained for the anisotropic the Vertical Transverse Isotropic (VTI) model.

## 2.2 EFFECTS OF VTI ANISOTROPY IN THE HYPERBOLIC EQUATION AND $\mathbf{V_{nmo}}$

The VTI anisotropic model (Figure 2.2) is defined by a vertical axis of rotational symmetry perpendicular to horizontal layers. Planes which contain the symmetry axis are the planes of mirror symmetry and the planes parallel to the horizontal layering are called isotropy planes since the phase velocity of any mode (velocity measured along the vector which is perpendicular to the wavefront), propagating parallel to the horizontal layering, is independent of the propagation azimuth. In the VTI model, due to the geometric relation between its elements of symmetry, the phase velocities of different modes are only dependent on the angle between the phase-velocity vector and the symmetry axis, being azimuthally independent. It is the most common model used to explain the anisotropic behavior of sedimentary rocks, being frequently associated with shale formations (intrinsically anisotropic) or with the intercalation of isotropic thin layers (thinner than the dominant wavelength) with different elastic properties (Tsvankin, 2005).

The stiffness matrix, which defines the material properties and relates the stress with the strain tensor, for the VTI medium is defined by five independent coefficients and is given by

$$\boldsymbol{c}^{(VTI)} = \begin{pmatrix} c_{11} & c_{11}-2c_{66} & c_{13} & 0 & 0 & 0 \\ c_{11}-2c_{66} & c_{11} & c_{13} & 0 & 0 & 0 \\ c_{13} & c_{13} & c_{33} & 0 & 0 & 0 \\ 0 & 0 & 0 & c_{55} & 0 & 0 \\ 0 & 0 & 0 & 0 & c_{55} & 0 \\ 0 & 0 & 0 & 0 & 0 & c_{66} \end{pmatrix}. \tag{2.5}$$

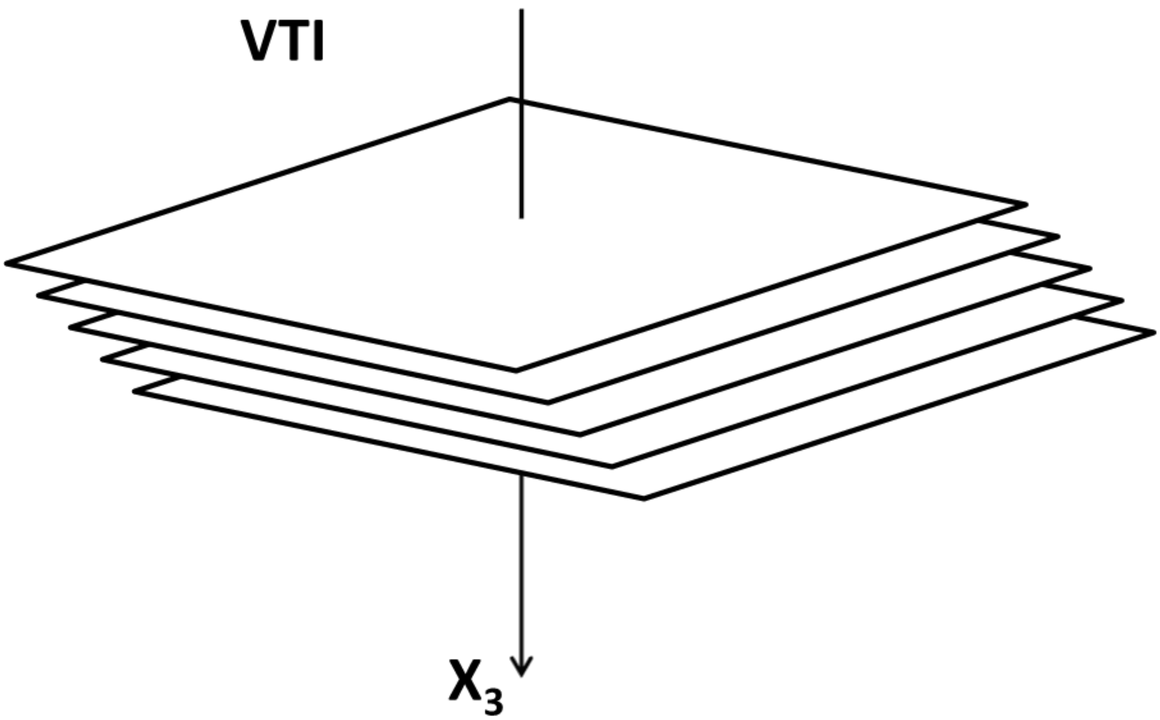


Figure 2.2: Model representing the VTI anisotropic case. The $X_3$ axis is the symmetry axis normal t the horizontal layers, so called isotropy planes (modified from Tsvankin, 2005).

Thomsen (1986) introduced a notation which condenses the anisotropic signature, expressed in the stiffness matrix, of the 3 wave modes (P-, SV- and SH-wave) for a VTI medium. This notation assumes that the anisotropic character is mild (weak anisotropic). Using Thomsen notation the anisotropic phase velocities of the 3 modes can be described by the P and S vertical velocities ($V_{P0}$ and $V_{S0}$) and three dimensionless anisotropy parameters, so called $\epsilon$, $\delta$, and $\gamma$ defined below as function of stiffness coefficients and density $\rho$:

$$V_{P0} \equiv \sqrt{\frac{c_{33}}{\rho}}, \tag{2.6}$$

$$V_{S0} \equiv \sqrt{\frac{c_{55}}{\rho}}, \tag{2.7}$$

$$\epsilon \equiv \frac{c_{11}-c_{33}}{2c_{33}}, \tag{2.8}$$

$$\gamma \equiv \frac{c_{11}-c_{33}}{2c_{33}}, \tag{2.9}$$

$$\delta \equiv \frac{(c_{13}+c_{55})^2-(c_{33}-c_{55})^2}{2c_{33}(c_{33}-c_{55})}, \tag{2.10}$$

Using the Thomsen notation, the P- and SV-wave velocities can be described by 3 parameters ($V_{P0}$, $\epsilon$, and $\delta$ for P-wave and $V_{S0}$, $\epsilon$, and $\delta$ for SV-wave) rather than 4 stiffness coefficients ($c_{11}$, $c_{33}$, $c_{55}$, and $c_{13}$. Similarly, SH-wave can be defined by only two parameters: $V_{S0}$ and $\gamma$.

Tsvankin (1995) showed, for a single and horizontal VTI layer, that $V_{nmo}$ for P- ($V_{nmo,P}$), SV- ($V_{nmo,SV}$), and SH-wave ($V_{nmo,SH}$) are defined as

$$V_{nmo,P} = V_{P0}\sqrt{1+2\delta}, \tag{2.11}$$

$$V_{nmo,SV} = V_{S0}\sqrt{1+2\sigma}, \tag{2.12}$$

$$V_{nmo,SH} = V_{P0}\sqrt{1+2\gamma}, \tag{2.13}$$

$$\sigma \equiv \left(\frac{V_{P0}}{V_{S0}}\right)^2 (\epsilon-\delta). \tag{2.14}$$

Although the NMO velocities equations above are defined as function of Thomsen parameters, they are valid for VTI media with arbitrary anisotropy strength, not just limited to the weak anisotropy case. Also, it is clear that seismic-derived stacking velocities cannot be directly used for time-to-depth conversion without incurring a depth error in an anisotropic VTI medium (Tsvankin, 1995).

The change in the phase velocity due to the anisotropic effect represented by the Thomsen parameters ($\epsilon$, $\delta$, and $\gamma$) and by the angle of the ray propagation, θ, (the angle that the seismic ray makes with the vertical axis of symmetry, the so-called polar angle), can be observed when the equations defined by Thomsen (1986), for weak anisotropy approximation in VTI media (single layer), are analyzed. The P, SV, and SH velocities, for a VTI medium, according to the weak anisotropy approximation theory, are shown below:

$$V_{P(\theta)} \approx V_{P0}(1+\delta \sin^2\theta \cos^2\theta + \varepsilon \sin^4\theta), \tag{2.15}$$

$$V_{SV(\theta)} \approx V_{S0}(1+\sigma \sin^2\theta \cos^2\theta), \tag{2.16}$$

$$V_{SH(\theta)} \approx V_{S0}(1+\gamma \sin^2\theta). \tag{2.17}$$

From the equations above, it can be seen that the smaller the propagation angle, i.e. the closer to the vertical axis, the smaller is the contribution of the anisotropy effects leading to the $V_P = V_{P0}$ and $V_S = V_{S0}$ which reduce the VTI medium to the isotropic case. Also, it can be seen that for $V_P$ the $\delta$ parameter has a larger weight when the ray is propagating close to the vertical plane while $\varepsilon$ has a stronger effect for rays traveling close to the horizontal plane. For $V_{SV}$, the effect of $\sigma$ is dependent on the difference $(\epsilon - \delta)$ rather than their individual values. Also, the anisotropic effect is amplified by the $\left(\frac{V_{P0}}{V_{S0}}\right)^2$ term, making, in most of the cases, the anisotropic effect on $V_{SV}$ larger than those observed on $V_P$. For $V_{SH}$, since the anisotropic effect is only dependent on $\gamma$, this means that its velocity is related to only two parameters, $V_{S0}$ and $\gamma$, leading its wavefront to assume an elliptical form in a homogeneous medium.

The effects of the anisotropy on the two-way time reflection are more clearly seen at larger offsets (offset larger than target depth). When long offsets are available, the nonhyperbolic behavior of the $t^2 - x^2$ relationship becomes visible, which requires the addition of the quartic term in the hyperbolic Equation 2.3 as it is seen below:

$$t^2 = t_0^2 + \frac{x^2}{V_{nmo}^2} + A_4 x^4. \tag{2.18}$$

Al-Dajani and Tsvankin (1998) showed that the quartic term can be described as a function of the Thomsen parameters, the vertical velocities, and the two-way zero-offset traveltimes for all three modes in VTI media as:

$$A_{4,P} = -\frac{2(\epsilon-\delta)(1+\frac{2\delta}{f})}{t_{P0}^2 V_{P0}^4 (1+2\delta)^4}, \tag{2.19}$$

$$A_{4,SV} = -\frac{2\sigma(1+\frac{2\delta}{f})}{t_{S0}^2 V_{S0}^4 (1+2\sigma)^4}, \tag{2.20}$$

$$A_{4,SH} = 0. \tag{2.21}$$

As it is shown, while the nonhyperbolic behavior of P- and SV-wave is proportional to $(\epsilon - \delta)$ difference, the SH-wave is hyperbolic for a VTI medium.

Another example of a nonhyperbolic equation for the moveout correction of P-wave in the VTI media is presented by Alkhalifah and Tsvankin (1995):

$$t^2 = t_{P0}^2 + \frac{x^2}{V_{nmo}^2} - \frac{2\eta x^4}{V_{nmo}^2 [t_{P0}^2 V_{nmo}^2 + (1+2\eta)x^2]}, \tag{2.22}$$

$$\eta \equiv \frac{\epsilon-\delta}{1+2\delta}. \tag{2.23}$$

The new parameter $\eta$ is the so called anellipticity. The Alkhalifah-Tsvankin equation is widely used for P-wave seismic time-processing with $\eta$ and $V_{nmo}$ controlling the P-wave two-way time reflection for vertically heterogeneous VTI medium.

The anisotropic equations above were defined considering a single VTI layer. The application of these equations in layered media requires the calculation of the effective quartic term, combining the effect of the layering itself and the anisotropy. Tsvankin and Thomsen (1994) derived the Equation 2.24 for the calculation of the effective quartic term in a 2D VTI model of N layers which is shown below:

$$A_4 = \frac{V_{nmo}^4 t_0 - \sum_{i=1}^{N} \left(V_{nmo}^{(i)}\right)^4 t_0^{(i)}}{4 V_{nmo}^8 t_0^3} + \frac{\sum_{i=1}^{N} A_4^{(i)} \left(V_{nmo}^{(i)}\right)^8 \left(t_0^{(i)}\right)^3}{V_{nmo}^8 t_0^3}, \tag{2.24}$$

where $t_0^{(i)}$ is the interval vertical traveltime and $V_{nmo}^{(i)}$ and $A_4^{(i)}$ are the NMO velocity and quartic term for the layer $i$, respectively.

In the case of an SV-wave, the effect of the anisotropy in the reflection traveltime, for a single layer VTI model, can be grasped analyzing the equation below also introduced by Tsvankin and Thomsen (1994):

$$t^2 = t_{S0}^2(1-2\sigma) + \frac{x^2}{V_{S0}^2} \tag{2.25}$$

where σ is defined by equation 2.14. It can be seen that the squared two-way SV-wave traveltime depends on P- and S-wave vertical velocities ratio, while the same is not true for squared two-way P-wave traveltime.

A similar analysis of the effects of the orthorhombic anisotropy in the hyperbolic equation and NMO velocity is shown in the Appendix A of this dissertation.

## 2.3 EFFECTS OF THE VERTICAL HETEROGENEITY IN THE HYPERBOLIC EQUATION

Since the location of a perforation shot is known, equations that calculate the two-way hyperbolic traveltime using this information have a clear advantage. It would be also convenient if the two-way hyperbolic time calculation used the average velocity instead of the NMO velocity as the former velocity is easier to obtain using well log or checkshots data. Blias (2007) introduced a new version of the normal moveout (NMO) correction including these characteristics. It is shown below:

$$t(x) = \sqrt{\frac{t_0^2 + \frac{x^2}{V_{ave}^2}}{1 + \frac{gx^2}{t_0^2 V_{ave}^2 (g+1)}}} \tag{2.26}$$

where $t_0$ is the two-way zero-offset traveltime, $V_{ave}$ is the average vertical velocity, $x$ is the offset, and $g$, the so-called the vertical heterogeneity factor, is given by the equation below:

$$g = \frac{V_{RMS}^2}{V_{ave}^2} - 1 \tag{2.27}$$

where $V_{RMS}$ is root-mean squared (RMS) velocity. The equations for $V_{ave}$ and $V_{RMS}$ are shown below:

$$V_{ave} = \frac{H}{\sum_{k=1}^{n} \Delta t_k} \tag{2.28}$$

$$V_{RMS}^2 = \frac{\sum_{k=1}^{n} \Delta t_k V_k^2}{\sum_{k=1}^{n} \Delta t_k} \tag{2.29}$$

where $\Delta t_k$.is the one-way traveltime in the *k*-th layer, $V_k$.is the interval velocity in the *k*-th layer (for any pure mode), and $H$.is the depth of the target.

Here, it is important to explain some aspects of the $g$ factor. As described by Taner and Koehler (1969), the normal moveout equation 2.3 is exact only for vertically and horizontally homogeneous media, although, for acquisition geometries where the offset is approximately equal to the depth of the target, the equation´s accuracy remains. Al-Chalabi (1973) introduced the $g$ term as a function of $V_{RMS}$ and $V_{ave}$ in order to compensate the vertical heterogeneity in the normal moveout equation. According to the equation 2.27, if the $V_{RMS}$ is equal to $V_{ave}$, the $g$ value goes to zero, meaning that there is no heterogeneity (the layer is vertically homogeneous).

The effect of the vertical heterogeneity can be understood analyzing the Figure 2.3. It can be seen that the non-vertical ray tends to travel through a longer path in the layer with the faster velocity (red arrow) leading to a higher average velocity. If the velocity contrast between the two contiguous layers is smaller, the value of the refraction angle would be smaller and the difference in the path length, along the faster layer, between a vertical ray and an oblique ray would be smaller as well. Therefore, the velocity contrast and the incidence angle of the rays are the main factors which influence average velocity for each ray, requiring the $g$ parameter in order to correct them.

Since the equation 2.26 is a function of the $V_{ave}$, it is possible to calculate the two-way traveltime as a function of the target's depth which is convenient since the depth of perforation shot is known. Blias (2007) also introduced the two-way NMO equation as a function of the target´s depth written below:

$$t(x) = t_0 \sqrt{\frac{4H^2+x^2}{4H^2+\frac{g}{g+1}x^2}} \qquad (2.30)$$

where $\mathrm{t}$ is the two-way traveltime, $\mathrm{t}_0$ is the zero-offset two-way traveltime, $\mathrm{H}$ is the depth of the target, $x$ is the offset and $g$ is the vertical heterogeneity of the P- or S-waves (pure

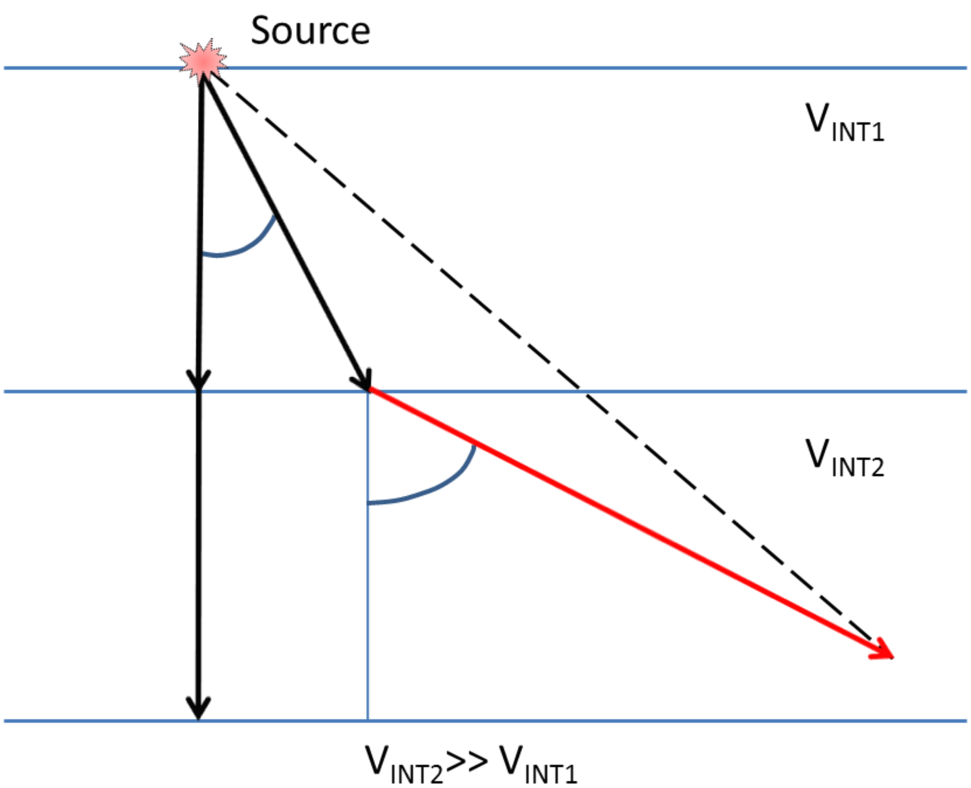


Figure 2.3: Scheme showing the difference between the total traveltime between the oblique and vertical rays. This difference depends on the velocity contrast between the layers and the incident angle. The larger the contrast, the faster is the ray since its raypath along the faster layer is longer. The dashed line represents the shorter straight path without the bending of the ray (modified from Taner et al., 2005).

waves). This equation is the main equation for the zero-time calculation which will be discussed in the next section.

## 2.4 PERFORATION SHOT GEOMETRY ACQUISITION AND ZERO-TIME PERFORATION SHOT CALCULATION

A typical geometry for microseismic acquisition uses vertical wells with geophones placed close to the formation which will be fractured. Such geometry helps to improve the signal-to-noise ratio of the low-energy events which, otherwise, would not be recorded (Maxwell, 2014).

Also, along with the microseismic acquisition, the seismic waves triggered by the perforation shots are acquired. Perforation shots are necessary to create a communication between the oil-bearing formation and the inner part of the well casing, making possible the oil to flow up to the surface. They consist of a certain number of explosive charges which are triggered from the surface by the perforation crew before the hydraulic fracture starts. The total number of explosive charges depends on the perforation equipment specifications. Numbers from 3 to 21 charges per foot for each gun system are commonly used. More than one gun system can be used per stage. The charges may be phased by some angle ($30^o$ and $60^o$ for example), creating a diagonal line of perforations along the borehole wall (Figure 2.4). The stages are defined along the horizontal part of the producer and the total number of stages is an important aspect of the final cost of the hydraulic fracture process. The total length of the horizontal section of the producer is also an important variable in the definition of the total number of stages, but the rule for the companies is to maximize the production with the smallest number of fractured stages.

Here, it is noteworthy to explain one aspect of the standard seismic acquisition and compare it to the perforation shot acquisition. In a standard seismic acquisition, the moment when the seismic source is triggered (zero-time) is precisely recorded, making possible the determination of the total traveltime for each trace acquired. This is done using a sensor which tells the recording system when the source is triggered, initiating the recording of the seismic data. In the case of the perforation shot acquisition, the zero-time, in most cases, is not recorded. Although some initiatives have been described in the literature (Maxwell, 2014), the zero-time recording is not usual and would demand some developments in the perforation shot equipment. Maybe, in the future, perforation shot and seismic crews may find a technical solution for that issue, if the importance of the zero-time acquisition becomes proved, but this is not a routine procedure yet.

Figure 2.5 shows a schematic diagram of perforation shot acquisition using geophones placed in a vertical well and a shot placed along a horizontal well. It is shown, in this figure, that the direct arrival of P- and S-waves (pure modes waves), issued by the source, is acquired by several geophones located at different levels (Figure 2.5a). Also, note that all direct arrivals, regardless the geophone which records them, have the same time origin, i.e. the same zero-time, since that all of them were originated from the same source. Given a velocity structure, one can calculate the unknown zero-time using the difference in time between P- and S-waves direct arrivals to calculate the total traveltime from the source to the receiver and subtract this total traveltime from the absolute time, measured in the field. In the case where P- and S-waves are recorded by several geophones, this calculation becomes a minimization problem of several equations (Figure 2.5b) whose goal is to find the best $t_0$ that minimizes the difference between the field measurement, i.e. the P- and S-wave traveltime differences measured at each receiver level (brackets in left side of minus

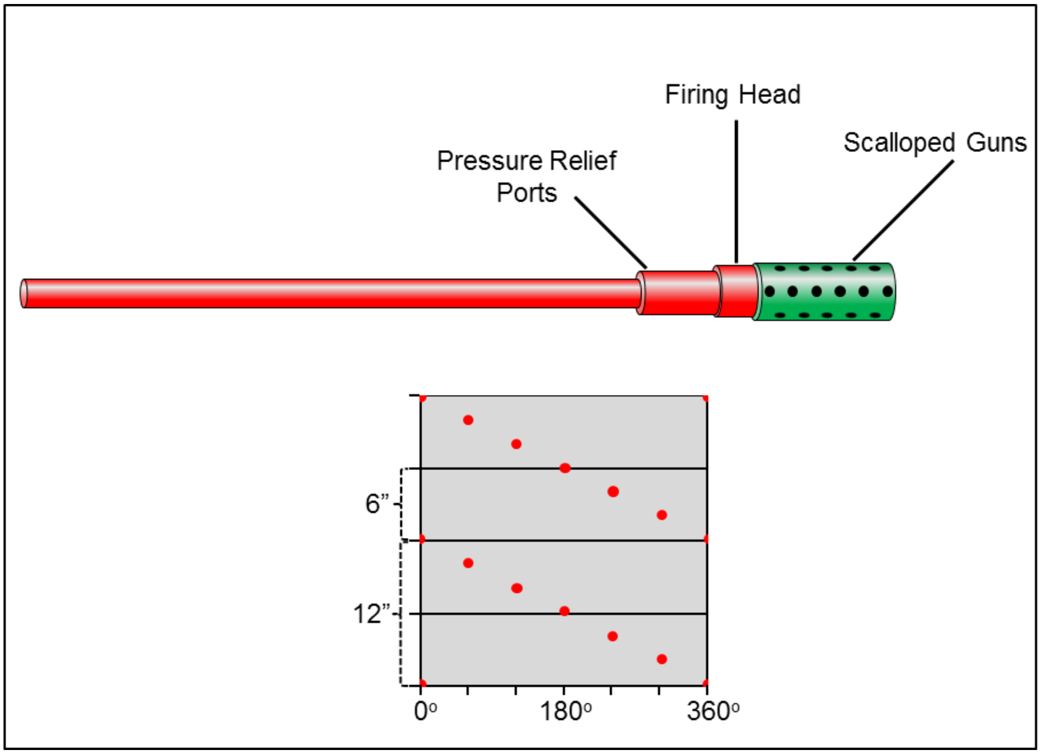


Figure 2.4: Example of a gun system with 60º phasing and 6 shots per foot. Due to the phasing, the shots create a series of shot lines along the diagonal direction in the borehole wall (modified from Halliburton, 2017).

signal of the Equation 2.31), from the calculated P- and S-waves traveltime differences (brackets in right side of minus signal of the equation 2.31). It is shown below, after some algebraic steps starting from equation 2.30, the equation to be minimized for each geophone level is:

$$min\left\{[t_S - t_P] - \left[\left(t_{0_S}\sqrt{\frac{4H^2+x^2}{4H^2+\frac{g_S}{g_S+1}x^2}}\right) - \left(t_{0_P}\sqrt{\frac{4H^2+x^2}{4+\frac{g_P}{g_P+1}x^2}}\right)\right]\right\} \tag{2.31}$$

where $t_S$ is the S-wave two-way time of the perforation shot, $t_P$ is the P-wave two-way time of the perforation shot, $t_{0_S}$ is the S-wave zero-offset two-way traveltime of the perforation shot, $t_{0_P}$ is the P-wave zero-offset two-way traveltime of the perforation shot, $H$ is the depth of the perforation shot, $x$ is the offset and $g_S$ and $g_P$ are the vertical heterogeneity of the S- or P-waves, respectively. Note that all variables of Equation 2.31

are known except the $t_{0_S}$ and the $t_{0_P}$ which are the variables to be found to minimize the difference between the bracketed term to the left of the minus signal (field values) and the bracketed term to the right of the minus signal (calculated values). Once the $t_{0_S}$ and $t_{0_P}$ are found, they can be used in Equation 2.30 and the traveltime between source and receivers can be calculated. Initial values for these variables can be obtained from S- and P-sonic well logs and then calibrated with checkshots data. Although the $t_S$ and $t_P$ variables do not come with the perforation shots, their difference is available from field data based on the difference between the direct arrivals of these modes at each geophone. The number of equations depends on the number of geophones. The total number of equations is equal to $n^2$ where $n$ is the number of geophones. since combinations of direct arrivals of different geophones can be used to constrain $t_{0_S}$ and $t_{0_P}$ minimization. Another constraint is that the zero-time of P- and S-waves have to be the same, regardless the geophone level which recorded the direct arrival; hence, different levels of receivers have to point to the same calculated zero-time value.

Note that the Equation 2.31 used in the minimization process works for layered isotropic cases. This means that effect of the layering, which leads to a nonhyperbolic behavior of the direct arrivals, is corrected by the vertical heterogeneity factor (Al-Chalabi, 1973; Al-Chalabi, 1974), but the effect of the intrinsic anisotropy presents in the layers is not taken into account by this equation. One way to visualize both effects in a layered medium is to analyze Equation 2.24, in Section 2.2, reintroduced below:

$$A_4 = \frac{V_{nmo}^4 t_0 - \sum_{i=1}^{N}\left(V_{nmo}^{(i)}\right)^4 t_0^{(i)}}{4V_{nmo}^8 t_0^3} + \frac{\sum_{i=1}^{N} A_4^{(i)}\left(V_{nmo}^{(i)}\right)^8\left(t_0^{(i)}\right)^3}{V_{nmo}^8 t_0^3}, \tag{2.32}$$

where $\mathrm{t}_0^{(\mathrm{i})}$ is the interval vertical traveltime and $\mathrm{V}_{\mathrm{nmo}}^{(\mathrm{i})}$ and $\mathrm{A}_4^{(\mathrm{i})}$ are the NMO velocity and quartic term for the layer $\mathrm{i}$. The $\mathrm{A}_4$ term rules the nonhyperbolic behavior caused by the anisotropy and by the layering. It is called as the effective quartic term for the layered media, as seen in the Equation 2.18.

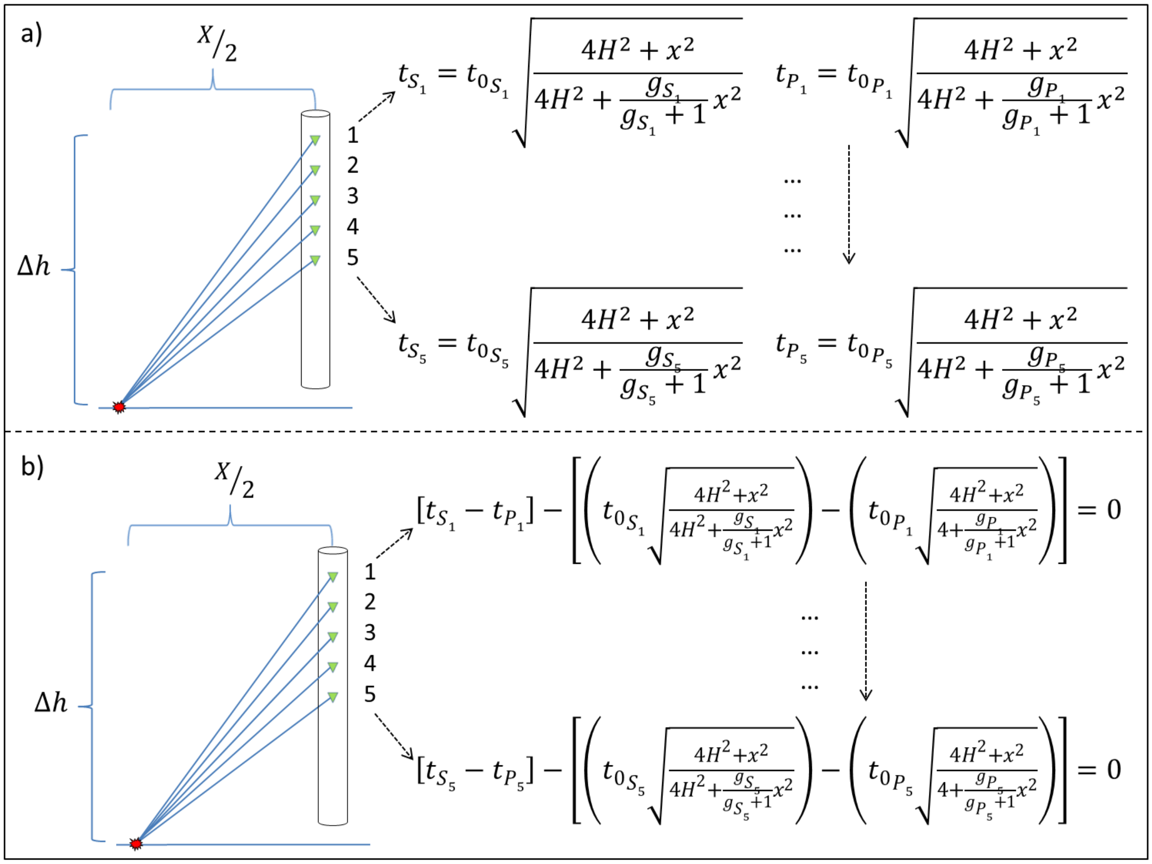


Figure 2.5: Scheme showing the acquisition of one perforation shot by 5 receivers. The equations for each wave mode acquired by each receiver level are shown in (a). In (b) the traveltime difference between P- and S-wave modes allow for a creation of a system of equations which can be used to calculate the zero-time of the perforation shot.

Note that the term at the left side of the plus signal contains only the $\mathrm{V}_{\mathrm{nmo}}^{(\mathrm{i})}$ and $\mathrm{t}_0^{(\mathrm{i})}$ variables meaning that no anisotropic effect is represented by this term, only the layering effect is presented. On the other hand, the term at the right side of the plus signal shows the $A_4^{(i)}$ variable which is the value of the $A_4$ term for each layer in the layered medium. This means that the contribution of the anisotropy is completely defined by this term.

Another point about the anisotropic effect on the hyperbolic behavior of the P- and S-waves direct arrival is linked to angle of the ray propagation (polar angle), or the angle that the seismic ray makes with the vertical axis of symmetry (refer to the Section 2.2 to a more complete explanation about the relation of the polar angle and the P- and S-waves velocity in VTI media).

The changes in the polar angle have a strong relationship with the offset-to-depth ratio. It turns out that, given a constant depth for the target, the smaller the offset, the smaller is the contribution of the anisotropy to the P- and S-waves velocities. That is true because the polar angle is reduced, making the ray propagate near to the vertical direction where the VTI model behaves similarly to the isotropic model.

Therefore, the effect of the anisotropy on the results obtained from the minimization of this system of equations described in the Figure 2.5b has to be measured in order to verify its accuracy and in which scenarios of offset and anisotropy strength this methodology can be used. This test will be explained in the next section.

## 2.5 EFFECTS OF ANISOTROPY AND VERTICAL HETEROGENEITY – SYNTHETIC DATA

To test how accurate would be the minimization of a system of equations based on Equation 2.31 for a layered and anisotropic medium case, I constructed a model based on actual P- and S-sonic well log data. This well log (well 3) is part of the set of wells, perforation shots, microseismic events, and other types of data which were used in my dissertation. I use it as the base of the synthetic models to ensure that specific characteristics of the field data are considered in the modeling which guarantees that the complexity seen in real data can be solved by this approach. In the next chapter, a detailed description of the field data used in the dissertation is presented. For now, I show the 1D model derived from this well.

Figure 2.6 shows the 1D model for P and S vertical velocities derived well 3. It was obtained from an arithmetic averaging process done in Petrel software (Schlumberger) called co-blocking. In this process, the user input all logs aimed to be blocked at once; so, all logs are blocked together which ensures that the output logs have the same boundaries for the resultant blocked layers. The P-sonic, S-sonic, and density logs were input. The user defines two parameters: the minimum thickness of each layer and the blocking factor. The former parameter, as the name says, gives the minimum possible thickness for the blocked layers and the latter defines the maximum number of layers that can be achieved by the output blocked logs. The blocking factor varies from 0 to 1 and it is multiplied by the total number of samples of the reference log which is one of the input logs (all logs have the same number of samples). The result of this multiplication defines the maximum number of layers. The contrast between the average value of each layer compared to average value of the whole log is used to define the most significant layers. Parameters were chosen with the objective of preserving layers with high elastic properties contrast in relation to other neighboring layers, even if their thickness were small. This is an important aspect since the field data used in the dissertation includes a thin-shale layer which shows a large velocity contrast to the carbonate layers above and below to it. In the end, the blocked velocity model was defined with seven layers.

Five synthetic models, one isotropic and four anisotropic, were generated to evaluate different anisotropic strength in the method's accuracy. I used a VTI model for all seven layers of the original isotropic model (Figure 2.6). Four anisotropic models with different combinations of $\epsilon$ and $\delta$ values, constant for all layers, were created: the

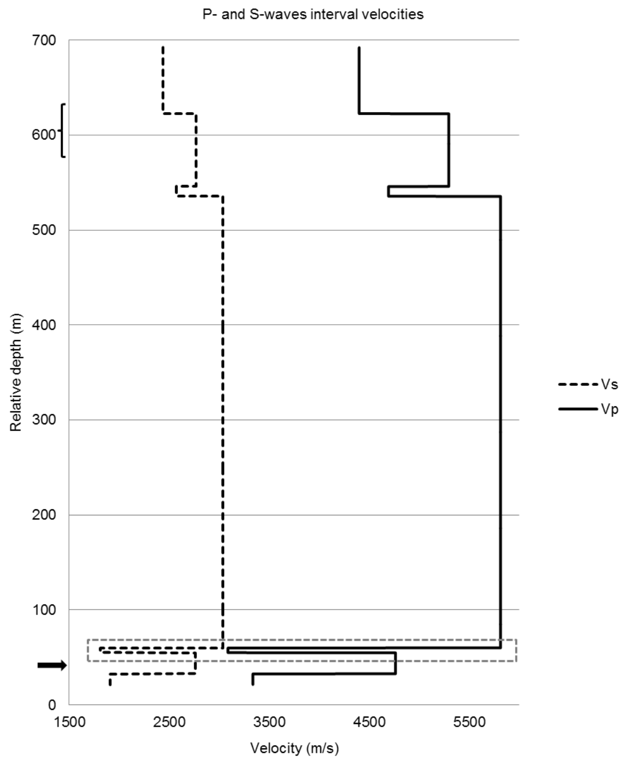


Figure 2.6: 1.5D velocity model derived from the well 3 used to generate the synthetic model. The gray dashed box marks the depth of Upper Bakken black shale. The black arrow and the black bracket mark the depths of the sources and receivers relative to the velocity model used in the isotropic and anisotropic ray tracing.

first model with $\epsilon = 0.1$ and $\delta = 0.05$, the second model with $\epsilon = 0.15$ and $\delta = 0.05$, the third model with $\epsilon = 0.15$ and $\delta = 0.1$, and the fourth model with $\epsilon = 0.05$ and $\delta = -0.05$. These values were defined, roughly, based on values found in the literature for the same area (Havens, 2012; Li et al., 2014; Huang, 2016; Yuan and Li, 2017; Grechka et al., 2017). The analogy between the VTI and orthorhombic models, as explained in Section 2.2 and Appendix A, shows that a hyperbolic relation between $t^2$ and $x^2$ is a reasonable approximation for P-wave, regardless the azimuthal direction, if the offset-to-depth ratio is small and the anisotropy strength is weak. In some degree, the same conclusion can be drawn for SV-waves (SV-wave is more sensitive to anisotropy), if the same conditions aforementioned for P-wave are held (Al-Dajani et al., 1998). The P- and

SV-waves direct arrivals were used as input data in the minimization process. Also, different geometry scenarios were tested within the synthetic models with the objective to recreate the geometry observed in field data. Figure 2.7 shows the distances between sources and receivers locations, with five receivers placed in a vertical well and fourteen sources along a horizontal well. Therefore, fourteen shots located at different offsets from the receivers were recorded. The offsets varied from 25 to 350 meters, with an interval of 25 meters. The five geophones were placed at 634, 619, 604, 589, and 574 meters above the source level. The black arrow and the black bracket mark the depths of the sources and receivers, respectively, in Figure 2.6, relatively to the P- and S-waves velocity models.

With the synthetic models defined, the next step is to calculate the exact traveltime according to the geometry, velocities, and anisotropic parameters. For that purpose, a modified version of an anisotropic ray-tracing code available in the Center of Wave Phenomena Consortium web-page, from Colorado School of Mines, was used to trace the rays from the source to the receiver positions, finding the exact traveltime between them in the anisotropic and isotropic model (Thomsen parameters equal to zero). The original version of this code was developed by Vladimir Grechka and Andres Pech in 2001. A reference to the original code is found in Grechka et al. (2002). The modifications of the ray-tracing code were limited to converting it from a reflection geometry to a point-to-point case, i.e. when source and receiver positions are known, and the direct first arrivals need to be calculated and no reflections are involved. I, also, modified it to run in parallel, i.e. split the process into several CPUs, instead of running the process in a serial fashion (one process per CPU per time unit).

As already mentioned, the number of equations in the system of equations to be minimized is equal to $n^2$ where $n$ is the number of geophones. Therefore, I used 25

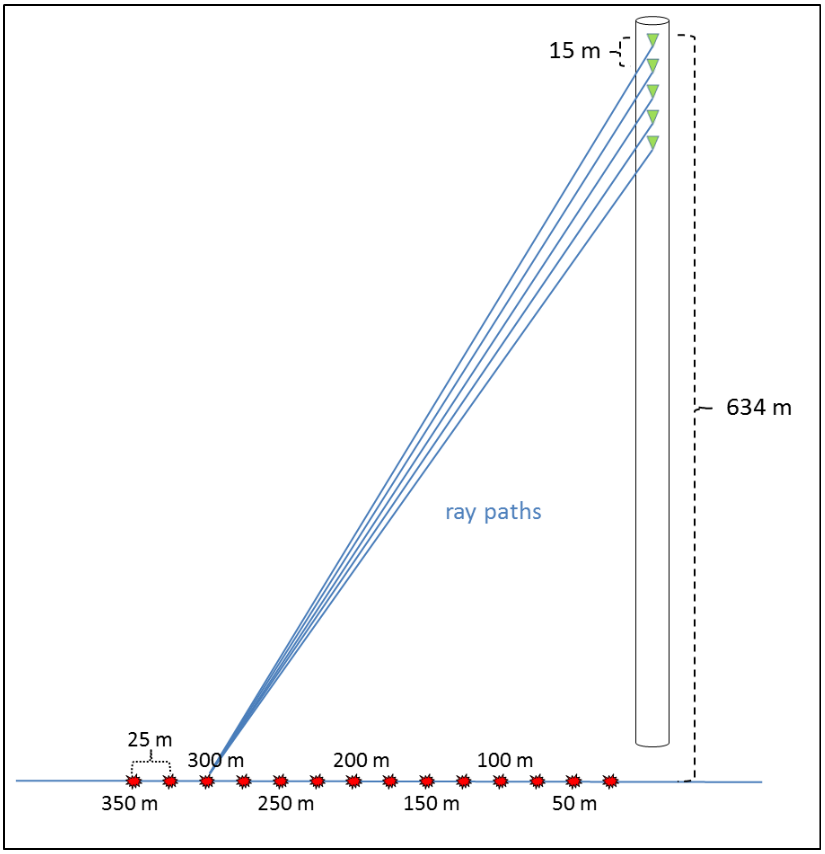


Figure 2.7: Scheme showing the geometry acquisition used to create the synthetic models.

equations since the synthetic models have 5 geophones. Also, a constraint saying that the zero-time for all 5 geophones should be the same was implemented. The initial model for the vertical traveltimes for P- and S-waves, $t_{0_P}$ and $t_{0_S}$, respectively, (equation 2.31) was calculated based on well logs information. In a real case, the initial mode for the vertical traveltimes should be corrected by checkshots data, if available. Nonetheless, to avoid local minimum solutions, upper and lower bounds limited the possible solutions. The limits were 2% for the P-wave and 5% for the S-wave calculated from their initial vertical traveltime and 1000 different vertical traveltime values were tested within this range. The distance between the sources and receivers was used as constraint since the small source-receiver offset and low-velocity variance in the model lead the seismic-ray propagation to be almost straight. I have assumed that the correct values were the ones with the smallest misfit in the minimization process. The values of the heterogeneity factor, $g$, are around 0.009 and 0.006 for P- and S-wave, respectively.

The software used to code the minimization algorithm was from Matlab. The method called *fmincon* was used to find the optimal values of $t_{0_P}$ and $t_{0_S}$ to achieve the least misfit. It minimizes a nonlinear multivariable function submitted to linear and nonlinear constraints. It is a gradient-based method, which may calculate the Jacobian and Hessian matrix if they are not provided by the user. Also, the minimization algorithm was coded in parallel, so that the 1000 trials would have a limited impact on its performance.

The zero-time results for the all synthetic models are evaluated subtracting the ray-tracing algorithm traveltime results from the traveltimes obtained from the minimization process. It is shown, through Figures 2.8 to 2.12, these differences for the geophone located at 604 meters depth (3rd geophone) which is a good average of the differences observed for the all five geophones. The figures which show the misfit are identified by the letter c. The total traveltimes, calculated by the ray-tracing code and by the minimization process, recorded by the geophones at 634, 604, 574 meters depth (1st, 3rd, and 5th geophone) are presented in the figures identified by letters a and b (P- and SV-waves, respectively).

The misfit shown in the isotropic model (Figure 2.8c) is negligible for P- and SV-waves (less than 0.5 ms which is sample rate of our field data). This means that the hyperbolic approach is adequate for the isotropic or near isotropic case.

All anisotropic models tested (Figures from 2.9 to 2.12) show errors for all offsets approximately between ± 1 ms. The errors oscillate around zero alternating positive and negative values. Tsvankin and Thomsen (1994) demonstrated that for small values of offset-to-depth ratio and assuming a medium weakly anisotropic, it is feasible to fit a hyperbola to a seismic dataset, sorted in common depth point domain, even though the correct relationship between the squared traveltime and offset is nonhyperbolic. Although the SV-wave is more sensitive to the anisotropy, the best-fit hyperbola is a good approximation for both P- and SV-waves if the conditions above hold true. In this paper, they show the best-fit hyperbola for P- and SV-waves in a model using the anisotropic parameters derived from the Taylor sandstone (Vp = 3368 m/s, Vs = 1829 m/s, $\epsilon = 0.11$, and $\delta = -0.035$) reproduced here in Figures 2.13a and 2.13b. Note that the residual moveout of the best-fit hyperbola for P- and SV-waves also oscillate between ± 1 ms (Figure 2.13a) and in terms of residual moveout of the P-wave normalized by the vertical arrival time $t_0$ the error is around ± 0.5% (Figure 2.13b). The Taylor sandstone shows anisotropic parameters similar to the $\epsilon$ and $\delta$ values found in my area of study which may indicate that, with that anisotropy strength, a hyperbolic approach could be precise enough. Moreover, these oscillations around zero are also seen in their results.

The higher sensitivity of the SV-wave to the anisotropy compared to the P-wave can be explained analyzing the Equations 2.22 (describe the squared P-wave two-way traveltime as a function of the squared offset) and 2.23 and comparing them with the Equations 2.14 and 2.25 (describe the squared SV-wave two-way traveltime as a function of the squared offset). These equations show that both the P- and SV-waves are a function of $(\epsilon - \delta)$. In P-wave, the $(\epsilon - \delta)$ term is part of the $\eta$ parameter and in SV-wave it is within of the $\sigma$ parameter. In the case of SV-wave, the $(\epsilon - \delta)$ term is multiplied by $\left(\frac{V_{P0}}{V_{S0}}\right)^2$ which magnifies the anisotropy effect. For example, for the synthetic velocity model based on the well 3, in Figure 2.6, P- and S-wave velocity ratio is approximately 1.89, leading to a multiplier equal to 3.57. This makes the influence of anisotropy greater for SV-wave than for P-wave, which could cause a larger deviation from the hyperbolic behavior for SV-wave, assuming the same offset for P- and SV-waves. Apparently, as shown by the synthetic results and also explained by Tsvankin and Thomsen (1994), SV-wave data acquired with the offset-to-depth ratio of 1.5 or less in weak anisotropy medium may be modeled using hyperbolic approach since the deviation derived from the nonhyperbolic behavior is small. Also, it is noteworthy that the actual anisotropy strength depends on the difference of the $\epsilon$ and $\delta$ values and not on their individual values. Therefore, similar values of $\epsilon$ and $\delta$ may lead to P- and SV-waves propagation behavior similar to the isotropic case, regardless of how large their individual values are (Thomsen, 1986).

The main advantage of the hyperbolic equation showed here is to avoid the need of other parameters, as $\epsilon$ and $\delta$ for example, to calculate the traveltime between source and receiver. In addition, it allows the use of the heterogeneity factor and the depth of the perforation shots which are easier to calculate or measured in field.

It is also important to mention that the minimization process searches for the optimal values of $t_{0_P}$ and $t_{0_S}$ which lead to smallest misfit between P- and SV-waves traveltime. This means that, unless the data are acquired in an isotropic medium, their values are not equal to the actual vertical traveltime values but equal to the values that better promote the misfit minimization of the system of equations. Note in Figure 2.13a that even in the zero-offset point the best-fit hyperbola does not show error equal to zero for $t_{0_P}$ or $t_{0_S}$, although, in the VTI media, the P- and S-velocities are equal to the velocities of the isotropic case. This happens because the normal moveout velocity that gives the best-fit hyperbola depends on the offset. Therefore, the $t_{0_P}$ and $t_{0_S}$ will vary accordingly to the offset used in the calculation (Tsvankin and Thomsen, 1994).

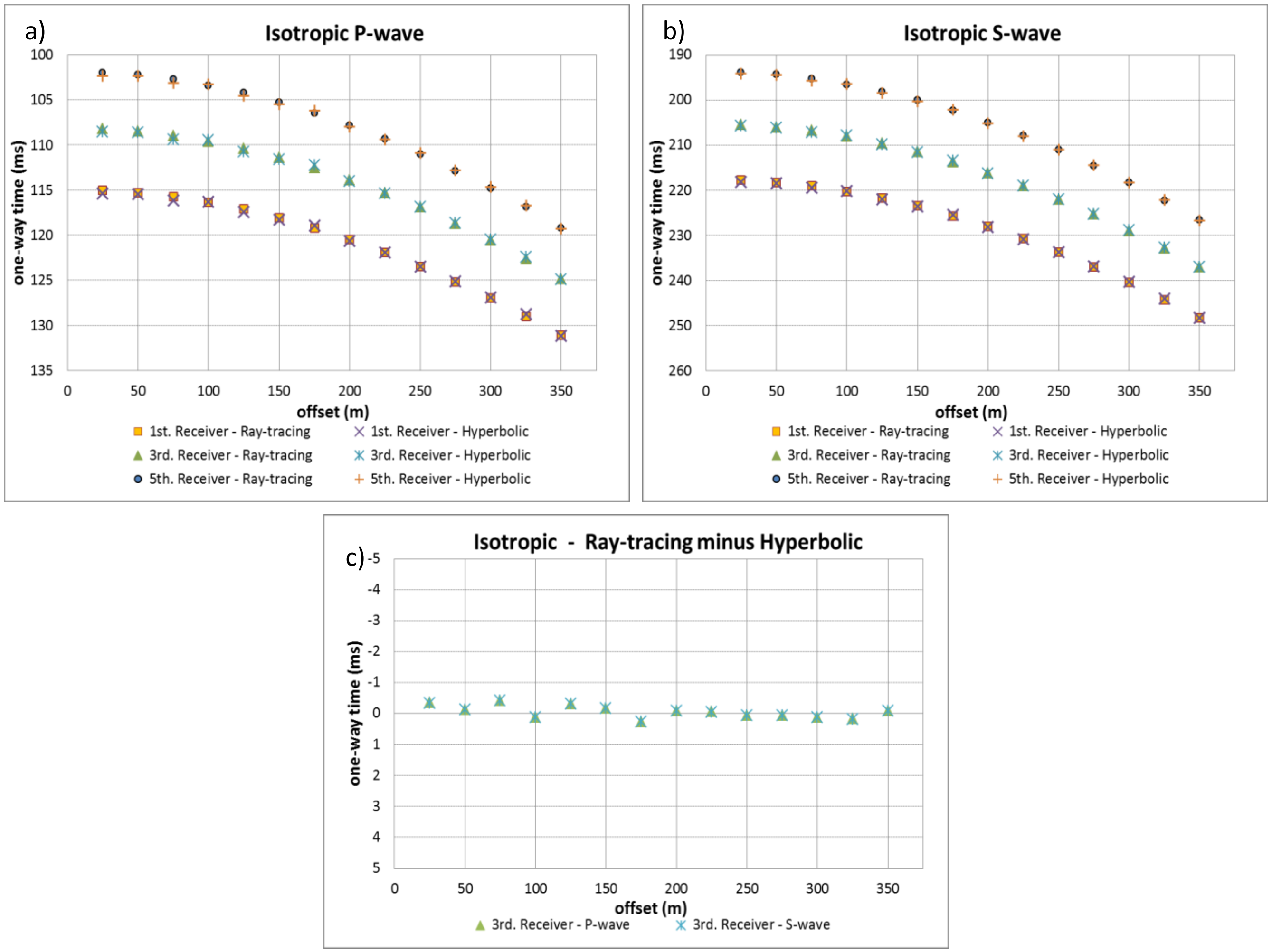


Figure 2.8: The exact (ray-tracing) and calculated (hyperbolic minimization) direct arrival times of three geophones (1st, 3rd, and 5th) for P- (a) and SV-modes (b) with sources at different offset distances using the velocity model showed in Figure 2.6 (isotropic case). (c) shows the one-way time misfits between the exact and calculated direct arrival times for each offset.

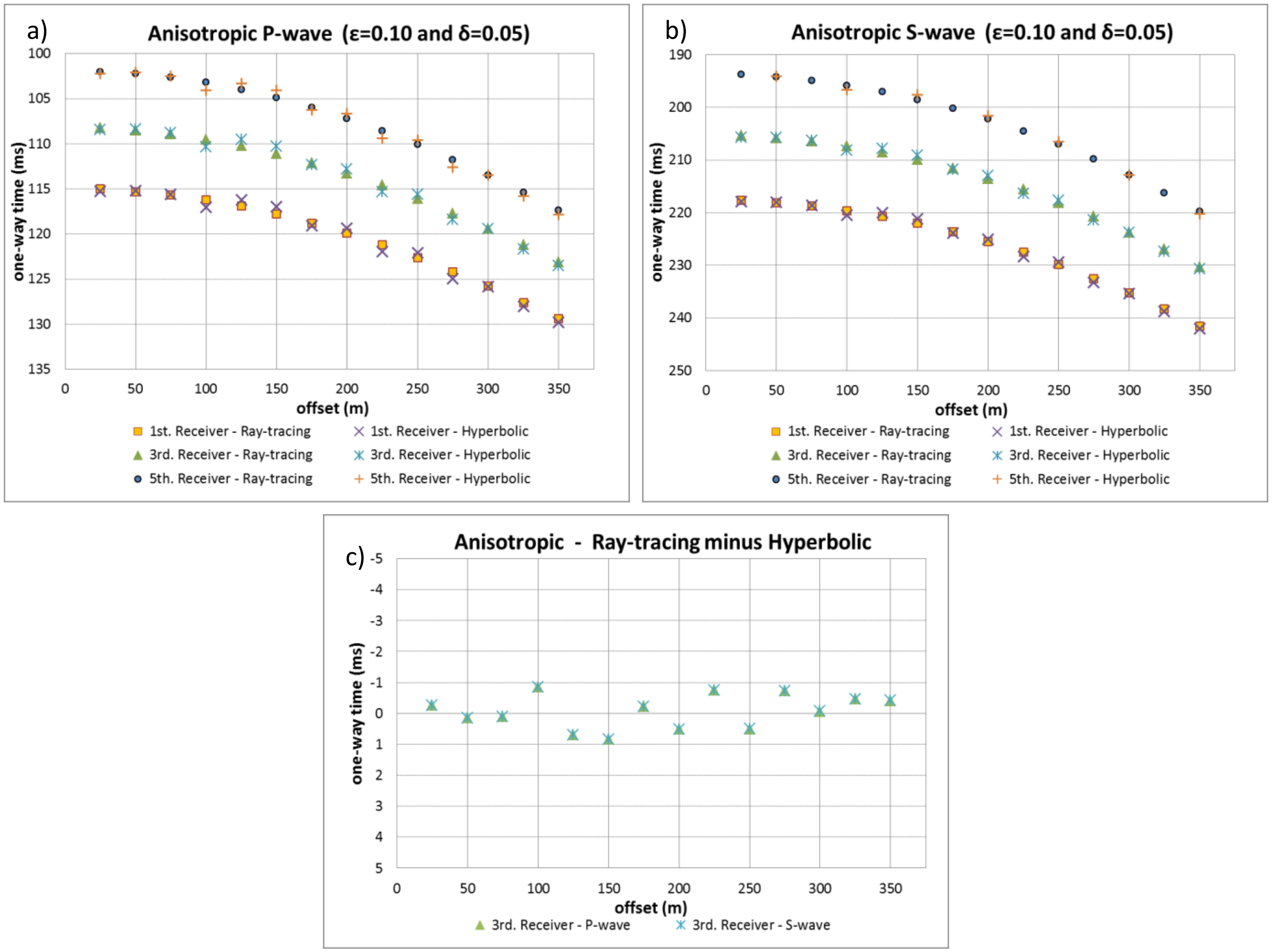


Figure 2.9: The exact (ray-tracing) and calculated (hyperbolic minimization) direct arrival times of three geophones (1st, 3rd, and 5th) for P- (a) and SV-modes (b) with sources at different offset distances using the synthetic anisotropic parameters $\epsilon = 0.10$ and $\delta = 0.05$ and the velocity model showed in Figure 2.6. (c) shows the one-way time misfits between the exact and calculated direct arrival times for each offset.

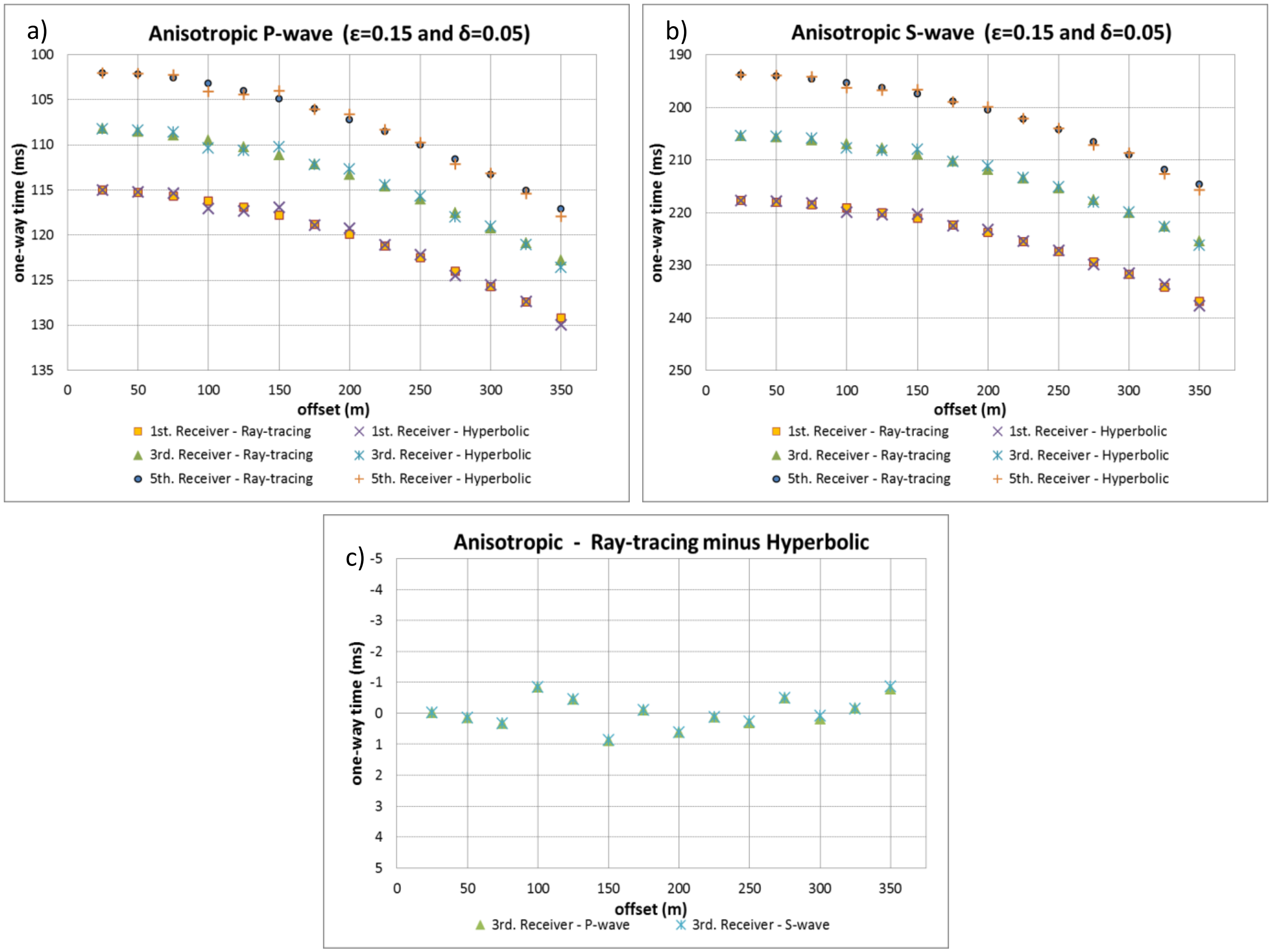


Figure 2.10: The exact (ray-tracing) and calculated (hyperbolic minimization) direct arrival times of three geophones (1st, 3rd, and 5th) for P- (a) and SV-modes (b) with sources at different offset distances using the synthetic anisotropic parameters $\epsilon = 0.15$ and $\delta = 0.05$ and the velocity model showed in Figure 2.6. (c) shows the one-way time misfits between the exact and calculated direct arrival times for each offset.

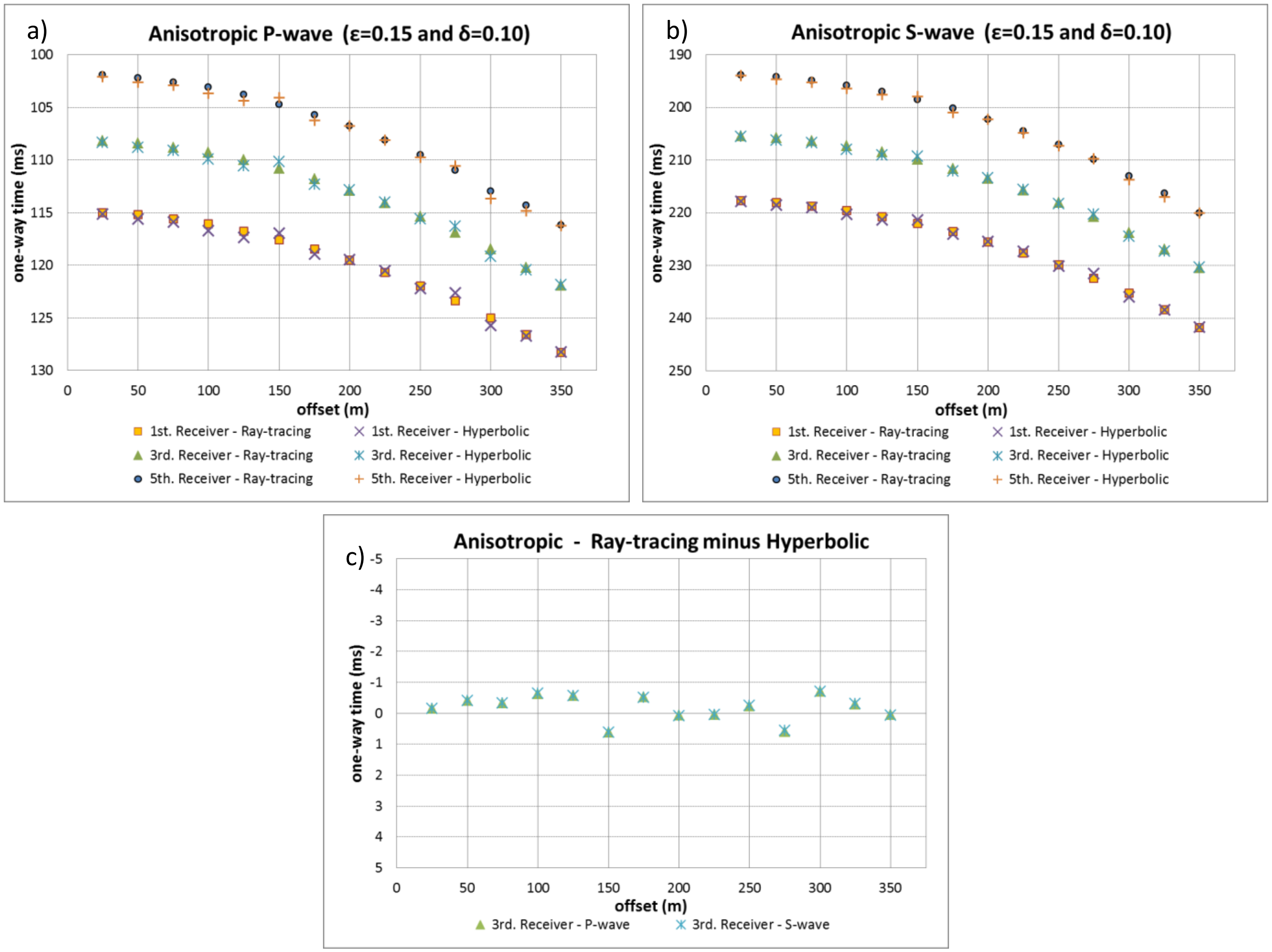


Figure 2.11: The exact (ray-tracing) and calculated (hyperbolic minimization) direct arrival times of three geophones ($1^{st}$, $3^{rd}$, and $5^{th}$) for P- (a) and SV-modes (b) with sources at different offset distances using the synthetic anisotropic parameters $\epsilon = 0.15$ and $\delta = 0.10$ and the velocity model showed in Figure 2.6. (c) shows the one-way time misfits between the exact and calculated direct arrival times for each offset.

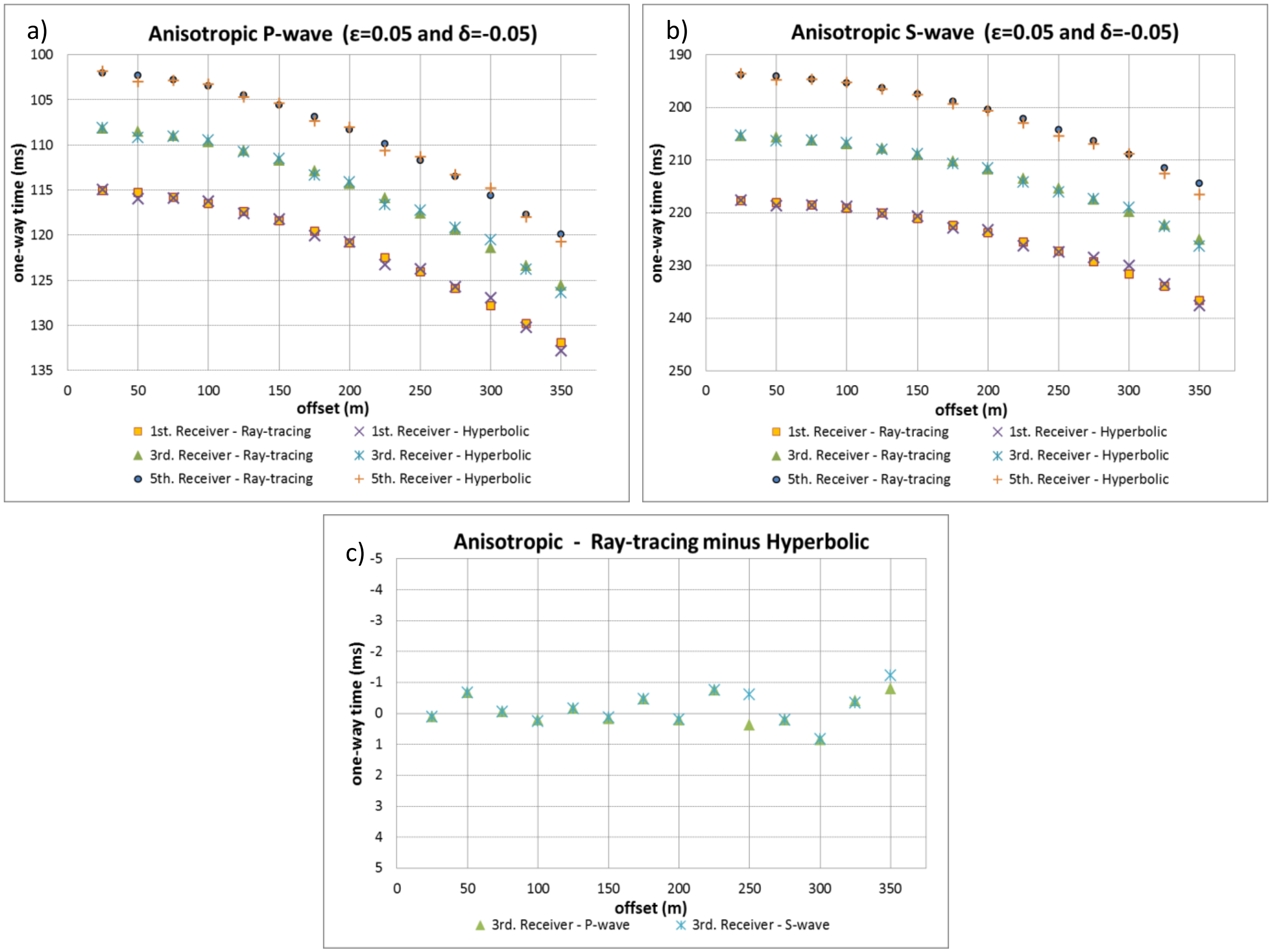


Figure 2.12: The exact (ray-tracing) and calculated (hyperbolic minimization) direct arrival times of three geophones ($1^{st}$, $3^{rd}$, and $5^{th}$) for P- (a) and SV-modes (b) with sources at different offset distances using the synthetic anisotropic parameters $\epsilon = 0.05$ and $\delta = -0.05$ and the velocity model showed in Figure 2.6. (c) shows the one-way time misfits between the exact and calculated direct arrival times for each offset.

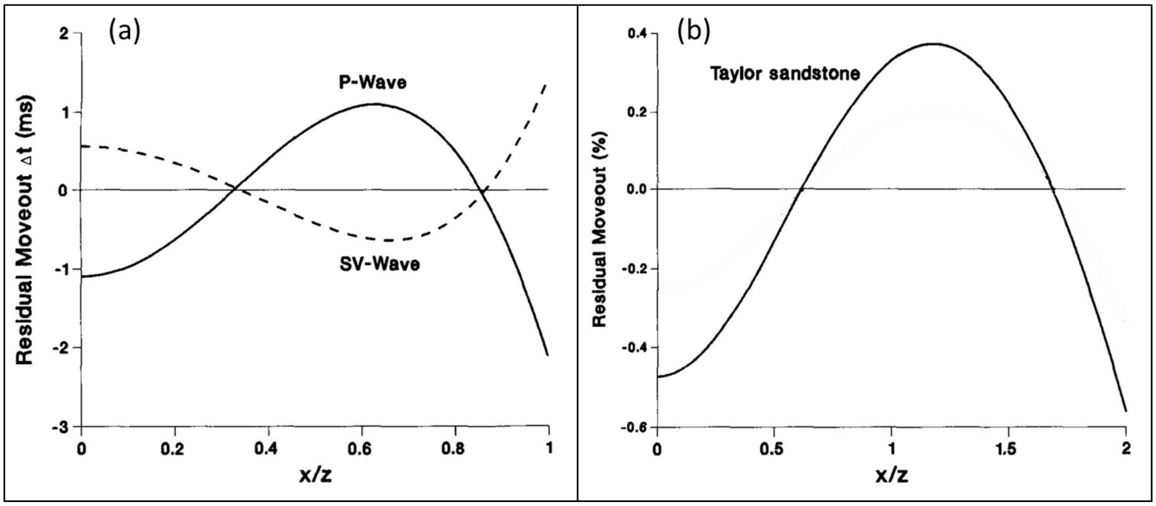


Figure 2.13: The P- and SV-waves residual moveouts in time (a) and the P-wave residual moveout in percentage after the normalization using the vertical traveltime (b) for different offset-to-depth ratio values. The P- and S-velocities and the anisotropic parameters are based on the Taylor sandstone laboratory measurements (modified from Tsvankin and Thomsen, 1994).

A second velocity model (Figure 2.14) was tested which also have seven layers but showing a constantly increasing velocity structure from the top to the bottom of the model. The P- and S-waves velocities increase by 5% from a layer to the next one. All layers have the same thickness in this model and the anisotropic parameters $\epsilon$ and $\delta$ used in the different anisotropic models´ versions are the same used in the model based on the well 3. Therefore, no velocity inversion is observed in this model, differently from the first model. The test with the second model was planned to observe the effect of the steadily increasing of the P- and S-waves velocities on the zero-time calculation. The Vp/Vs ratio for this model is 1.8 for all layers and the value of the heterogeneity factor, $g$, is around 0.006 for P- and S-waves.

The results of the zero-time calculation using the second velocity model are shown through Figures 2.15 to 2.19 for the isotropic and for the 4 anisotropic cases, respectively.

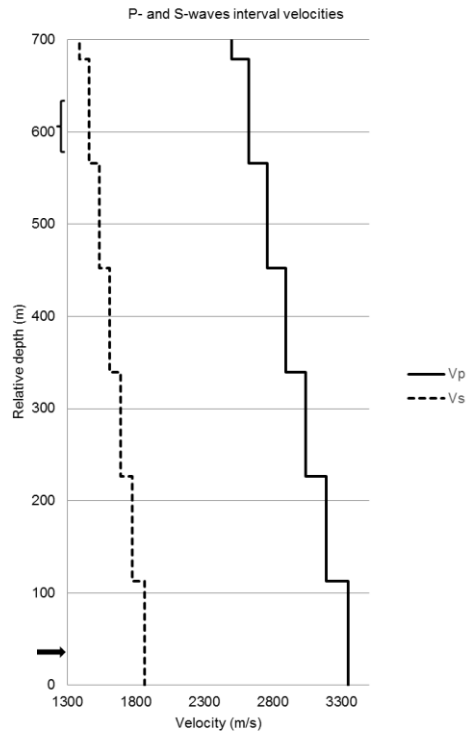


Figure 2.14: 1.5D velocity model with hypothetic steadily increasing P- and S-velocities values with depth. This model was used to generate the second synthetic model. The black arrow and the black bracket mark the depths of the sources and receivers relative to the velocity model used in the isotropic and anisotropic ray tracing.

The results for the zero-time calculation with the second model are similar to what was observed using the first model. The errors for most of the offsets in the isotropic and anisotropic versions of the second model lay between ± 1 ms. The P- and S-waves variances for the second velocity model are smaller than for the first model helping the hyperbolic moveout approximation to fit the synthetic data.

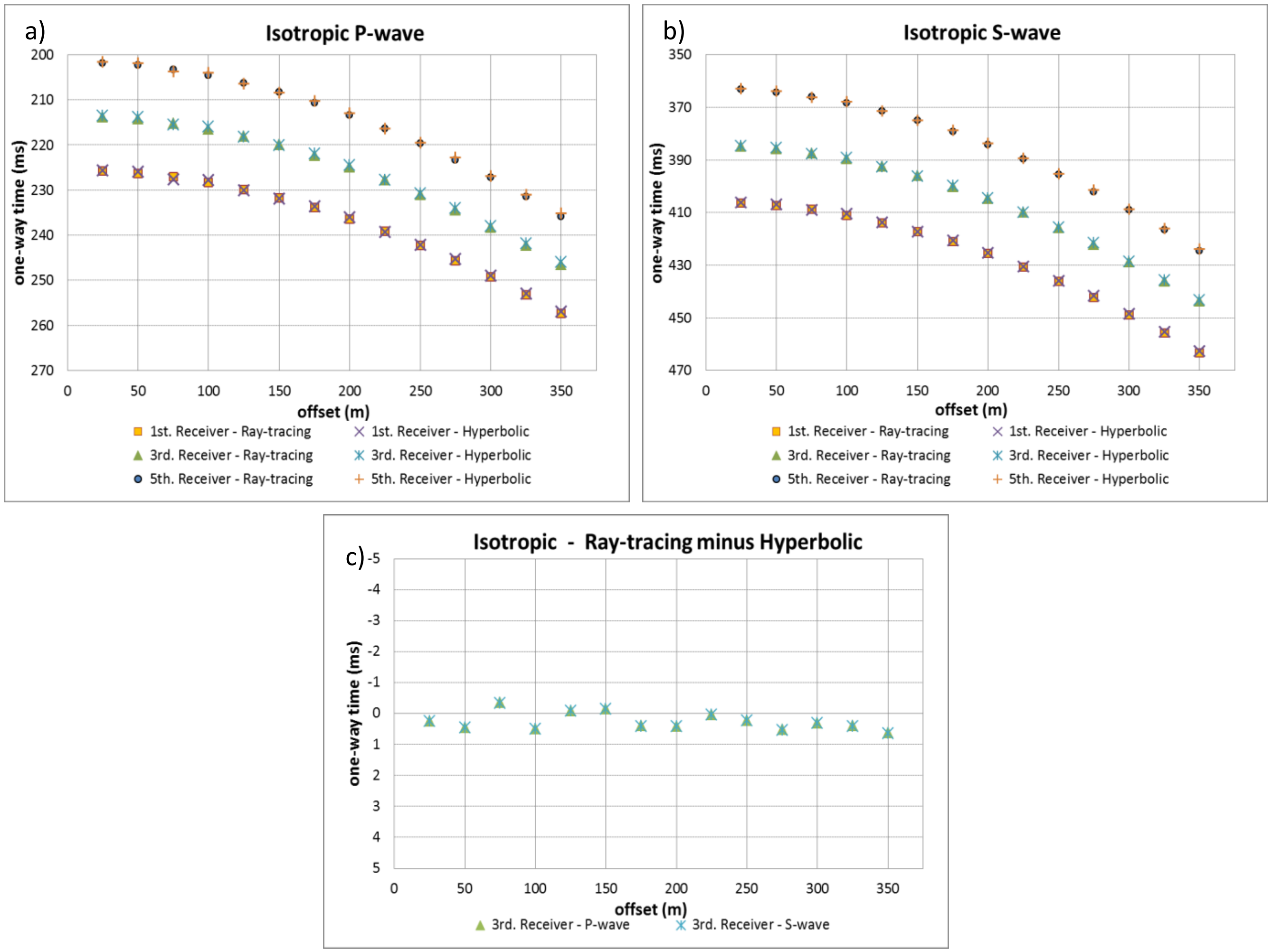


Figure 2.15: The exact (ray-tracing) and calculated (hyperbolic minimization) direct arrival times of three geophones (1$^{st}$, 3$^{rd}$, and 5$^{th}$) for P- (a) and SV-modes (b) with sources at different offset distances using the velocity model showed in Figure 2.14 (isotropic case). (c) shows the one-way time misfits between the exact and calculated direct arrival times for each offset.

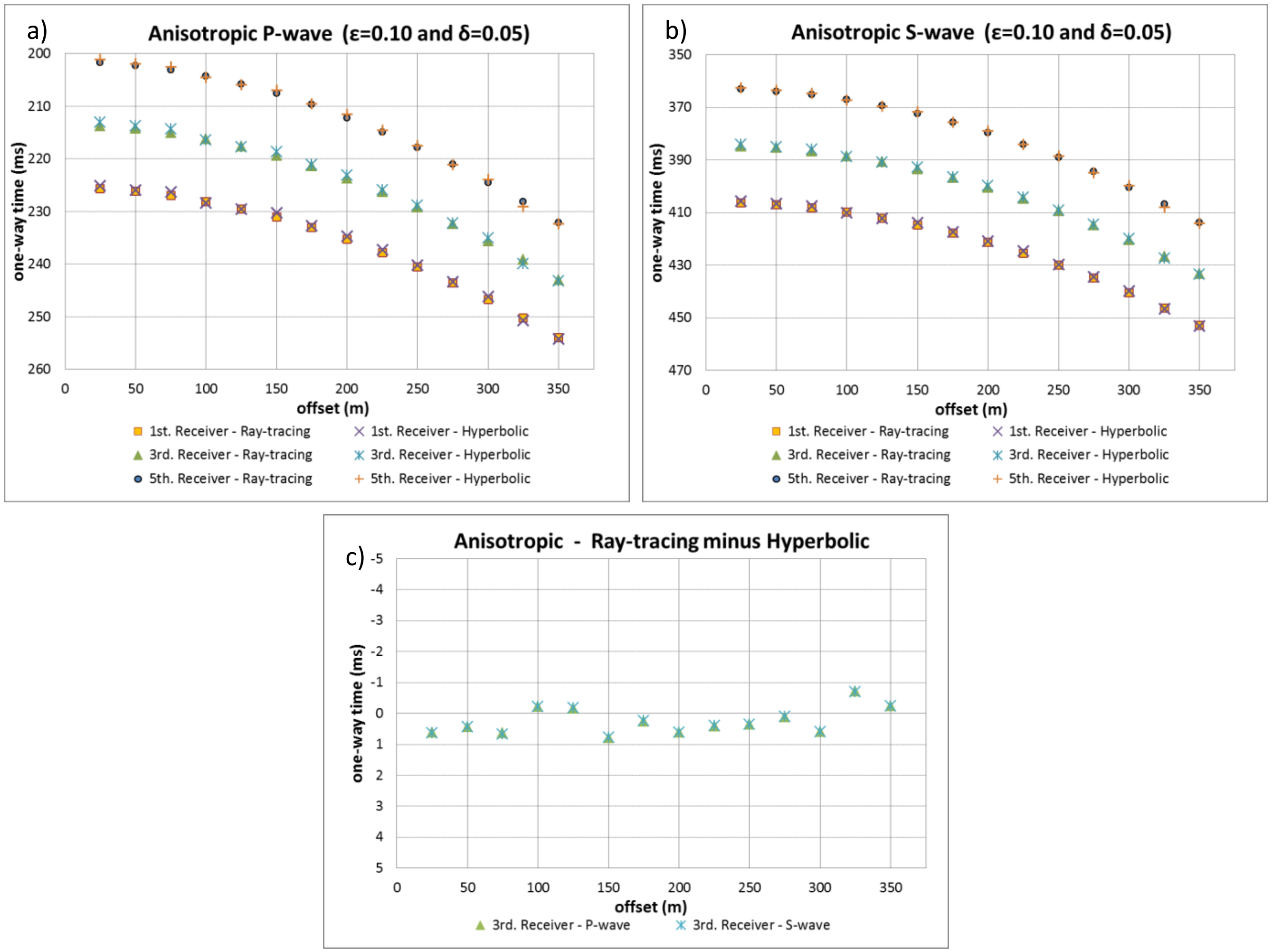


Figure 2.16: The exact (ray-tracing) and calculated (hyperbolic minimization) direct arrival times of three geophones (1st, 3rd, and 5th) for P- (a) and SV-modes (b) with sources at different offset distances using the synthetic anisotropic parameters $\epsilon = 0.10$ and $\delta = 0.05$ and the velocity model showed in Figure 2.14. (c) shows the one-way time misfits between the exact and calculated direct arrival times for each offset.

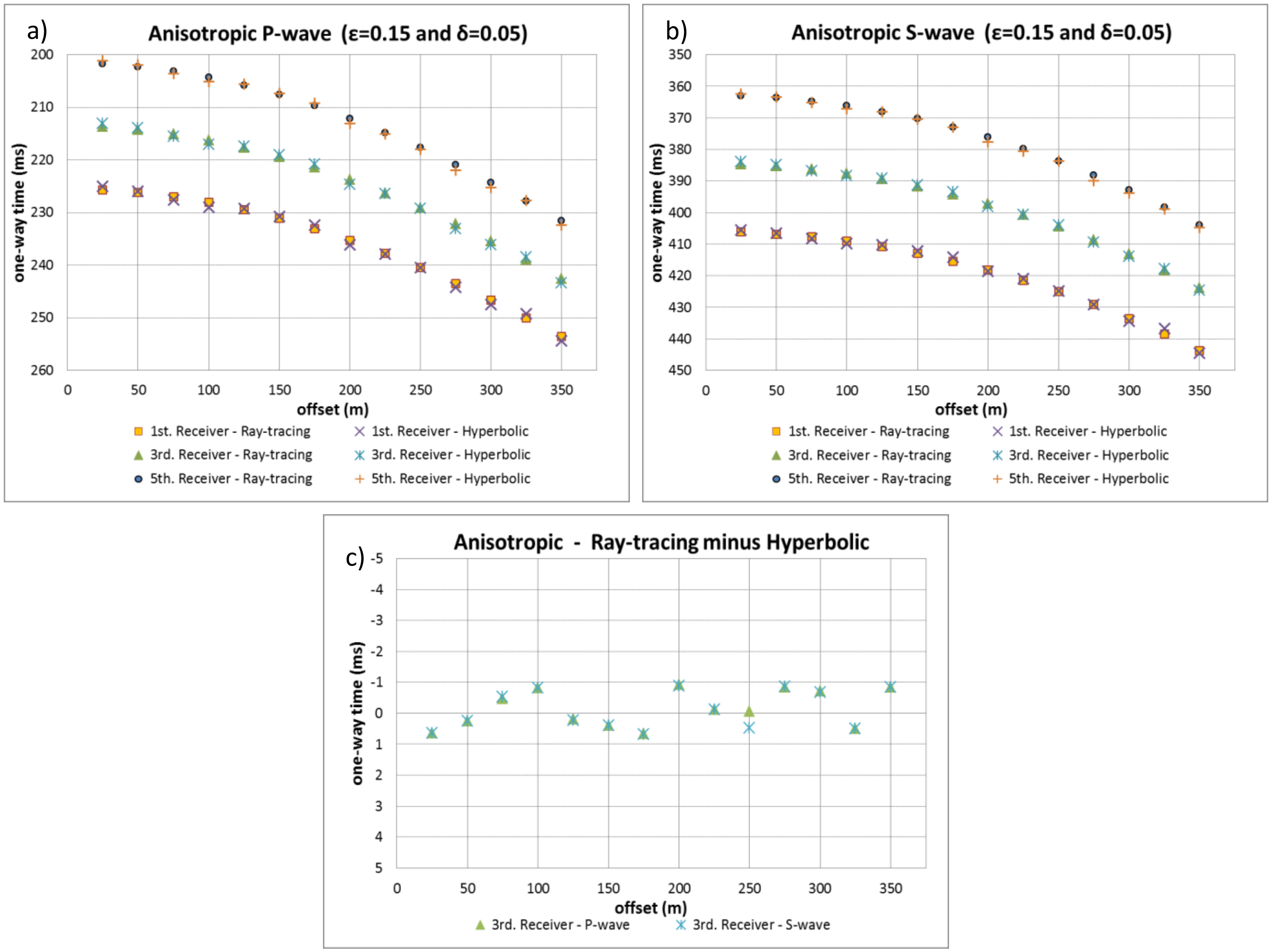


Figure 2.17: The exact (ray-tracing) and calculated (hyperbolic minimization) direct arrival times of three geophones (1st, 3rd, and 5th) for P- (a) and SV-modes (b) with sources at different offset distances using the synthetic anisotropic parameters $\epsilon = 0.15$ and $\delta = 0.05$ and the velocity model showed in Figure 2.14. (c) shows the one-way time misfits between the exact and calculated direct arrival times for each offset.

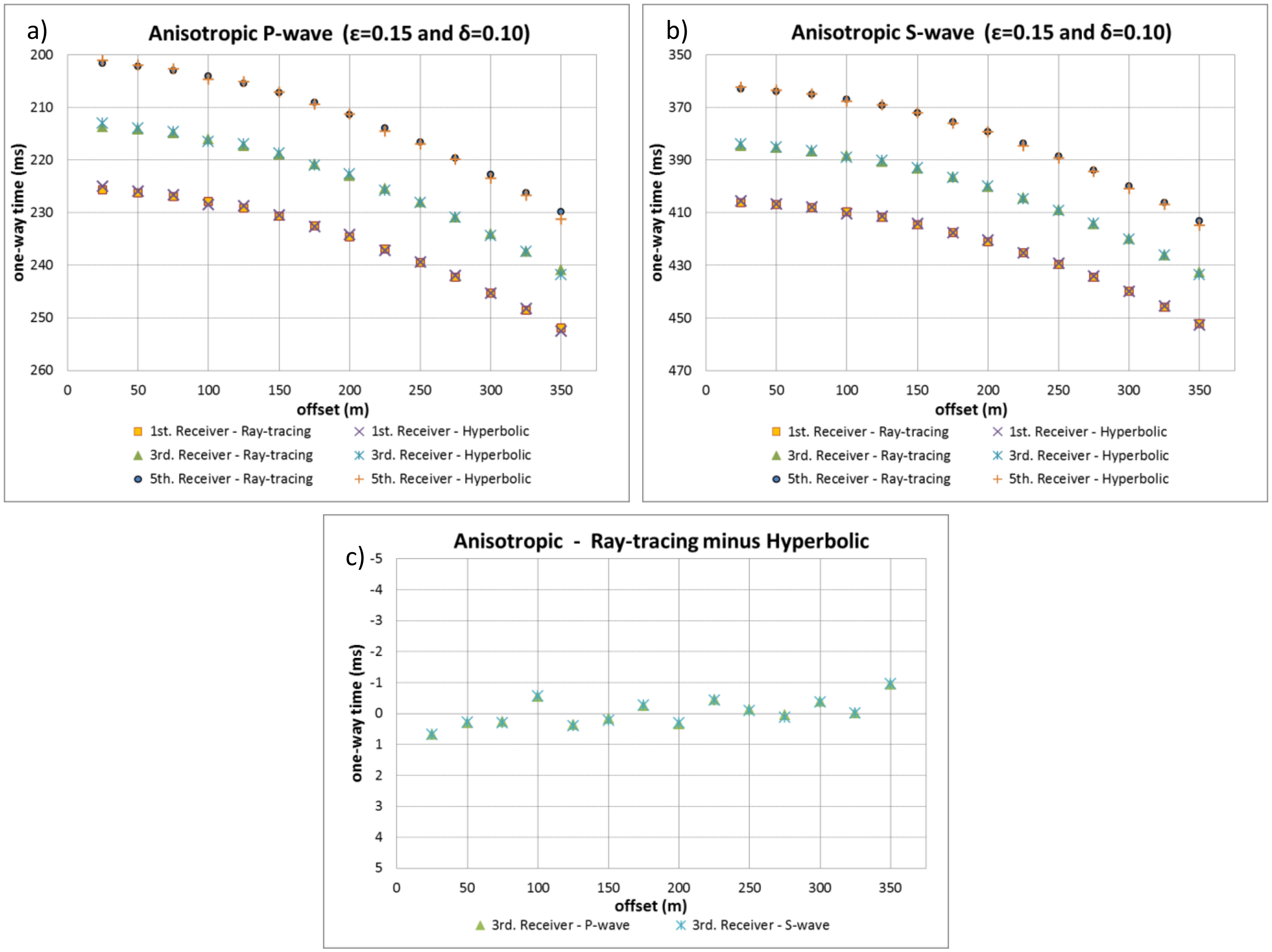


Figure 2.18: The exact (ray-tracing) and calculated (hyperbolic minimization) direct arrival times of three geophones ($1^{st}$, $3^{rd}$, and $5^{th}$) for P- (a) and SV-modes (b) with sources at different offset distances using the synthetic anisotropic parameters $\epsilon = 0.15$ and $\delta = 0.10$ and the velocity model showed in Figure 2.14. (c) shows the one-way time misfits between the exact and calculated direct arrival times for each offset.

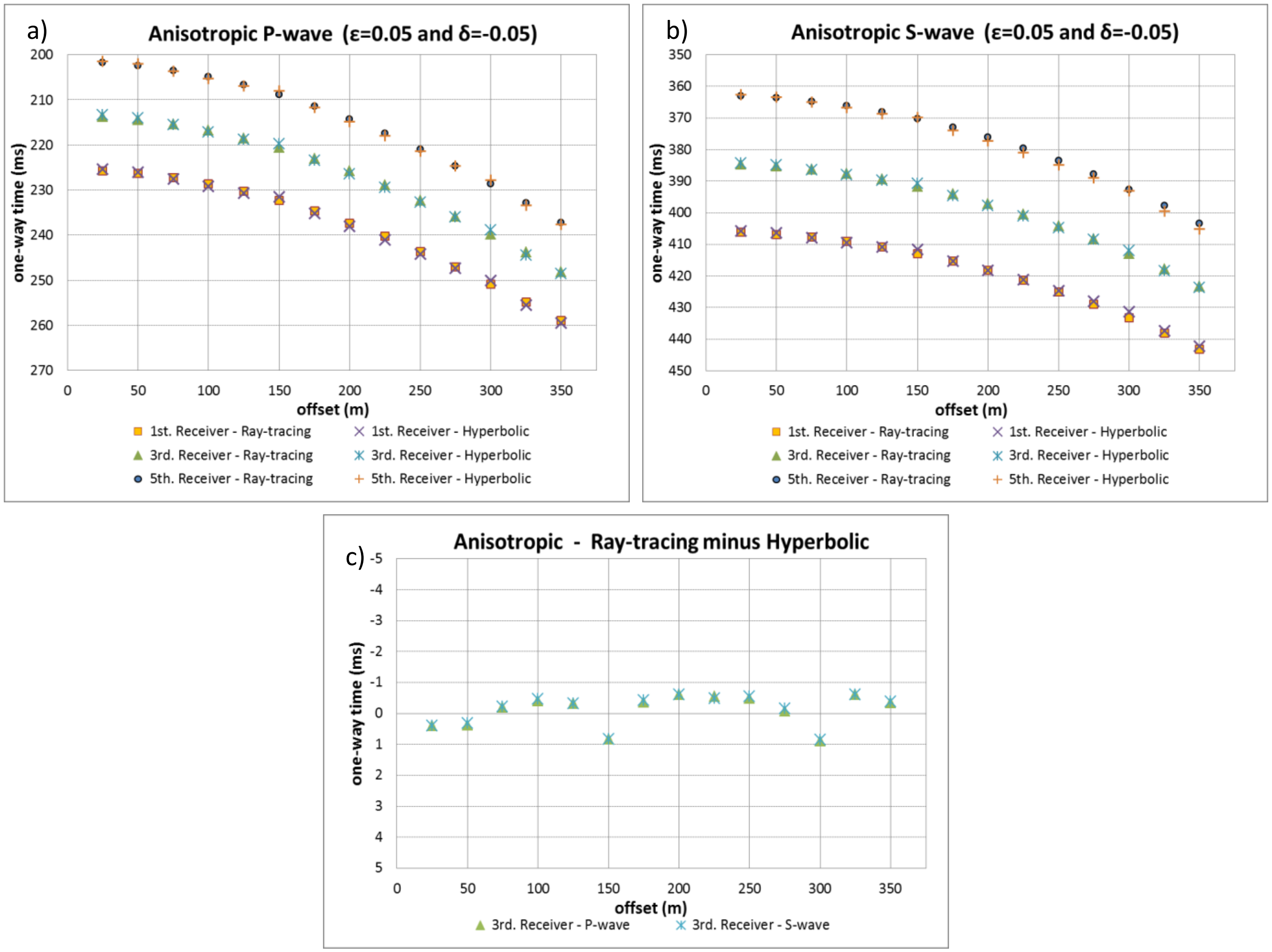


Figure 2.19: The exact (ray-tracing) and calculated (hyperbolic minimization) direct arrival times of three geophones (1st, 3rd, and 5th) for P- (a) and SV-modes (b) with sources at different offset distances using the synthetic anisotropic parameters $\epsilon = 0.05$ and $\delta = -0.05$ and the velocity model showed in Figure 2.14. (c) shows the one-way time misfits between the exact and calculated direct arrival times for each offset.

## 2.6 CONCLUSIONS

The statements below summarize the conclusions of this chapter:

- The zero-time values obtained in the minimization process, following the hyperbolic approach, are precise enough to guarantee the accuracy of the calculated values, assuming that the anisotropy is weak and the offset-to-depth ratio is small (less than 1.5);
- Most of the errors observed in the minimization process remain between ± 1 ms. Even though the SV-wave is more sensitive to the anisotropy effects over the hyperbolic behavior of the $t^2 - x^2$ relationship, the best-fit hyperbola approach is reasonable, assuming the medium as weakly anisotropic and the acquisition geometry with a small the offset-to-depth ratio;
- P- and S-waves velocity model with smaller variance tend to work better with the hyperbolic moveout approach as the propagation of the seismic ray tend to be straighter. This leads to the $t^2 - x^2$ relationship to be closer to the hyperbolic behavior.

# Chapter 3

# P-wave anisotropy changes of the Bakken Formation overburden due to hydraulic fracturing

In this chapter, I show the application of the walkaway and walkaround techniques for the calculation of the near and far overburden anisotropic parameters δ and ε and for the calculation of P-velocity azimuthal anisotropy using data acquired in the Bakken region, in North Dakota[1]. For this purpose, I use the perforation shots direct P-wave arrivals, after the perforation shots zero-time values have been calculated according to the method explained in Chapter 2. At the end of the chapter, I discuss the results and state the conclusions. But, first, I describe the geology of the area and show the geometry of the survey.

[1] Part of the content of this chapter was published as:
Silva, A. A. C., and R. R. Stewart, 2017, Characterizing and imaging hydraulic-fractured overburden layers using perforation shots: 87th Annual International Meeting, SEG, Expanded Abstracts, 2992-2996.

### 3.1 GEOLOGICAL SETTING

The perforation shot data were acquired during hydraulic fracturing of the Middle Bakken member at the Williston Basin Province located in North Dakota (Figure 3.1). The Williston Basin spans from Saskatchewan and Manitoba in Canada over North Dakota, South Dakota, and Montana. It is classified as an intracratonic sag basin developed in the Late Ordovician on the North American Craton. It is alleged that the interaction between two Archean shear systems, the Brockton-Froid-Frombert Fault Zone and the Transcontinental Arch is responsible for the sagging process, leading to structural depression creation where the basin sediments were deposited (Gerhard and

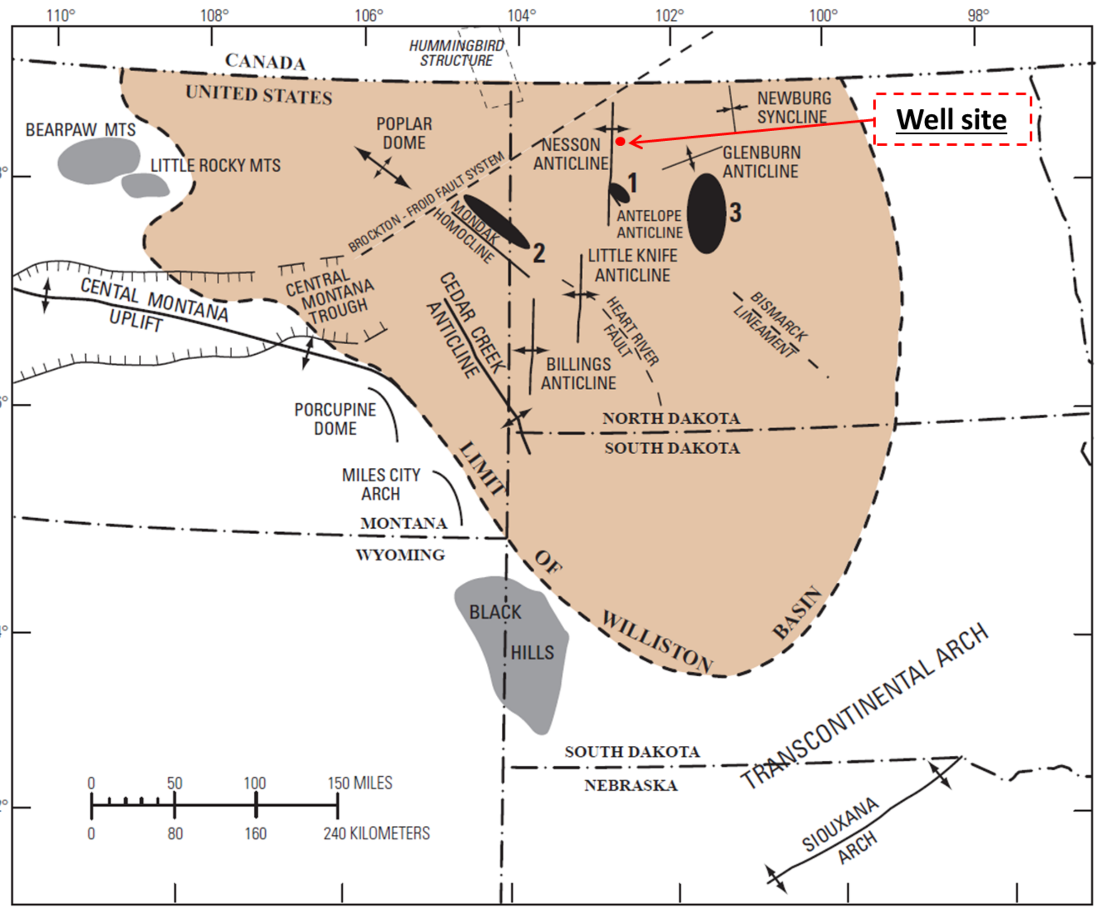


Figure 3.1: Map view of the Williston Basin, USA with major structures identified including the largest oil producing areas in Bakken Formation: Antelope field (1), Elm Coulee field (2), and Parshall and Sanish fields (3). The approximate well sites are identified on the map as well (modified from Pollastro et al., 2013).

Anderson, 1988).

The stratigraphy of the area of interest consists of two main units, namely, the Mississippian Madison Group formed by the Lodgepole, Mission Canyon and Charles formations and the Late Devonian Early Mississippian Bakken Formation. The Bakken Formation is divided in 3 members: Upper, Middle, and Lower Bakken members. The maximum total thickness of Bakken formation is approximately 50 m (160 ft) and it is located at its depocenter just to the west of the Nesson Anticline (LeFever, 2008). The Bakken Formation was deposited in the Late Devonian-Earlier Mississippian and both the Upper and Lower Bakken are classified as black shales. They have high TOC content (10% for the lower member and up to 35% for the upper member) with a maximum thickness of 17 m for the lower member although the upper member, generally, shows 9 m or less (LeFever, 2008). The Middle Bakken is classified as sandstone/siltstone showing a much more variable composition which includes mudstone clasts and detrital limestone and dolomite (Pitman et al., 2001). The three members are easily identified in well logs (Figure 3.2), although due to their limited

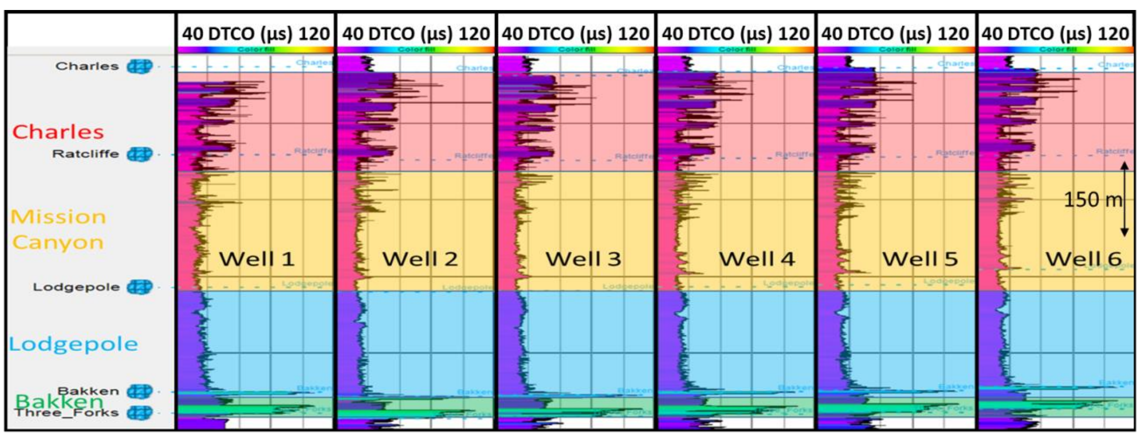


Figure 3.2: P-sonic logs of 6 vertical wells acquired in the study area. The limits of the formations sampled in the wells are identified by the colors of the boxes. Note the high compressional transit time values (low P-velocity) for the Bakken Upper and Lower members (black shales). The true vertical depth of the wells is not annotated due to the confidentiality terms.

thickness cannot be completely resolved in the seismic images. The Lower Bakken member is underlain by the Sanish Sand, which varies, in term of composition, from a coarse siltstone to fine sandstone and dolomite, located at the top of the Three Forks Formation (Upper Devonian). The Sanish Sand importance derives from the discovery well of the Bakken Formation, at the Antelope Field, leading to the beginning of the production in Bakken Formation and Sanish Sand layer (Pollastro et al., 2013).

According to reports yielded by Hess Corporation, geochemical data obtained from the Rock-Eval pyrolysis analysis of core samples in our study area show total organic content (TOC) of the Upper and Lower Bakken members varying from, approximately, 5 wt. % to 20 wt. %, classified as type II-III and within the mature oil window in today´s conditions. The Tmax is approximately 445 ºC and Hydrogen Index (HI) varies from 200 mg HC/g TOC to 350 mg HC/g TOC. The HI values are in agreement with the HI maps of the Upper and the Lower Bakken published by Pollastro et al. (2013). The Upper Bakken member is overlain by the Lower Mississippian

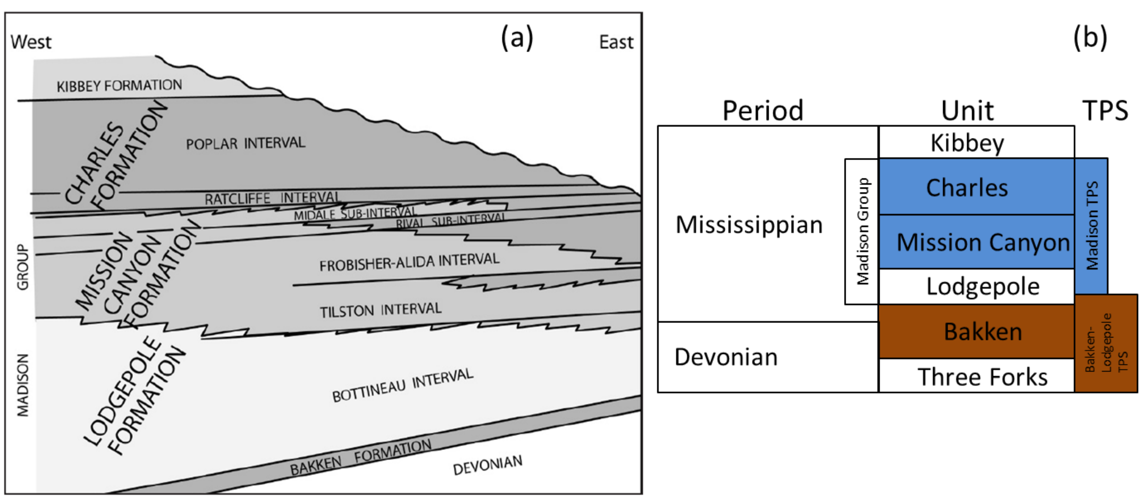


Figure 3.3: Geologic cross-section (a) from west-to-east of the Williston Basin including the units of the Bakken-Lodgepole and Madison Total Petroleum System (b) (modified from Gaswirth et al., 2010).

Lodgepole Formation. The conventional oil accumulation associated with Bakken Formation is classified as part of the Bakken-Lodgepole Total Petroleum System (Figure 3.3).

The Lodgepole Formation is formed by different carbonate units deposited along slope and basin followed by a shelf and slope environments leading to a complex system dominated by a carbonate ramp setting (Kerrs, 1988). Deposits in the shallow part of the ramp are coarser carbonates including calcareous grainstones intercalated with oolitic shoals which become finer basinward (Kent et al., 1988). Conventional reservoirs in the Lodgepole Formation are correlated to the Waulsortian mounds which are associated to paleo-topographic highs at the lower part of the ramp system. The base and the ramp show finer carbonates as thin-argillaceous and cherty wackestones and mudstones sometimes interbedded with thin shales. It has its greatest thickness near the depocenter of the basin reaching, approximately, 250 m of thickness (Gaswirth et al., 2010).

The Mission Canyon Formation overlies the Lodgepole Formation. Laterally, the Lodgepole Formation uppermost sediments grade to the Mission Canyon Formation. Different from of the Lodgepole Formation, which represents the maximum transgression of the sea in the Mississippian age in the Williston Basin (Kerrs, 1988), the Mission Canyon depositional environment is characterized by deposits of carbonates along a gently dipping ramp associated with a shallowing of water due to the regression of the shoreline toward the basin depocenter. Nonetheless, sea-level fluctuations causing cycles of transgression flooding along the ramp followed by shoreline progradation into the basin are recorded (Lindsay, 1988). Stratigraphically, the Mission Canyon Formation shows several discontinuities visible on the log which are used as markers (Petty, 1996).

The different intervals are formed by dolomitized mudstone and wackestone or grainy limestone (Kerrs, 1988).

The Charles Formation is less distributed in the basin showing erosion and absence near to borders of the basin. It has its maximum thickness near the basin center. It is mainly formed by evaporitic rocks showing several interbeds of salt, anhydrite, thin shale and limestone. Charles Formation is divided into two intervals, namely, the lower Ratcliffe and the upper Poplar intervals. The Ratcliffe Interval is divided into seven subintervals characterized by progradational facies in the base overlaid by a sequence of alternating carbonate and evaporite strata. Overall, the subintervals represent a regressive sequence prograding toward the west (Hendricks, 1988). The Poplar Interval is formed by several halite beds alternating with carbonate and anhydrite layers (Gaswirth et al., 2010). The hydrocarbon accumulations associated with Charles and Mission Canyon formations are classified as part of the Madison Total Petroleum System.

## 3.2 DATASET

The data set used in this study includes 80 perforation shots triggered in 2 horizontal producer wells, H2 and H3. The P- and S-sonic (fast and slow), the gamma-ray, and the density logs from 6 vertical wells in the area were also available. In addition, I had the pore pressure profiles of the Bakken Formation collected in the 6 vertical wells and the horizontals H2 and H3. Additionally, the 3D surface P-wave seismic data and the P-wave zero-offset Vertical Seismic Profile (VSP) data acquired at the vertical well V3 were used for velocity calibration and interpretation purposes. Finally, the microseismic events acquired during the hydraulic fracturing of 29 stages in the horizontal well H3 and 38 stages in the horizontal well H2 were used for interpretation as well (Figure 3.4a). An early horizontal producer well, H1, had produced in the area, for 2.5 years, before the other two producers were drilled.

The perforation shots were fired within the Middle Bakken Member. Each stage is 80 m long and 4 perforation shots were triggered in each stage. The distance between each perforation shot within each stage was 12 m. The perforation shots were placed in the center of the stages. All perforation shots were shot by a gun system with the following specifications: 6 shots per foot (spf), 60º phased and 0.42 inches of entrance hole diameter (EHD). The horizontal sections of the H2 and H3 were not cemented. The hydraulic fracturing sequence started in the producer H3 at its toe (north) and moved toward its heel (south). H2 was the second well to be fractured, also with the fracture sequence starting from its north end moving toward in its south end. Figure 2.4 (Chapter 2) shows the geometry of the perforation shots for the for the gun system specifications mentioned above.

The microseismic events and the perforation shots were recorded by the 6 observation vertical wells. Acquisition was done using 3-component geophone arrays with 40 geophone levels. The interval between the geophones was 15 m which makes for 585 m of total array length. Five out of six observation wells (V1 to V5) had their deepest geophones placed approximately 50 m above of the average depth where the horizontal sections of the producers were drilled. For the observation well V6, the deepest geophone was placed 680 m above of the same average depth. Figure 3.4b offers the 2D perspective of the horizontal and vertical with the receivers while the Figure 3.11a offers the 3D perspective.

The relative amplitudes of the perforation shots and microseismic events, i.e. the amplitudes after the attenuation and spherical spreading corrections have been applied, were also provided. They show that the relative amplitudes of the perforation shots are, on average, one order of magnitude higher than those observed in the microseismic events. Also, due to the high frequency shown by the perforation shots, the expected picking error for P-wave is around 0.25 ms. This error value is calculated based on the Equation 3.1 shown below (Aki and Richards, 2002):

$$t_e = \frac{1}{f_m \log_2\left[1+\left(\frac{S}{N}\right)^2\right]} \qquad 3.1$$

where S/N is the signal-to-noise ratio, $f_m$ is the P-wave dominant frequency, and $t_e$ is time error picking.

For P-wave, the signal-to-noise ratio (S/N) and the dominant frequency values are 30 and 400 Hz, respectively. For SV-wave, the S/N was not calculated but it is lower than P-wave S/N. Assuming a conservative value of 10 for the S-wave S/N and of 250 Hz for the dominant frequency (measured), the SV-wave error picking is roughly 0.6 ms. Both P- and SV-wave picking errors are roughly equal to or smaller than the sampling rate used for recording the seismic data, indicating that the picking process should impose a limited error in the zero-time calculation.

Since different data were collected over about 2.5 years, their integration and interpretation require the description of the acquisition’s timeline of these data. The horizontal well H1 was drilled and completed in 2009 and had produced for approximately 2.5 years before the other 2 horizontals and the 6 vertical wells were drilled. The production of H1 lowered the pore pressure of the Bakken Formation. The low pore pressure was identified by the vertical wells V1, V3 and, V4 in 2011. The original pore pressure was 6800 psi and it was measured by the H1 during its production monitoring and by pore pressure gauges installed in the vertical wells V2, V5, and V6, also in 2011 (Dohmen et at., 2014). The 6 vertical wells and the H2 and H3 were drilled approximately from April to July of 2011. The 3D vertical vibroseis surface seismic was

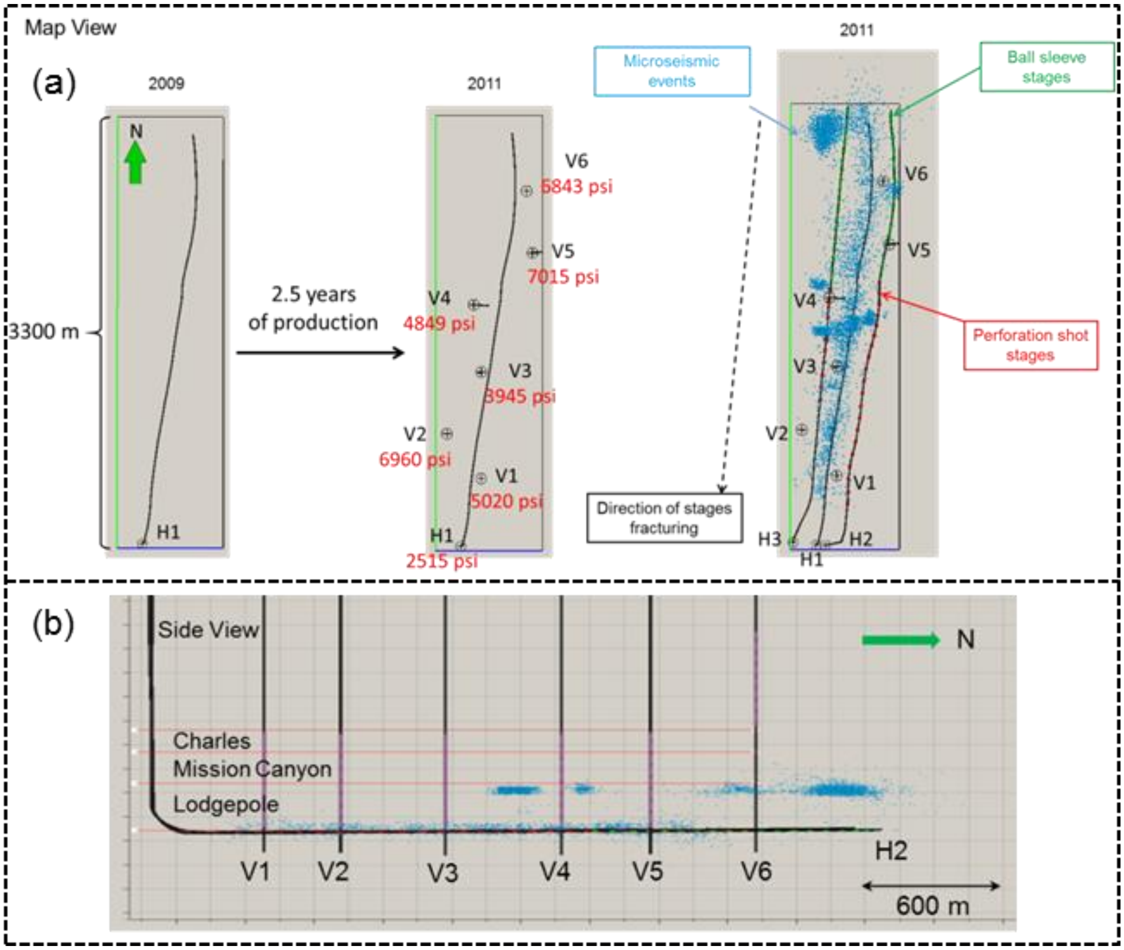


Figure 3.4: a) Map view of the wells drilled in the area separated according to the year they were drilled. H1, drilled in 2009, caused an irregular pore pressure drop within Bakken Formation after 2.5 years of production. The impact of the H1 production in the reservoir pore pressure was measured by pressure gauges placed in the observation wells and H1. Finally, the producers H2 and H3 were drilled and fractured, first H3 and then H2, from north to south. Microseismic events (blue dots) were measured by geophone arrays placed in the observation wells. Northern stages were completed using Ball Sleeve method and southern stages using Perforated and Plug technique. b) Side view showing the location of the microseismic event clusters relative to the observation wells, producers and the formations in the area. The purple dots on the observation wells represent the geophone position of each array. The exact coordinates are not annotated due to the confidentiality terms.

acquired also in early 2008. The vertical vibroseis VSP zero-offset was acquired in August 2011 in well V3. Hydraulic fracturing of the H2 and H3 stages was conducted from September 26th, 2011 to October 16th, 2011. The timeline acquisition is summarized in Figure 3.4a.

## 3.3 ZERO-TIME PROCESSING WORKFLOW AND ELASTIC MODELING

The processing sequence for the calculation of the zero-time started with a bandpass frequency filter (65 – 85 – 480 – 500 Hz) to increase the signal-to-noise ratio of the P-wave direct arrival. After that, horizontal and vertical rotations involving the 3 components of each geophone were performed. This is accomplished by establishing a window around the P-wave direct arrival acquired by each geophone which should be large enough to include one to two wavelet cycles. Next, In the rotation process, the two horizontal channels are rotated yielding the transverse and radial channels. Finally, the radial and the raw vertical channels are rotated yielding the Pmax and Pmin channels. This two-step rotation largely separates the energy of P-wave from other arrivals, especially SV-waves, by focusing their energies on different channels. Figure 3.5 shows the result of the two-step rotation applied to a perforation shot from the stage 19 of the H2 producer recorded by the well V5, located 330 m away from the receivers. After the P and SV-waves have been isolated, the direct arrivals of each phase are picked at the onset of their wavelets. The five uppermost geophones were used in the zero-time calculation as these geophones tend to be less affected by the anisotropy of the overburden layers since, for these geophones, the seismic rays propagate closer to the vertical direction. These time values are the input for the zero-time calculation

Although the picking of the P-wave direct arrival of the perforation shots is straightforward, the picking of the SV-wave can be more difficult since this mode is weaker than P-wave, arrives later, and can be confused with other converted modes. To reduce the SV-wave picking uncertainty, I undertook a seismic elastic modeling with the same anisotropic velocity model shown in Figure 2.8. The density cube was also derived. from the well V3 using the blocking technique described earlier (Chapter 2). Only the plane which contains the source and receivers was modeled (z-x plane). We

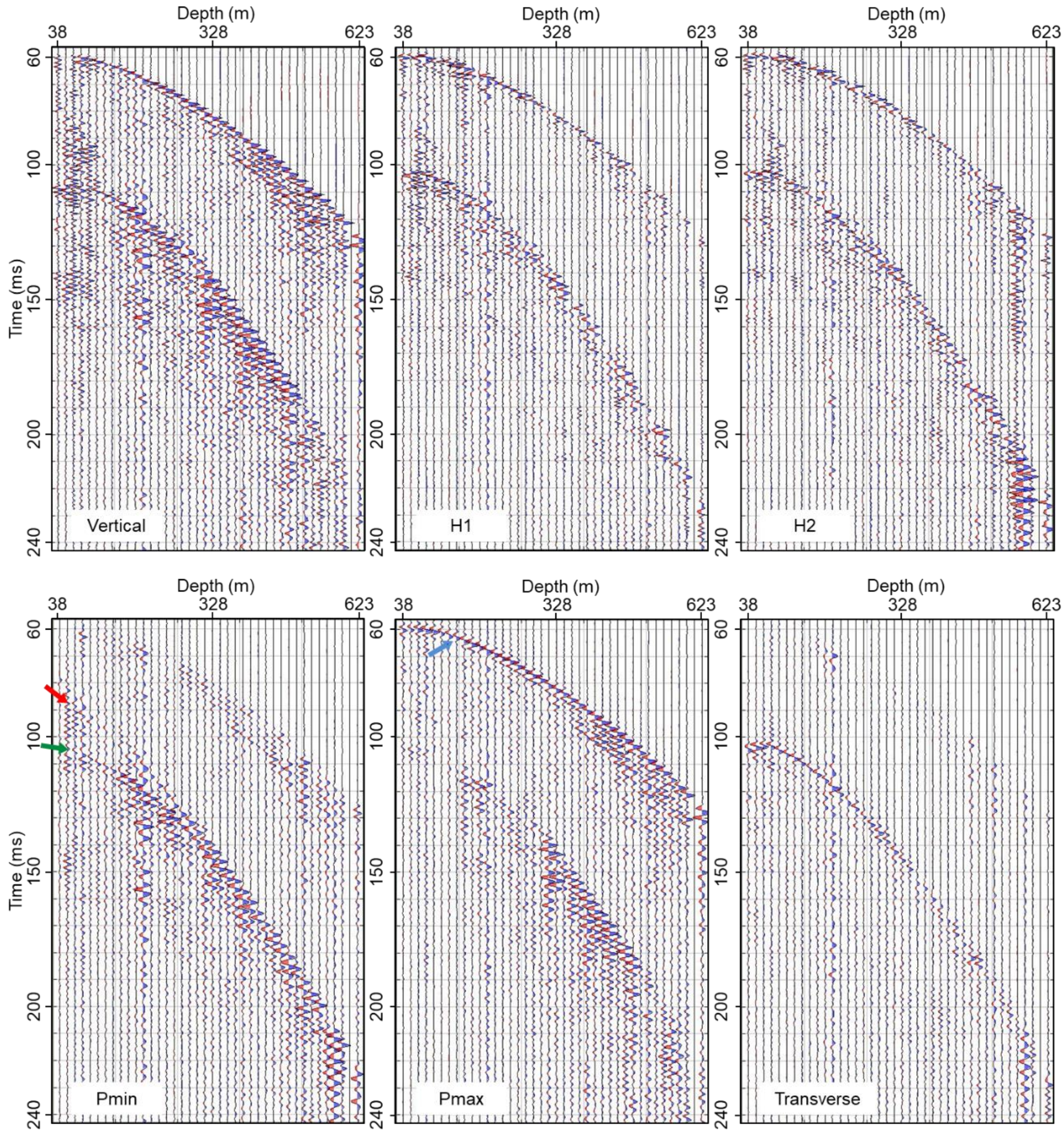


Figure 3.5: Perforation shot from stage 19 of producer H2 acquired by well V5. The upper row shows the raw vertical, H1 and H2 components and the lower row shows the final result after the horizontal rotation, using H1 and H2, and the vertical rotation, using the radial (not shown) and vertical components. The Pmin component highlights the direct SV-wave from the perforation shot (green arrow) and the PSV-wave converted from the P-wave propagation (red arrow). The Pmax component shows the P-wave direct wave (blue arrow).

performed the seismic modeling using Madagascar open-source software package which is an 8th-order spatial and 2nd-order temporal time-domain finite-difference modeling algorithm.

The main objective with this simplified elastic model is to verify whether converted SV-waves from P-wave propagation can interfere with the direct SV-wave generated by the perforation shots, which may be created in the boundary between the Upper Bakken (black shale) and Lodgepole Formation (limestone), where the velocity contrast is relevant. Although the $\varepsilon$ and $\delta$ values of the Upper Bakken Member may be larger than the values used in the modeling (Vernik and Liu, 1997), any converted phase in that boundary will come up since the velocity contrast between these formations is quite large.

Figures 3.6a and 3.6b show six snapshots of the seismic modeling at 1, 15, 40, 100, 150, and 200 ms of time of propagation and its seismogram, respectively, for a perforation shot placed 250 m offset from the vertical geophone array. This geometry simulates a typical perforation shot observed in the field data. For this modeling, we used a Ricker wavelet with a 300 Hz of peak frequency. There is a converted SV-wave when the direct P-wave encounters the Upper Bakken Member – Lodgepole Formation boundary (Figure 3.6a – white arrows). In the seismogram, the direct SV-wave arrives after the converted SV-wave. That is an important result since this modifies where the direct SV-wave arrival times should be picked. Comparing the modeled seismogram (Figure 3.6b) and the real data after the horizontal and vertical rotation (Figure 3.5 - Pmin component), two SV-wave events in the figures can be identified (colored arrows in Figure 3.5 and black arrows in Figure 3.6b). Given the modeling result, the second event was chosen as the direct arrival of the SV-wave (green arrow – Figure 3.5) which was generated by the perforation shot.

It is important to keep in mind that although all perforation shots were recorded by the six observation wells, we used only the first arrival picks from the closest well to each perforation shot to calculate the zero-time. This helped to avoid the anisotropic effects that may be present in the overburden, affecting especially the farthest horizontal offsets. Figure 3.7 shows the offset-depth ratio values using the 3rd. geophone and the second perforation shot of each stage, which is the most central perforation shot within per stage. The offset distance was doubled so that the ratio values shown in Figure 3.7 could be compared to the ratio values more commonly seen in the two-way time propagation case. The lines in Figure 3.7 are linking the stages to the specific observation wells used in the calculation of their zero-time values.

As explained in Chapter 2, the calculated zero-time should be the same for all geophones regardless whether it is calculated with P- and/or S-waves. It turns out that the final result of each geophone used in the minimization did not show the exact same value for the calculated perforation shot zero-time, probably due to the noise introduced during the picking processing. Some small deviations from an average zero-time value were found. Table 3.1 shows the arithmetical average of the deviations in relation to the final zero-time value. The deviations are the differences between the five zero-time values, one per geophone, and their average, i.e. the difference for their final zero-time value. The average is done per perforation shot and the standard deviations of the arithmetical averages are also shown. The arithmetical averages and their standard deviations were calculated for P- and S-waves. Note that both arithmetical averages and their standard deviations are close to zero which indicates the robustness of the results. Also, the differences between the zero-times calculated using the P- and S-waves data are shown. Note that the P- and S-waves absolute differences are small, demonstrating

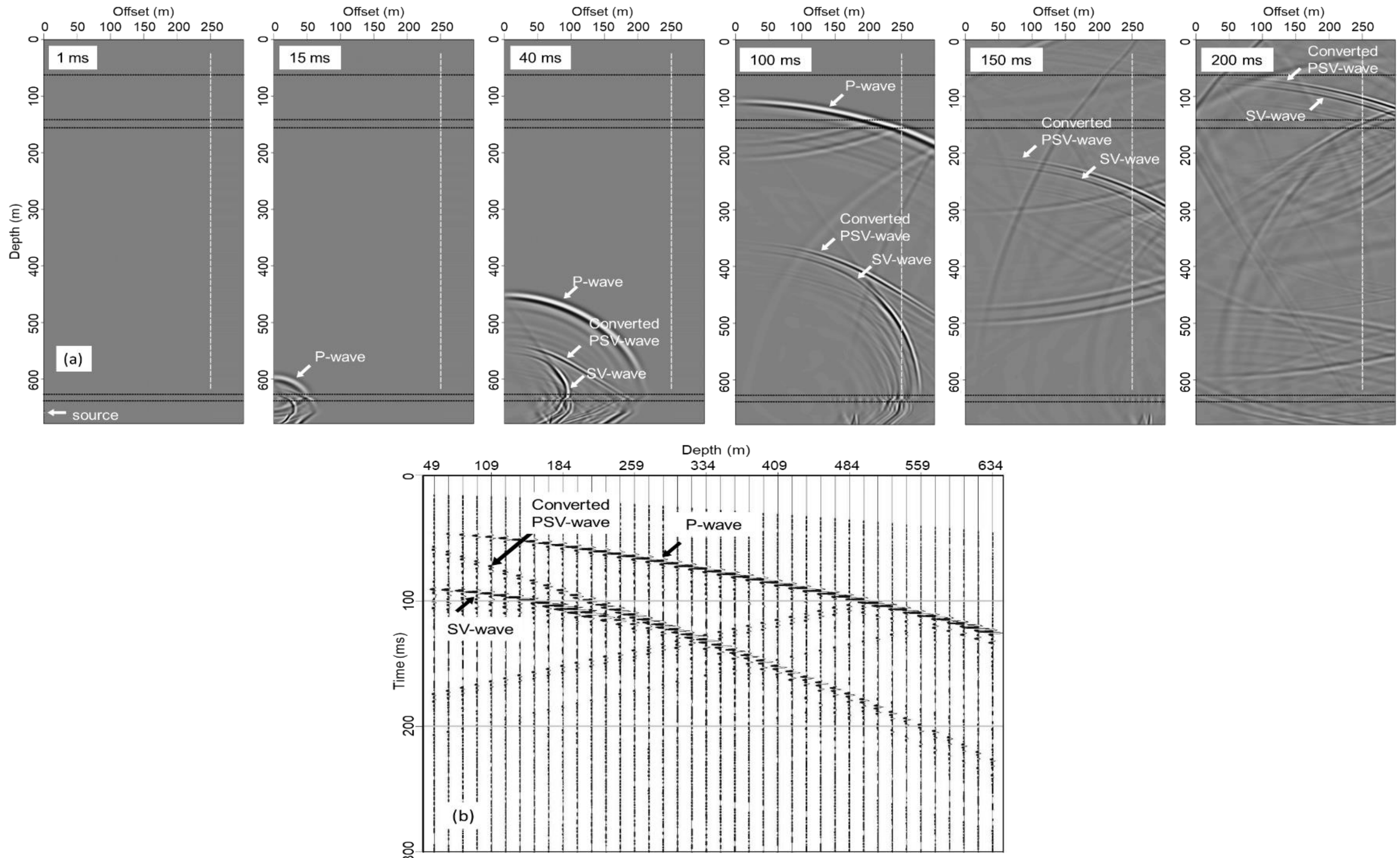


Figure 3.6: a) Six snapshots of the seismic modeling, using the velocity model of Figure 2.8, of a perforation shot offset 250 m from receiver array (vertical white dashed line). A Ricker wavelet with 300 Hz frequency was used. The P- and SV-wave direct modes are observed in the modeling. A converted PSV-wave occurred close to SV-wave requiring attention to pick the correct mode. b) Seismogram of the seismic modeling of the wavefield recorded by 40 receivers, with 15 m of spacing, placed in the white dashed line indicated in the snapshots. P-, SV-, and PSV-modes are pointed out by black arrows.

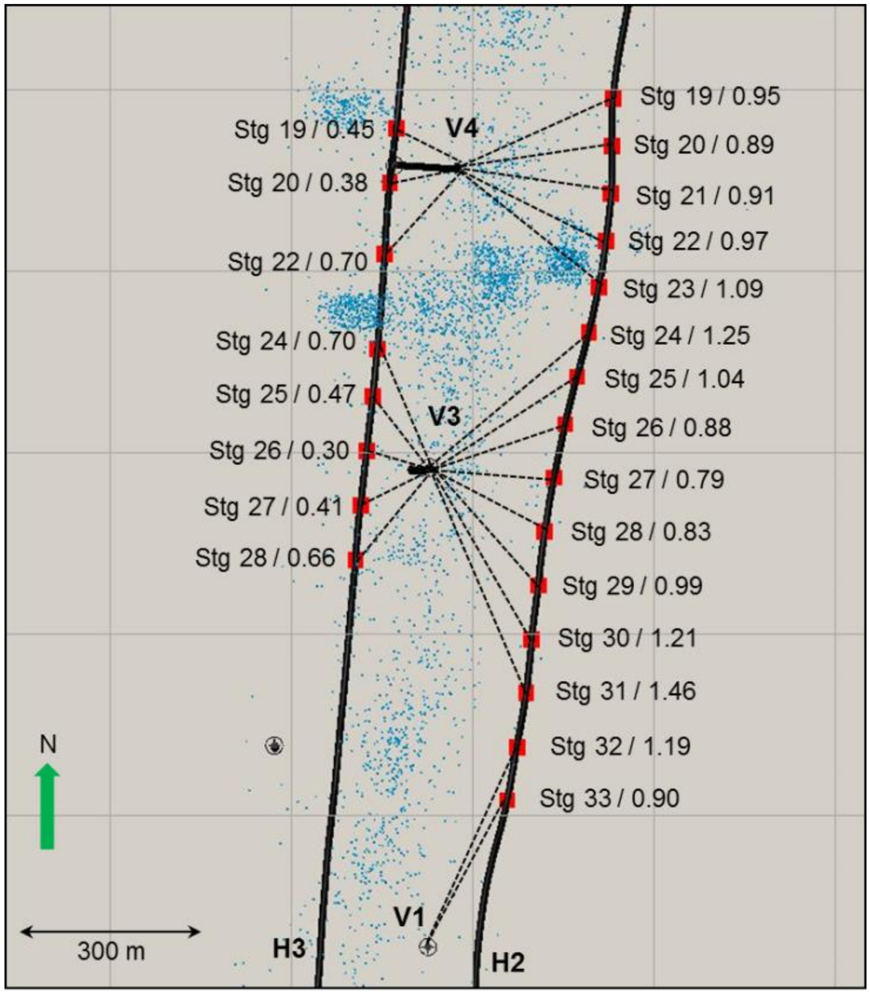

Figure 3.7: Map view showing which observation well was used to calculate the zero-time value. The horizontally closest vertical well to each perforation shot was used to avoid some anisotropy effects. Only the five uppermost receivers of the arrays were used for the zero-time calculation. All stages have four perforation shots although there are stages which not all shots were retrieved. In the map, the average offset-depth ratio of the stage (3rd. geophone for the perforation shot in the midst of the stage) is given. The offset was doubled to simulate the two-way traveltime. The offset-depth values confirm that for most of the perforation shots this ratio is below one which helps to avoid the anisotropy effect allowing for the use of the hyperbolic equation to calculate zero-time values.

the consistency of the method.

Since the shots' depth is not constant due to the mild inclination of the producers H2 and H3, a correction similar to a topography correction was performed using the depth differences between the shots' depth and a fixed datum. The P-velocity for correction was calculated from the zero-offset VSP survey carried out in the well V3.

### 3.4 WALKAROUND STUDY USING PERFORATION SHOTS

After the zero-time calculation of each perforation shot, a VSP walkaround analysis was performed using the direct arrival of P-wave of selected perforation shots. For that purpose, 4 groups of perforation shots, each with 3 shots, approximately with the same horizontal offset from the well V3, were used (Figure 3.8). Each group represents a different offset range from the V3, giving us the chance to analyze whether the traveltime variation of P-wave with the azimuth could indicate the fastest P-wave direction, which might be correlated to the preferential fractures azimuth, and if the fastest P-wave direction might change as the offsets increase. The limitation in the number of perforation shots (3) for each different offset is due to the unusual geometry of the perforation shots which are located along the horizontal section of the H2 and H3 wells. Nonetheless, with 3 perforation shots per offset group, we were able to fit an ellipse, according to the P-wave direct arrival traveltime, using the V3 observation well position as the center of this ellipse. Such minimization searches for smallest misfit between the perforation shots P-wave traveltimes and the ellipse's parameters, namely, the eccentricity (longer and shorter semi-axes ratio) and orientation. This best-fitted ellipse renders the shorter and longer semi-axes which preferentially align with the anisotropy direction that may be caused by the alignment of the fractures' strikes within the area. In this case, the shortest axis is preferentially aligned with the fastest P-wave direction which should be parallel to the fracture strike of the dominant fracture set.

Figure 3.8 shows the map of the 4 groups of perforation shots and the respective

Table 3.1: Arithmetical averages of the deviations in relation to the final zero-time values and their standard deviations. The dashes in some shots mean that only 2 geophones were used in the calculation making the standard deviations equal to zero.

| | *P-wave* | | *S-wave* | | *Difference P- and S-wave zero-times (ms)* |
|---|---|---|---|---|---|
| | *Average (ms)* | *Standard Deviation (ms)* | *Average (ms)* | *Standard Deviation (ms)* | |
| *19H2-perf1* | 0.05 | 0.03 | 0.22 | 0.12 | 0.26 |
| *19H2-perf2* | 0.15 | 0.08 | 0.44 | 0.21 | 0.39 |
| *19H2-perf3* | 0.16 | 0.09 | 0.28 | 0.24 | 0.31 |
| *19H2-perf4* | 0.09 | 0.05 | 0.28 | 0.26 | 0.26 |
| *20H2-perf2* | 0.15 | 0.09 | 0.30 | 0.24 | 0.43 |
| *20H2-perf3* | 0.09 | 0.05 | 0.25 | 0.20 | 0.31 |
| *20H2-perf4* | 0.04 | 0.03 | 0.36 | 0.18 | 0.36 |
| *21H2-perf1* | 0.09 | 0.04 | 0.16 | 0.15 | 0.58 |
| *21H2-perf2* | 0.16 | 0.07 | 0.08 | 0.04 | 0.61 |
| *21H2-perf3* | 0.13 | 0.07 | 0.22 | 0.19 | 0.76 |
| *21H2-perf4* | 0.10 | 0.06 | 0.19 | 0.14 | 0.34 |
| *22H2-perf1* | 0.19 | 0.05 | 0.18 | 0.07 | 1.26 |
| *22H2-perf2* | 0.14 | 0.07 | 0.10 | 0.09 | 0.82 |
| *22H2-perf3* | 0.15 | 0.08 | 0.27 | 0.16 | 0.26 |
| *22H2-perf4* | 0.08 | 0.05 | 0.32 | 0.25 | 0.75 |
| *23H2-perf1* | 0.11 | 0.05 | 0.28 | 0.27 | 0.27 |
| *23H2-perf2* | 0.04 | 0.02 | 0.40 | 0.33 | 0.39 |
| *23H2-perf3* | 0.14 | 0.03 | 0.19 | 0.13 | 0.22 |
| *23H2-perf4* | 0.11 | 0.03 | 0.18 | 0.19 | 0.16 |
| *24H2-perf1* | 0.06 | 0.04 | 0.24 | 0.12 | 0.26 |
| *25H2-perf2* | 0.16 | 0.11 | 0.54 | 0.29 | 0.63 |
| *25H2-perf3* | 0.15 | 0.11 | 0.37 | 0.29 | 0.38 |
| *25H2-perf4* | 0.16 | 0.11 | 0.35 | 0.20 | 0.51 |
| *26H2-perf1* | 0.14 | 0.09 | 0.24 | 0.19 | 0.38 |
| *26H2-perf2* | 0.12 | 0.07 | 0.15 | 0.14 | 0.17 |
| *26H2-perf3* | 0.08 | 0.06 | 0.50 | 0.35 | 0.56 |
| *26H2-perf4* | 0.08 | 0.08 | 0.33 | 0.28 | 0.33 |
| *27H2-perf1* | 0.10 | 0.11 | 0.19 | 0.07 | 0.17 |
| *27H2-perf2* | 0.11 | 0.07 | 0.17 | 0.13 | 0.28 |
| *27H2-perf3* | 0.10 | 0.05 | 0.43 | 0.17 | 0.40 |
| *27H2-perf4* | 0.14 | 0.08 | 0.60 | 0.20 | 0.52 |
| *28H2-perf1* | 0.11 | 0.05 | 0.50 | 0.48 | 0.65 |
| *28H2-perf2* | 0.10 | 0.05 | 0.55 | 0.38 | 0.68 |
| *28H2-perf3* | 0.13 | 0.06 | 0.37 | 0.23 | 0.30 |
| *28H2-perf4* | 0.13 | 0.08 | 0.37 | 0.30 | 0.41 |
| *29H2-perf1* | 0.05 | 0.06 | 0.35 | 0.26 | 0.44 |
| *29H2-perf2* | 0.11 | 0.11 | 0.25 | 0.27 | 0.22 |
| *29H2-perf3* | 0.08 | 0.07 | 0.18 | 0.22 | 0.09 |
| *29H2-perf4* | 0.09 | 0.04 | 0.16 | 0.07 | 0.00 |
| *30H2-perf1* | 0.13 | 0.10 | 0.07 | 0.07 | 0.00 |
| *30H2-perf2* | 0.07 | 0.07 | 0.17 | 0.09 | 0.00 |
| *30H2-perf3* | 0.09 | 0.09 | 0.27 | 0.22 | 0.00 |
| *30H2-perf4* | 0.16 | 0.16 | 0.38 | 0.22 | 0.00 |
| *31H2-perf1* | 0.08 | 0.07 | 0.24 | 0.15 | 0.00 |
| *31H2-perf2* | 0.09 | 0.07 | 0.37 | 0.18 | 0.00 |
| *31H2-perf3* | 0.26 | 0.19 | 0.47 | 0.35 | 0.00 |
| *31H2-perf4* | 0.26 | 0.22 | 0.35 | 0.26 | 0.00 |
| *32H2-perf1* | 0.19 | - | 0.99 | - | 0.00 |
| *32H2-perf2* | 0.29 | - | 0.20 | - | 0.00 |
| *32H2-perf3* | 0.18 | - | 0.79 | - | 0.00 |
| *32H2-perf4* | 0.16 | - | 1.12 | - | 0.20 |
| *33H2-perf1* | 0.16 | - | 0.22 | - | 0.00 |
| *33H2-perf2* | 0.21 | - | 0.36 | - | 0.18 |
| *33H2-perf3* | 0.27 | - | 0.49 | - | 0.25 |
| *33H2-perf4* | 0.23 | - | 0.92 | - | 0.74 |
| *19H3-perf2* | 0.23 | 0.20 | 0.34 | 0.32 | 0.36 |
| *19H3-perf4* | 0.17 | 0.10 | 0.16 | 0.06 | 0.15 |
| *20H3-perf2* | 0.08 | 0.05 | 0.66 | 0.19 | 0.72 |
| *20H3-perf4* | 0.38 | 0.23 | 0.07 | 0.04 | 0.08 |
| *22H3-perf2* | 0.24 | 0.18 | 0.23 | 0.22 | 0.23 |
| *22H3-perf3* | 0.34 | 0.35 | 0.52 | 0.35 | 0.51 |
| *24H3-perf1* | 0.29 | 0.28 | 0.33 | 0.31 | 0.39 |
| *28H3-perf3* | 0.31 | 0.31 | 0.48 | 0.48 | 0.55 |
| **Average** | **0.15** | **0.09** | **0.34** | **0.21** | **0.32** |

average offset value for each group (small differences among the shots were corrected). The smallest offset, 215 m, (inner brown circle) shows the P-wave fastest velocity direction aligned with, approximately, N65ºE and eccentricity around 10%. With the increasing of the offset to 370, 490, and 570 m, the alignment of the fastest P-wave direction changes towards N5ºE - N5ºW while the eccentricity decreases to almost zero (no preferential azimuth), except in the farthest offset where it reaches its maximum around 30%. Table 3.2 summarizes the results of the walkaround study.

To interpret the results above mentioned, it is important to keep in mind that H1 has produced for 2.5 years before the perforation shots acquisition, lowering the Bakken Formation pore pressure. In the region of the well V3, in July of 2011, the Bakken Formation pore pressure was measured at 3945 psi (Dohmen et al., 2014) while the original pore pressure was assumed to be 6800 psi. Also, the pore pressure measured by the producer H1 was 2515 psi. This indicates that the nearby area to the well V3 has contributed to the H1 production.

Dohmen et al. (2014) suggest that the lowering of the pore pressure caused by the early production of the well H1 is heterogeneously distributed throughout the area. This interpretation is corroborated by the differences in the Bakken Formation pore pressure measured by other observation wells (V2, V5, and V6 have shown 6960, 7015, and 6843 psi, respectively, while V1 and V4 have shown 5020 and 4849 psi, respectively). Also, microseismic events triggered during the hydraulic fracturing of stages in the northern limit of H3 producer were recorded close to the heels' horizontals, in the southern limit of the producers' area. It was calculated that the increase in the sufficiently high to create new hydraulic fractures in the southern stages but, probably, big enough to reactive fractures early created by the H1 producer completion. This has led the authors to conclude that although H1 has produced the area heterogeneously, the fracture network created by its completion was pervasive enough to communicate a large area from the toe to the heel along the horizontals length (Figure 3.9a).

One way to grasp how connected is the fracture network created by H1 is to analyze the pressure variation in a well while hydraulically fracturing another one nearby

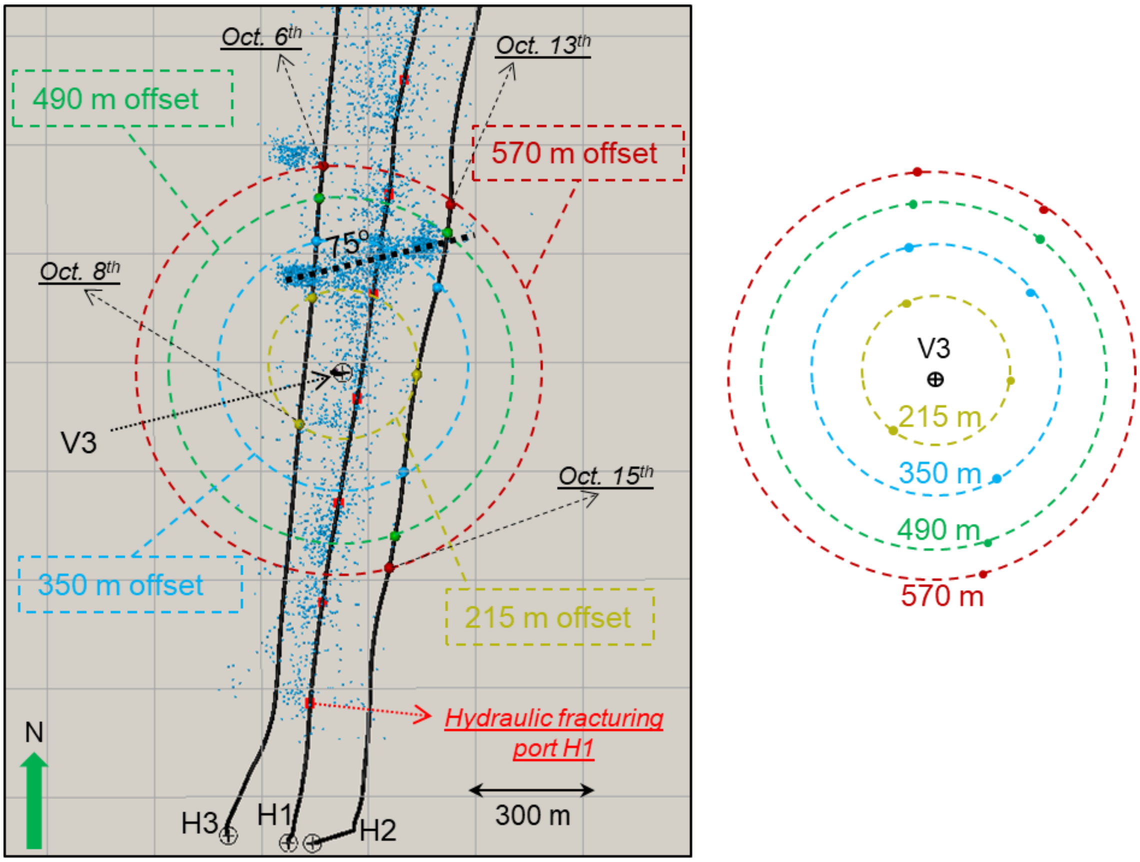


Figure 3.8: Map view of the VSP walkaround experiment. The well V3 was the well used in this exercise. Each offset, shown in different color, has three perforation shots. The absolute offset values are also shown. The dates of the first and last perforation shot of H2 and H3 used in the experiment are shown for comparison. The blue dots represent the recorded microseismic events and the 75° represents the average alignment of the microseismic events located 275 m above the reservoir depth. The red squares in the H1 represent its hydraulic fracturing ports. Note that a port of H1 is near V3. On the right side, only the shots and well V3 relative positions are shown, assisting the understanding of the geometry of acquisition.

(Dohmen et al.; 2014). Figure 3.9b shows the pressure variation measured by the gauge placed in the H1 well while the H3 well was being fractured. First, we can clearly see the low initial pressure recorded by H1 compared to the original pore pressure at the reservoir depth. Next, two distinct pressure build-ups are visible which are separated by an operational downtime caused by a mechanical issue of the perforation tool. Given the low permeability of the Bakken Formation, it is not expected to have a rapid diffusion of the pore pressure within large areas of the reservoir. Nonetheless, the pressure profile recorded by H1 shows a quick response to the stimulation of different stages regardless the distance between H1 and the stages of H3. Moreover, I do not see

Table 3.2: Calculated values for the P-wave fastest direction and its eccentricity for each formation according to the data of each offset.

| | Offset 215 (m) | | Offset 490 (m) | |
|---|---|---|---|---|
| | P fast direction (o) | P eccentricity (%) | P fast direction (o) | P eccentricity (%) |
| Charles | N66E | 12.3 | N3E | 6.3 |
| Mission Canyon | N66E | 11.3 | N3E | 8.5 |
| Lodgepole | N68E | 8.1 | N8E | 10.3 |
| | Offset 350 (m) | | Offset 570 (m) | |
| | P fast direction (o) | P eccentricity (%) | P fast direction (o) | P eccentricity (%) |
| Charles | N16W | 1.2 | N6W | 29.3 |
| Mission Canyon | N58E | 0.4 | N6W | 30.6 |
| Lodgepole | N66E | 3.8 | N4W | 30.4 |

seen the H1 pressure profile overcoming the minimum pressure needed to create new tensile fractures in the undepleted reservoir. Therefore, the microseismic events observed throughout the north to the south in the area can be explained only as the results of the reactivation of the fracture network created by H1, within the depleted reservoir, leading to the microseismic events caused by the slip of these fractures (Dohmen et al., 2014).

Similarly, Figure 3.10 shows the pressure profiles of three observation wells and 2 producers where possible connections among them, via fractures, may be interpreted. It shows the pressure build-ups recorded by the pressure gauges installed at the reservoir level in the wells V3, V4, and V6 during the hydraulic fracturing of the stages of H2 and H3. The correlation between pressure build-ups in the observation wells and the hydraulic fracturing of the stages in the producer wells can be unclear without another data that may corroborate this interpretation, a chemical tracer, for example. It seems that the pressure profile variations in the observation wells appear to be triggered by some specific stages but not all of them. This may point to the presence of a

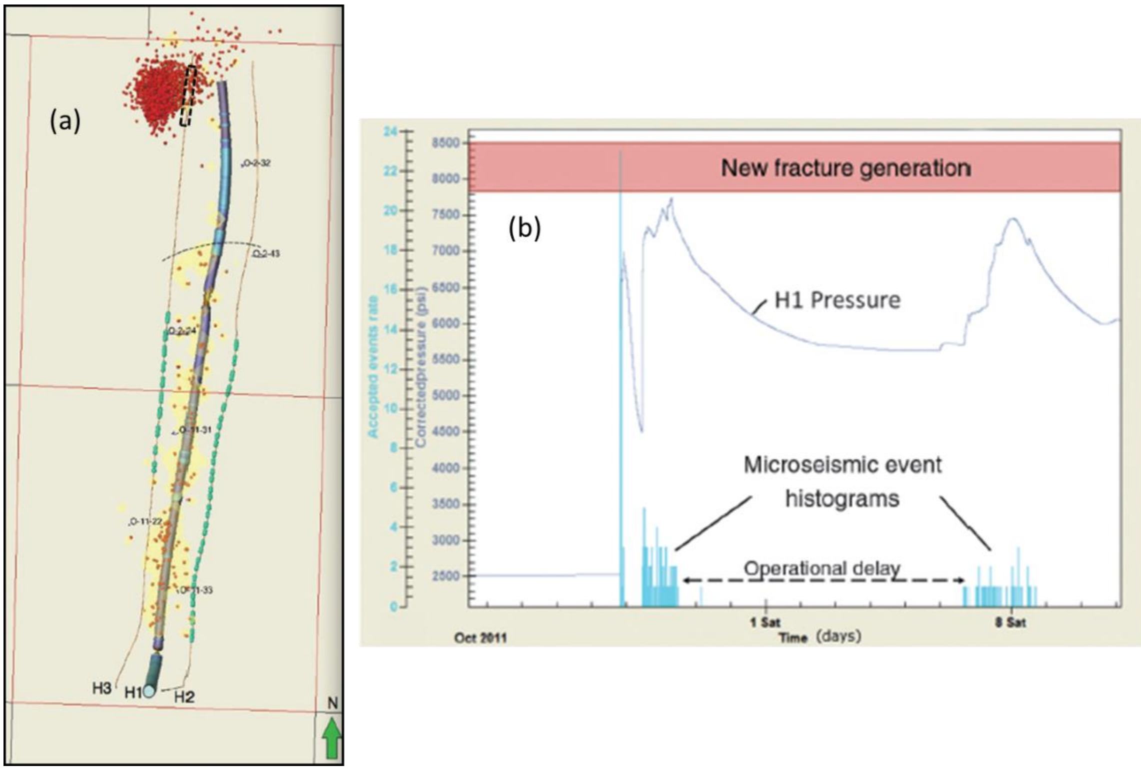


Figure 3.9: a) Map view showing the microseismic events distribution triggered by the stages of H3 located within the black dashed box. Although most of the events happened in the northern part of the survey (actually above the reservoir depth), some of them were located along all south length of the H1. This is interpreted as the product of the fractures reactivation created by H1, 2.5 years early. b) Plot showing the response of the pressure in the H1 during the hydraulic fracturing of the H3 and H2. Note that the pressure in the H1 has not reached the pressure threshold necessary to create new tensile fractures leading to the reactivation of the fractures created by H1 as the explaination of the microseismic events in the south part of the area. The length of the side of the red square in the map view is one mile. The coordinates are not provided due to the confidentiality terms (modified from Dohmen et al., 2014).

heterogeneous fracture network, in term of intensity and distribution, early created by H1. The spatial distance between the observation vertical wells and the different stages of the producers varies. Apparently, the nearest vertical well to a stimulated stage does

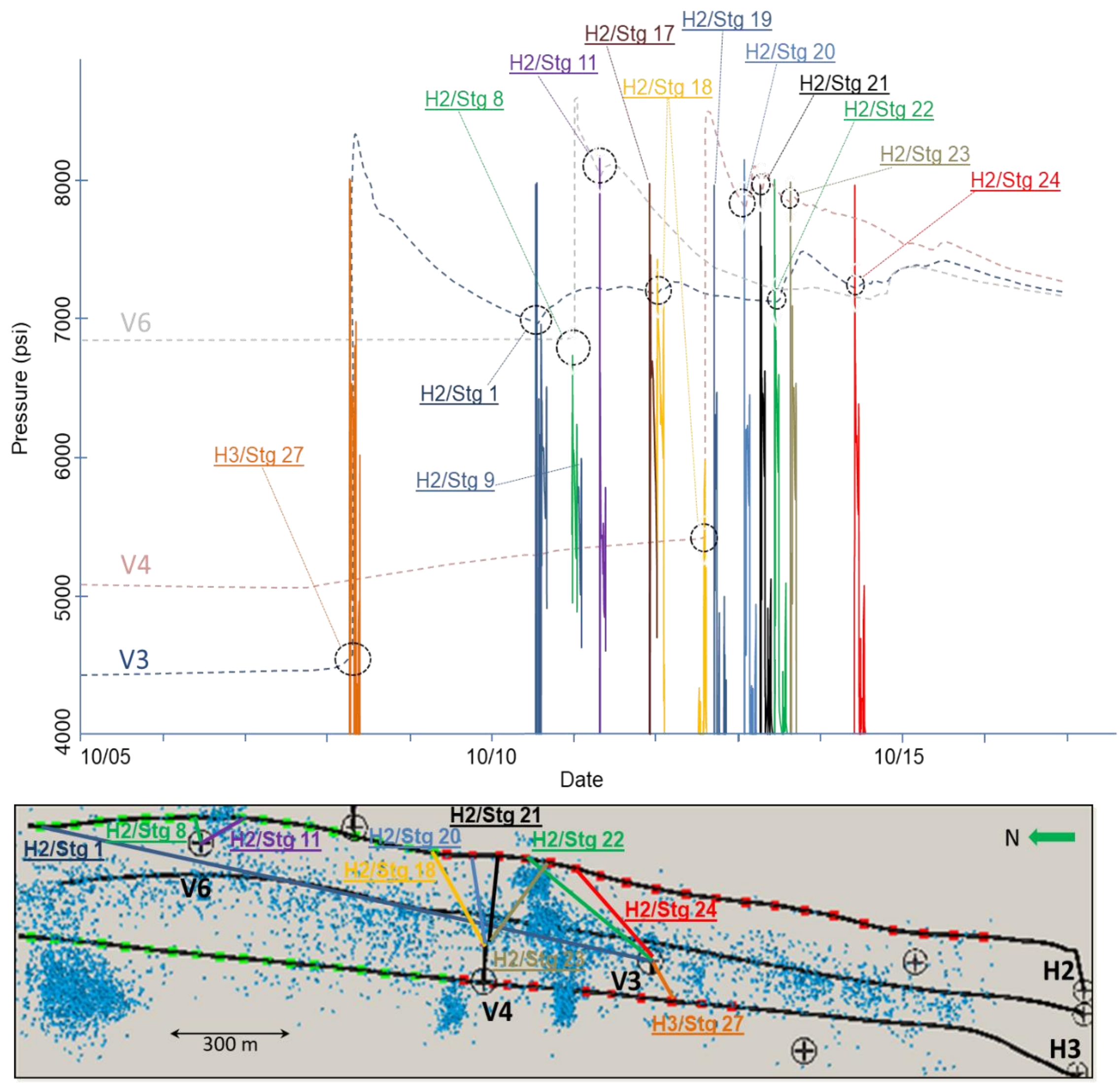


Figure 3.10: a) Plot showing the pressure build-ups in the observation wells, V3, V4, and V6 during the hydraulic fracturing of some stages of H3 and H2. Note that some abrupt responses in the observation wells almost at the same time of the fracturing of some stages. The fracturing of some stages changes the declining pressure trend in the observation wells. b) Map view showing the position of the fracturing stages and their correspondent affected observation wells. The color-code of the build-ups in the pressure plot and the names of the stages in the map view is the same to make easier the stage identification. The pressure of the stages was measured at the surface. The coordinates are not annotated due to the confidentiality terms.

not necessarily show a pressure build-up which could be associated to the stimulation of this stage. The same can be said about the azimuth defined by the alignment between the vertical well which recorded a pressure build-up and the stimulated stage interpreted as the one that caused the pressure increasing. This azimuth is not constant.

Therefore, observing that some of most northern stages were able to trigger microseismic events at the south limit of the area (Figure 3.9a) and associating this to a heterogeneous azimuth pattern in the pressure build-ups within Bakken Formation (Figure 3.10), we conclude that an irregularly fractured volume, initially caused by H1, is present throughout the area. We interpreted the variation of our results with regards to the direction of fastest P-wave velocity azimuth (from N65$^{o}$E, in the smallest offset, to N5$^{o}$W in the farthest offset) and in terms of the P-wave velocity eccentricity (the largest eccentricity is found at the farthest offset) as a consequence of this heterogeneity.

Partially, this heterogeneity can be caused not only by the fracture network created by H1, 2.5 years early, but also by H2 and H3. This argument raises a concern about the validity of putting perforation shots in the same offset group regardless when each perforation shot was triggered during the hydraulic fracturing campaign. Perforation shots triggered at the first stages of the campaign, in H3, may sample a formation less affected by the hydraulic fracturing carried out by H3 and H2, compared to the perforation shots triggered at the last stages of H2. The dates when the first and last perforation shots used in the walkaround study, for each one of the horizontal wells, are shown in Figure 3.8. This information helps to determine how long the perforation shots are apart, which may be critical considering the effect that the pressure can have in keeping the fractures opened once the hydraulic pressure is not applied anymore (Figure 3.9b).

On the other hand, the smaller is the offset, the higher is the chance of the fractured network to be homogeneous. In this case, the pressure variation imposed by the hydraulic fracturing throughout the rock volume may be faster and evenly equalized.

My results corroborate other studies' findings. Yang and Zoback (2014) showed, at the same area, that microseismic events, triggered during the stimulation of 3 stages in the horizontal H2, present focal mechanisms with a mix of normal and strike-slip components. These events are located at Lodgepole Formation, approximately 275 m (900 feet) above the Bakken Formation (Figure 3.8). Events in the Bakken Formation were also analyzed showing similar focal mechanisms. In their calculation, they assumed the fault' strike equal to N75ºE which was derived from the general alignment of the microseismic event cluster located in the Lodgepole/Mission Canyon formations. The dip and rake were then calculated using the P-wave first arrival sign and the results pointed out to a preexistent set of fractures. Such fracture set was interpreted as the expression of the conjugate plane of the normal/strike-slip regime assumed for the area, with the SHmax aligned to N50ºE. This preexistent set of fractures would be responsible for the connection between the Bakken Formation and Mission Canyon Formation with the hydraulic fluids being transmitted to the upper levels, triggering microseismic events in the Lodgepole and Mission Canyon formations. Interesting to notice that the strike azimuth assumed in their analysis is quite close to our fastest P-velocity azimuth results for the smallest offsets (215 and 350 m). The area within these two offsets encompasses most of the microseismic events located in these formations showing that the preferential alignment of the microseismic events is similar to our fastest P-velocity azimuth results.

Another study in the area carried out by Grechka et al. (2017) shows the moment tensor inversion results for some microseismic events selected at the same cluster analyzed by Yang and Zoback (2014). Comparing the moment tensors obtained using only V4 data and V4 and V5 data combined (Figure 3.11), they showed results indicating that the fracture's strike values are varying from approximately N50ºE (events located

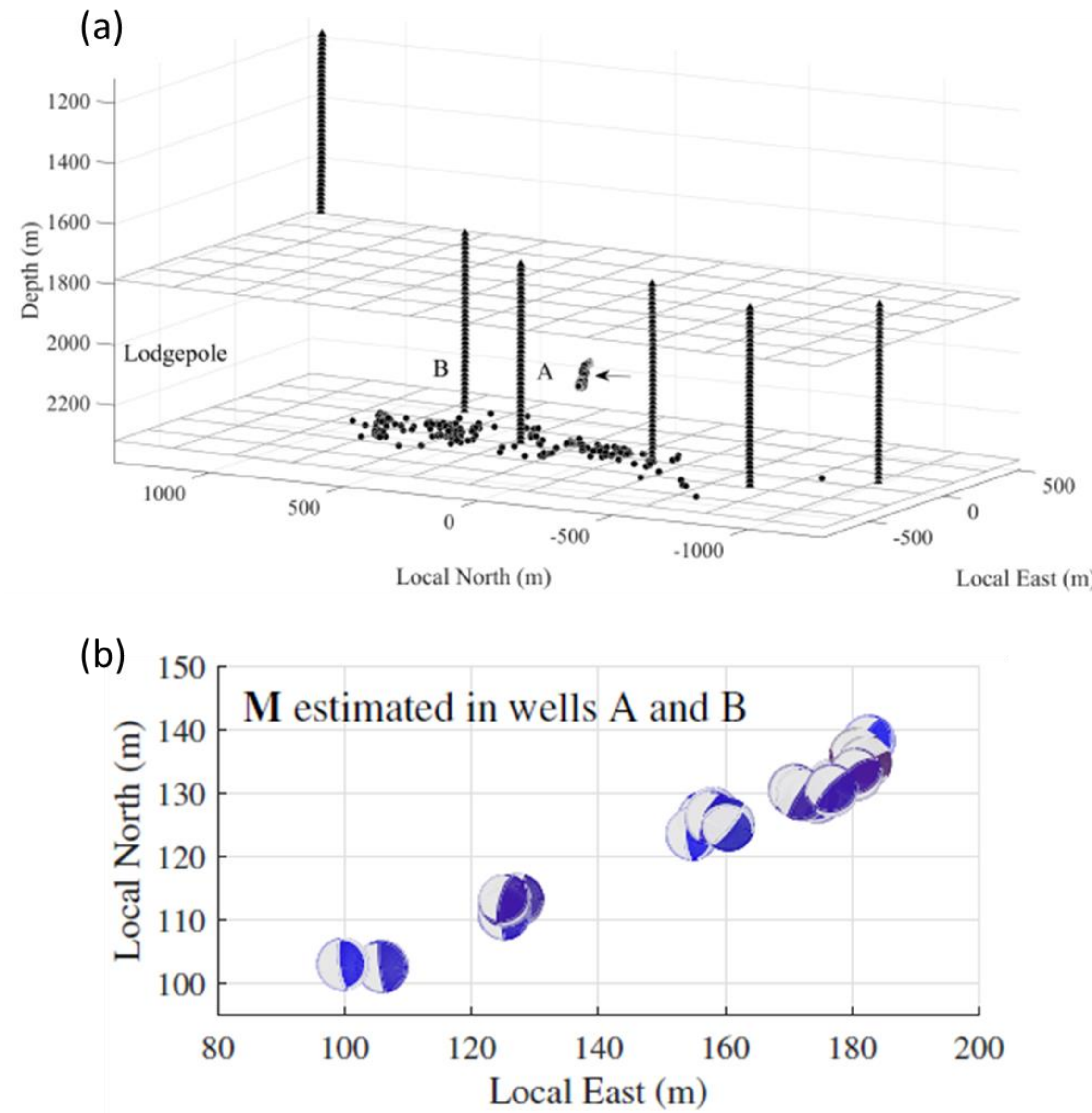


Figure 3.11: a) 3D diagram showing the geometry acquisition and the microseismic events (black arrow) whose moment tensors were inverted. The inversion was carried out using the data acquired the wells A (V4) and B (V5). b) Beach balls showing the results of the moment tensor inversion of the 19 microseismic events. Note that eastern events have strikes oriented approximately to N50$^{o}$E while those at closer to the west side have strikes oriented approximately to N10$^{o}$W The coordinates are not annotated due to the confidentiality terms (modified from Grechka et al., 2017).

close to the east side of the microseismic cluster) to N10$^{o}$W (events located close to the west side of the microseismic cluster). These values are consistent with our result which varies from N65$^{o}$E (smaller offsets) to N5$^{o}$W (larger offsets).

Another explanation for the approximately north-south orientation of fractures can be related to the proximity of the study area to the Nesson Anticline (Figure 3.1) which has its hinge line oriented approximately north-south. The hinge zone is a preferential place for extensional fractures and joints formation since this is a highly stressed area. The study area is not placed in the Nesson Anticline hinge zone but is it located in the base of its east limb which is mild folded, forming an incipient synclinal-like structure. Using the same argument of the preferential fractures formation in the anticline hinge zone, the mild folded region where the study area is located may also show fractures/joints north-south aligned but such joints are not visible in the 3D seismic P-wave (Figure 3.12).

Although we are more confident that the fastest P-velocity azimuth, identified using our nearest offsets, is more likely to be related to the preexistent preferential fractures´ strike, such correlation is not so direct when we compare the N10$^o$W strike events, identified by Grechka et al. (2017), with our farthest offset (570 m) results, which show the fastest P-velocity azimuth equal to N5$^o$W. In the case of the farthest offset, its eccentricity value is quite high compared to the eccentricity of the other offsets and it may be caused by differences in the fracture density. As explained before, this difference may arise from the use, in the same offset group, of P-waves from perforation shots acquired during the stimulation of the early and last stages of the hydraulic fracturing campaign. P-waves acquired during the hydraulic fracturing of the first stages might have sampled a less fractured formation compared to last perforation shots recorded. Therefore, larger offsets may encompass areas large enough to sample a kind of heterogeneity which has more to do with the moment that each perforation shot was acquired, during hydraulic fracturing campaign, than the preferential fracture strike direction.

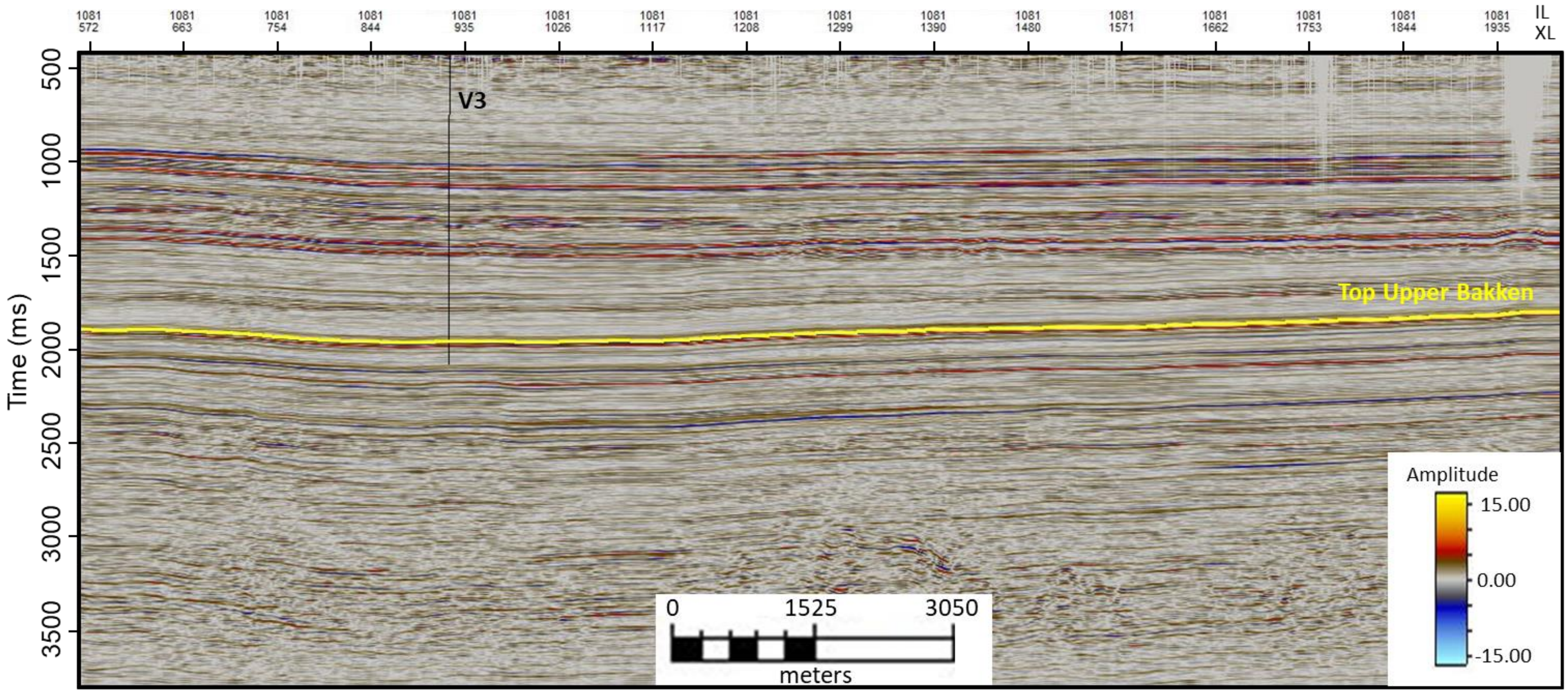


Figure 3.12: Seismic inline oriented west-east (south view) passing at the V3 position. Note the mild concavity where the V3 is located. This is the end of the east limb of the Nesson Anticline (not shown in the seismic image) mapped, approximately, 1 mile to the west. Such smooth structure may create fractures and faults aligned with the hinge line of the Nesson Anticline which is oriented approximately north-south. Although this is a possible explanation for results indicating azimuthal P-velocity differences aligned north-south, fractures and faults aligned to this direction are not visible on seismic. The vertical exaggeration is 20. The distance between crosslines is 33.5 m. The coordinates and depth are not annotated due to the confidentiality terms.

### 3.5 WALKAWAY STUDY USING PERFORATION SHOTS

Another experiment carried out using the perforation shots was the analysis of the anisotropy in the area before and after the hydraulic fracturing using the reverse VSP walkaway geometry. The purpose of this experiment was to access the changes in the anisotropic parameters of the near-reservoir and far-reservoir overburden due to the hydraulic fracturing of the Bakken Formation. In this experiment, I assumed that the media follows the Vertical Transverse Isotropic (VTI) model of anisotropy.

For that purpose, I looked for a set of perforation shots with the geometry of acquisition which would more plausibly separate the expected elastic property changes due to the hydraulic fracturing of the stages. I decided that the part of the whole survey area which more likely promotes the separation of these changes is located over the horizontal H2, on the east side of the survey (Figure 3.13). The perforation shots triggered from the stage 19 to 33 in this horizontal were recorded by the geophone arrays in the vertical V1 and V5 at the same time. The horizontal section of the H2 and the location of the observation wells V1 and V5, projected on the map, are approximately aligned along a straight line. Since the hydraulic fracturing jobs were performed from north to south, the direct P-wave arrivals recorded by well V1 should be less affected by the fractures created by the previous hydraulically fractured stages than those arrivals recorded by well V5. The locations of the perforation shots of H2 regards to the V1 and V5 locations located, respectively, to the south and north in relation to the H2 stages, explains this effect. Carrying out two reverse VSP walkaway studies, separately, with the P-wave direct arrivals acquired by each vertical well opens the possibility to calculate the Epsilon($\varepsilon$) and Delta ($\delta$) Thomsen parameters and evaluate what is the effect of the fracturing in the formations.

To use the perforation shots in the anisotropy estimation of the near- and far-overburden formations, we split the overburden data according to the two of the formations of the area, namely, Lodgepole and Mission Canyon formations instead of working with each geophone as one layer level. Working with the geophones within each

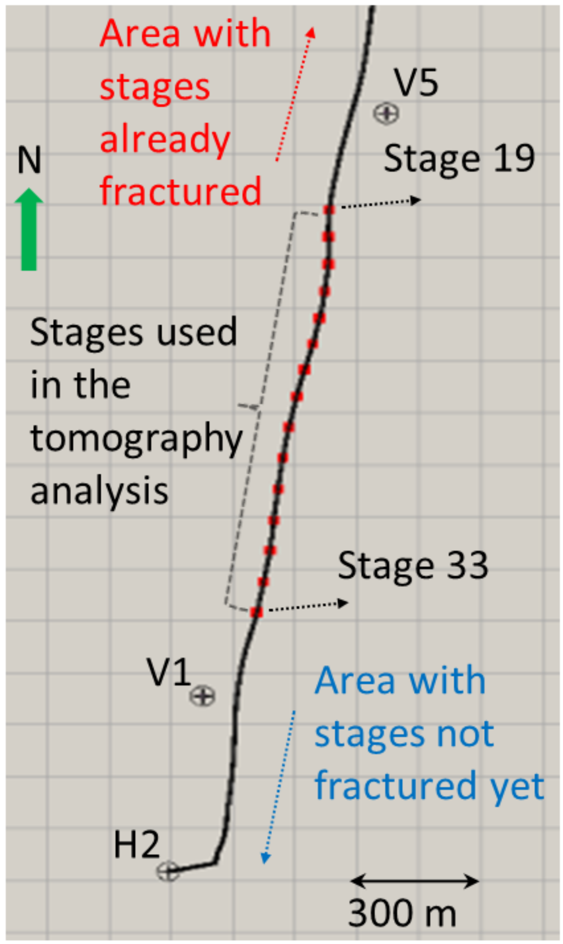


Figure 3.13: Map view showing the H2 stages whose perforation shots were used in the tomography study. As the fracturing sequence started from the north and went to the south, the wavefield front acquired by well V5 was more affected by the fractures since the stages toward north have been already fractured while the wavefield recorded by well V1 sampled the area before the stages have been hydraulically stimulated. The coordinates are not annotated due to the confidentiality terms.

formation as a unit helps to increase the number of sensors in each studied formation which, in its turn, increases the range of the angle of incidence of the seismic rays that pass through each formation. That is valid as long as the formations show themselves as roughly uniform units regards to the P-velocity (Figure 3.2 – blue box region for Lodgepole Formation and orange box for Mission Canyon Formation).

Therefore, in the case of the well V5, I used 13 receivers for both Lodgepole Mission Canyon formations (180 m). The selection of the receivers within the formations focused on sampling the largest possible length of each formation without overlapping each other. In the case of the well V1, the same method of selection of the receivers was used although just the even receivers (20) were available due to operational issues with the geophone array. Therefore, the interval between the geophones was 30 m and only seven receivers were used in the Lodgepole and Mission Canyons formations, while keeping the same investigated length for each formation. The range of depth investigated at wells V1 and V5 is shown in Figure 3.2 (blue box region for Lodgepole Formation and orange box for Mission Canyon Formation).

Figure 3.14 shows the P-wave direct arrivals of 15 perforation shots recorded by well V5 after a band-pass filtering (65 – 85 – 480 – 500 Hz) and the data rotation using 3 components. Each perforation shot shown was triggered in one of the stages used in the VSP walkaway experiment, i.e. one shot per stage from stage 19 to 33. The P-wave direct arrivals are visible which helps to reduce error in the picking of the P-wave wavelet. The P-wave direct arrivals recorded by well V1 show similar quality, but, as mentioned before, only 20 receivers of the V1 geophone array were used in the VSP walkaway experiment.

For the well V5, the number of shots used was 53 and for the V1 it was used 50 shots. The difference in the number of shots comes from the perforation shots of the stage 25 which were not recorded by V1. For both wells, each point of analysis was

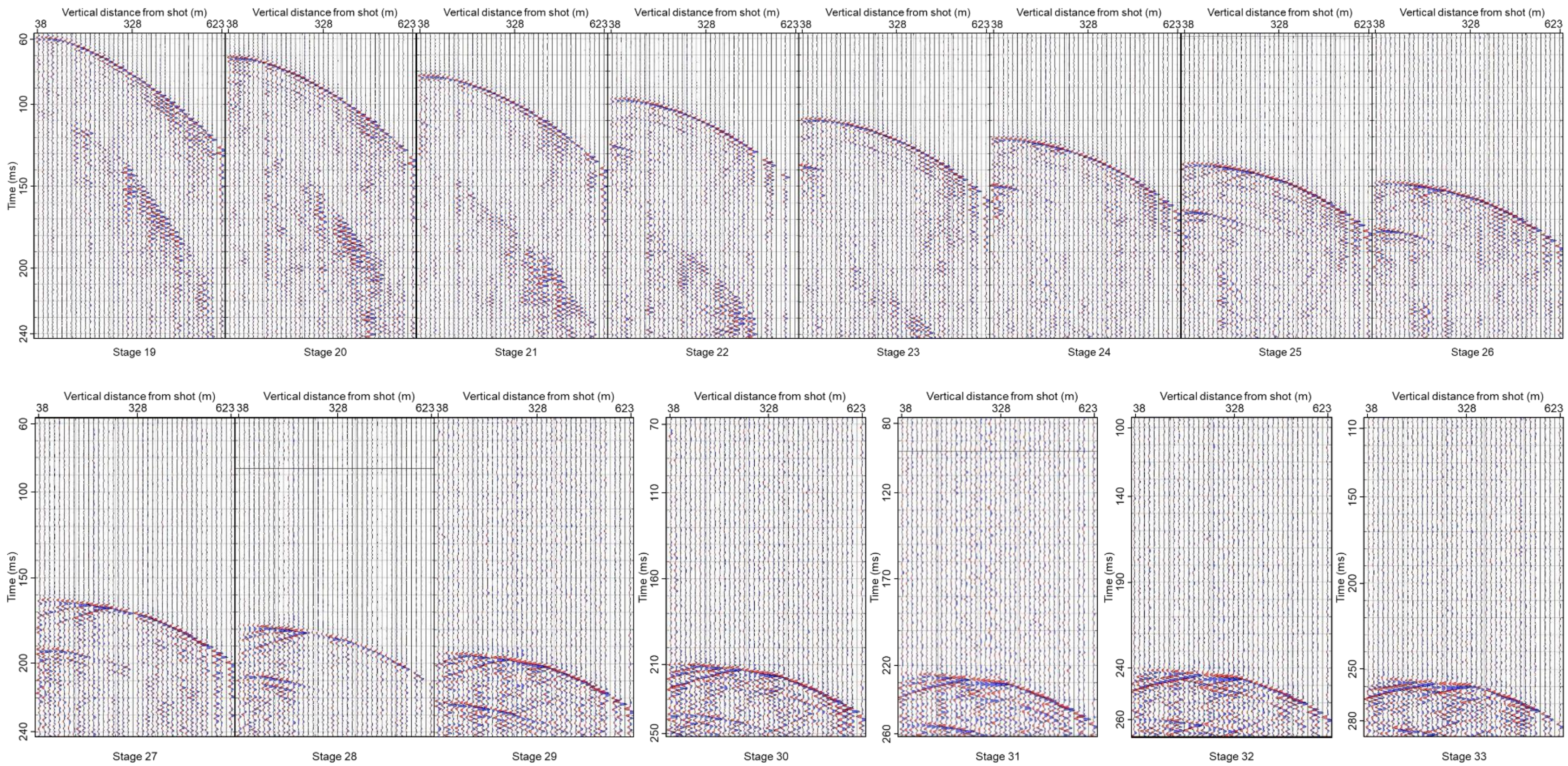


Figure 3.14: P-wave direct arrivals of 15 shots, one per stage, recorded by well V5. Note that the direct arrivals are clear promoting a more precise picking process of the P-wave direct arrivals wavelets. The data were band-pass filtered (65 – 85 – 480 – 500 Hz) and rotated using the 3 components. The amplitude was normalized shot by shot to enhance the P-wave direct arrivals.

calculated by averaging 13 shots which yields, approximately, a 300 m window for the average process. The averaging of shots and receivers helps to stabilize the calculation and reduce the effects of small uncertainties in the picks in the results.

In this walkaway experiment, only the anisotropic parameters ε and δ were calculated while the vertical P-velocity was given as an input to the process. The vertical P-velocity for each formation was calculated using the zero-offset VSP data acquired in the well V3. The VSP vertical velocity profile is preferred in this experiment since both perforation shots and VSP data show similar frequency content, decreasing the chances of differences in the velocities due to the dispersion effect. The vertical P-velocity for Lodgepole and Mission Canyon formations were, 5650 m/s and 5850 m/s, respectively.

I used for this experiment the VSP walkaway analysis option of the RockDoc software from the Ikon Company. The software deals with the different layers removing the influence of the previous ones (layer stripping) so that the calculated anisotropy for each layer responds only to the intrinsic anisotropy of one specific layer. The analyzed layers are assumed to be laterally uniform in terms of vertical P-velocity and anisotropy parameters by the software. The software uses the weak anisotropy approximation defined by Thomsen (1986).

Given the times of the direct arrivals of the P-wave and the geometry of the survey, the vertical and horizontal slownesses are calculated as a function of the incident angle. Finally, with the slownesses and the vertical P-velocity, the ε and δ parameters are obtained. In the case of isotropic homogeneous media, the slownesses are equal because ε and δ are equal to zero and the representation of both slownesses in the Cartesian Coordinates Plane (vertical slowness in the vertical axis and horizontal slowness in the horizontal axis) forms a circle. Otherwise, with different values for the slownesses, in an anisotropic homogeneous media, the representation differs from a circle and is equal to an ellipse if the ε = δ but ≠ 0 (zero). Mathematically, the approach used here can be summarized in the following equations:

$$S_p(\theta) \approx \frac{1}{V_{P0}}(1 - \delta \sin^2\theta \cos^2\theta - \varepsilon \sin^4\theta) \quad 3.2$$

$$S_x(\theta) = S_p(\theta) \sin\theta \quad 3.3$$

$$S_y(\theta) = S_p(\theta) \cos\theta \quad 3.4$$

where $S_p(\theta)$ is the slowness vector and the $S_x(\theta)$, and $S_y(\theta)$ are the components of the slowness vector all as a function of the angle of incidence θ, and $V_{P0}$ is the vertical P-velocity (Thomsen, 2002).

Figures 3.15a, 3.15b (Lodgepole Formation), 15c, and 15d (Mission Canyon Formation) show the horizontal and vertical slownesses in the Cartesian Coordinates Plane for each formation before and after the hydraulic fracturing, i.e. the calculation was done with the data acquired by the observation wells V1 (before) and V5 (after) separately. Note that due to the geometry of acquisition, most of the rays are much closer to the horizontal than to the vertical propagation. In turn, the ε parameter has less uncertainty since its influence is stronger in the horizontal direction. On the other hand, the δ parameter estimate is more questionable as the vertical direction, where its effect is stronger, is poorly sampled. Also, it is important to keep in mind that the vertical P-velocity is calculated based on a zero-offset VSP data of the nearby well V3 and not from the actual positions of the observation wells V1 and V5. Therefore the absolute values of ε and δ should be interpreted with caution but the comparison of ε and δ values before and after the hydraulic fracturing may indicate how the presence of the fractures modify broadly the P-velocity in the media.

Figures 3.15a and 3.15b show the results of the Lodgepole Formation using the data of well V1 (before) and V5 (after), respectively. The calculated ε parameter was

0.08 before fracturing and 0.05 after fracturing. In the case of δ, the calculated values were 0.21 before and 0.04 after fracturing.

Figures 3.15c and 3.15d show the results of the Mission Canyon Formation. The calculated ε value was 0.05 before and 0.02 after fracturing while the calculated δ was 0.09 before and -0.01 after fracturing. The values for ε and δ are, in general, within the range of values of anisotropic parameters found by other authors for the same area (Huang, 2016; Grechka et al., 2017).

Comparing the values obtained before and after the hydraulic fracturing of both formations, it is visible the slightly decreasing in the values of ε, and a more substantial decreasing in the δ values, after the hydraulic fracturing. As mentioned before, the effect of δ parameters has a small influence in the slowness vector since the geometry of acquisition favors the propagation closer to the horizontal plane. The lack of vertical rays is even clearer in the Lodgepole Formation.

Because the absence of the nearly vertical rays may lead to larger uncertainty in the δ values results, I decided to not consider the δ in my interpretations. The variation observed in the δ values is far bigger than the variation observed in the ε parameter. As the hydraulic fractures created are expected to be vertical due to the larger vertical stress value compared to the other two horizontal stresses in the area, in principle, variation in δ should be less than in ε. That is because ε is more sensitive to the vertical fractures while δ is more sensitive to the layer bedding structure or horizontal fractures. Although there are cases that horizontal fractures are also created associated to the vertical fractures, during the hydraulic fracture (Rutledge et al., 2016; Grechka and Yaskevich, 2014), the lack of reliable data along all angles of incidence turns this interpretation speculative.

On the other hand, differently from the typical incident angle coverage of rays acquired in the surface seismic, predominantly vertical, our data have more access to horizontal rays yielding more reliable inputs to calculate ε. Moreover, since the hydraulic fractures expected should be vertical, the ε parameter should represent better the changes in the media elastic properties imposed by the hydraulic fracturing. Because of these arguments, my interpretation focuses on the ε results.

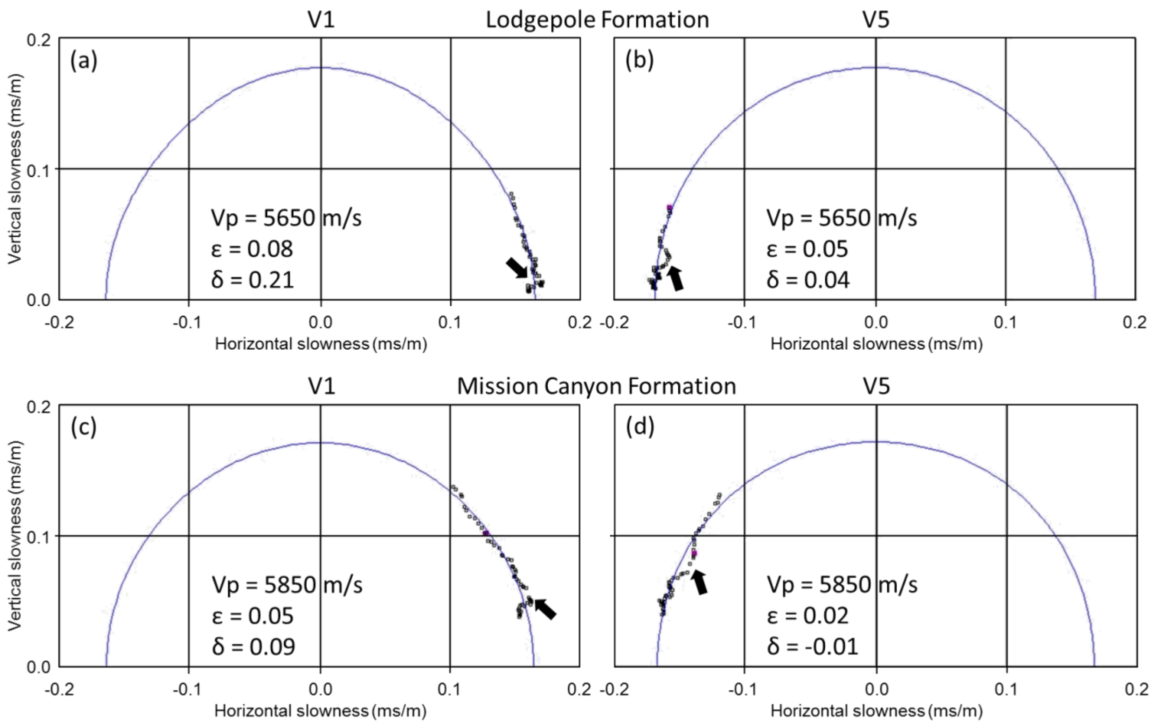


Figure 3.15: Anisotropic parameters ε and δ results derived from the VSP walkaway analyses before fracturing (well V1 - (a) Lodgepole Formation and (c) Mission Canyon Formation) and after fracturing (well V5 – (b) Lodgepole Formation and (d) Mission Canyon Formation) of the stages 19 to 33 of the producer H2. A reduction in the values of the anisotropic parameters is observed after hydraulic stimulation.

The decrease in ε values after the hydraulic fracturing can be understood as an overall decreasing of the P-velocity parallel to the horizontal plane since the vertical P-velocity is kept constant as one of the inputs of the calculation. Note that the ε value decreases 0.03 in both Lodgepole and Mission Canyon formations; although the

Lodgepole Formation is slightly more anisotropic than Mission Canyon Formation. The slower P-velocity after the hydraulic fracturing is compatible with the interpretation of the reduction of P-velocity, possibly caused by the vertical fractures created during the fracturing process. There are regions, as at the stages 21, 22, and 23 of the producer H2, where microseismic events have occurred 900 feet above the Bakken Formation indicating natural fractures reaching depths, at least, as high as the bottom of the Mission Canyon Formation (Yang and Zoback, 2014). Therefore, reactivated natural fractures or new fractures created during the hydraulic fracturing can be the source of the P-velocity reduction.

Another point is some sharp variations in the horizontal slowness indicating that the P-velocity parallel to the horizontal plane is not constant and varies laterally. This information is important since lateral velocity variation may be correlated to the density of the fractures created during the hydraulic fracturing process, which, in its turn, can tell something about the efficiency of the fracturing process itself.

## 3.6 DISCUSSION

I have found results which are in agreement with the results of other studies as, for example, the P-wave fastest direction with, approximately, the same orientation of the fracture strikes calculated from the microseismic data (Grechka et al., 2017 and Yang and Zoback, 2014). Also, the lateral variation of $\varepsilon$ values observed in my findings can indicate that the P-velocity lateral variation is correlated to the fracturing process.

Nonetheless, the elastic property variations, P-velocity for instance, are not easily measured by other methods. Seismic surveys designed to measure the changes in the elastic properties due to the hydraulic fracturing have not effectively shown these changes, at least in this area. In the case of the well logs data, which are measured closer to where the hydraulic fracturing takes place and with tools with much higher resolution, they do not seem able to identify such changes.

Figure 3.16 shows a VSP walkaround study, carried out by Huang (2016) and Figure 3.17 shows a set of fast and slow S-sonic logs. The well logs and the VSP were acquired in the well V3. These data sets were collected after approximately 2.5 years of production of the producer H1 but before the hydraulic fracturing of the producers H2 and H3. So, it is not adequate to directly compare our results with these two data sets.

Nonetheless, it is reasonable to assume that the surrounding area of the V3 has been fractured and produced by H1, given the low pressure measured by V3 compared to the original pore pressure, from 6800 psi to 3945 psi (Dohmen et al., 2014), and the rapid pressure build-up measured by V3 during the hydraulic fracturing of some stages of H2 and H3 (Figure 3.10). Moreover, one of the hydraulic fracturing ports of the H1 is

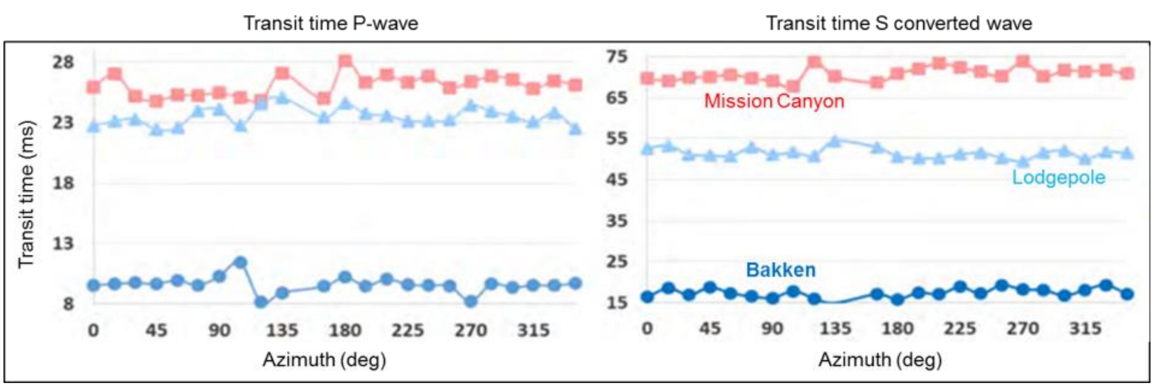


Figure 3.16: Transit time within each formation, namely, Mission Canyon, Lodegpole, and Bakken, for P- and converted SV-wave along different azimuths. The data was acquired at well V3 as a VSP walkaround survey. Note that both transit time, P- and converted SV-wave, do not show variation with the azimuth which could be interpreted as caused by a preferential fracture direction. In such case, consistent ups and downs in the transit time would be visible (modified from Huang, 2016).

quite close to the V3 position which helps to corroborate the idea that this area was produced (Figure 3.8). Therefore, even before the hydraulic fracturing of the producers H2 and H3, some effects of the hydraulic fracturing of H1 around V3 should be apparent.

The VSP walkaround carried out in V3 and studied by Huang (2016) had 23 shots recorded around V3, i.e. one shot at each 15° of azimuth, starting from the north. The nominal offset was about 1680 m (5500 ft). Figure 3.16 shows the transit time within the Mission Canyon, Lodgepole, and Bakken formations for the P-wave and converted SV-wave in different azimuths. A preferential fracture direction would cause the transit time of a wavefront passing orthogonally to it to be increased due to the lower velocity along the direction perpendicular to the fractures' strike. Parallel to the preferential fracture direction, this effect would be minimized and smaller transit time (faster velocity) would be expected. It turns out that the predicted transit time pattern is not visible in any formation. Neither in the P-wave nor in the SV-wave transit times. A possible explanation for that result can be, again, the lack of a preferential direction in the propagation of the hydraulic fractures which seems to be unlike given the presence of oriented natural fractures in the area; although their effects may be rather localized. Nevertheless, the dominant frequency needed to measure thin fractures may be much higher than that available in a regular VSP walkaround survey.

Well logs data can illustrate of how troublesome the identification of the hydraulic fracturing effects in the formations may be. Li et al. (2017) show how the near condition of a hydraulically fractured well can be a hurdle to the identification of the fracture preferential direction using fast and slow S-sonic well logs.

In our case, despite the pressure data indicate that the V3 area was produced, Figure 3.17 shows the slow and fast S-sonic logs with approximately the same readings, leading to no preferential fracture direction identification. Different fast and slow S-waves readings would be visible if the hydraulic fracturing process has opened the fractures parallel to maximum horizontal stress ($Sh_{max}$) direction. One explanation could be the similarity in the maximum and minimum horizontal ($Sh_{min}$) stresses which may lead to no

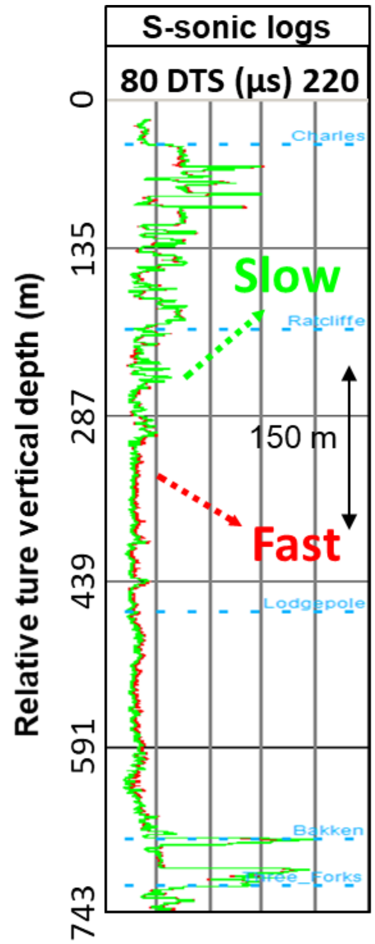


Figure 3.17: Fast and Slow S-sonic well log of the well V3 show no difference in the reading between them even after 2.5 years of production of producer H1 nearby located. The production of H1 is associated to its hydraulic fracturing and the pore pressure decline measured by well V3 (3945 psi in 2011 while the original pore pressure is assumed to be around 6800 psi) confirms that the area was produced. Nonetheless, differences between Fast and Slow S-sonic logs are not visible which do not confirm the presence of fractures aligned in a specific direction. The actual true vertical depth is not annotated due to the confidentiality terms.

preferential direction in the fracture opening (small anisotropy stress). Apparently, the microseismic event locations, separated per stage, tend to concentrate as point clouds rather than in linear features, corroborating this explanation. However, the $Sh_{min}$ and $Sh_{max}$ difference (about 1500 psi, before depleted) for the area (Dohmen et al., 2014) is not irrelevant. Another way to explain this apparent divergent result is to assume that although the low pressure measured in V3 may result from the H1 production, the fracture network created by its hydraulic fracturing was not pervasive enough to reach V3 borehole wall. The V3 surrounds may have been depleted during the 2.5 years of H1 production, even with the limited fracture network created by the hydraulic fracturing treatment, assuming that, given a period of time long enough, the slow pressure diffusivity in the low permeability medium would not be an unpassable obstacle to deplete the region. If these characteristics are true, the use of the well logs to measure the presence of hydraulic fractures is limited.

It is necessary to say that the results that I have found using the VSP walkaway technique have limitations. The first point is the lack of P-wave direct arrivals propagating closer to the vertical direction, i.e. normal to the layering of the formations. This fact imposes more uncertainty on the $\delta$ calculation, being the reason why I decided to not use it in my analysis.

Another point is that the vertical P-velocity is assumed constant within each formation. Although this is not a bad approximation given the low variation of the P-sonic well log data, small variations can increase the uncertainty of the results.

Also, the inversion process for the anisotropic parameters of each layer considers them laterally constant. It is visible in Figure 3.15 (black arrows) that the horizontal slownesses of some perforation shots show sharp variations in the data acquired by observation wells V1 and V5 which are characteristics expected when lateral velocity variations are present in the media. These variations may be indicative of the P-wave velocity variation due to the hydraulic fracturing of the formations, assuming that the propagation of the fractures is likely heterogeneous and the hydraulic fracturing of the horizontal H1 might have previously created heterogeneity in the area. To solve that problem, it is necessary to locate spatially where these lateral velocity changes are occurring. With that goal, I decided to perform a 3D anisotropic tomography analysis using the V1 and V5 P-wave direct arrivals data and correlate the tomography result with the H2 production logging tool data. The idea behind this correlation is to verify if the lateral P-velocity variation is a valid property to map the hydraulic fracturing efficiency and, consequently, could be translated in higher production for some of the stages in H2. These results are shown in Chapter 4.

### 3.7 CONCLUSIONS

The statements below summarize the findings of this chapter:

- The zero-time for the perforation shots used in the VSP walkaround and walkaway analyses were calculated showing small overall misfits for P- and SV-waves meaning that the hyperbolic approach, described in Chapter 2, is accurate.
- The VSP walkaround results of the smallest offsets show that the fastest P-wave velocity is in agreement with the direction of the strike of the natural fractures interpreted in the area. This is expected since that the P-wave traveling parallel to the fractures' strike tend to be faster than any other direction
- The VSP walkaway results show values for ε and δ parameters in agreement with the values found by other authors in the area. The ε results show that after the hydraulic fracturing its value was reduced indicating a reduction in the P-velocity traveling parallel to the horizontal plane. This P-velocity reduction is interpreted as caused by the hydraulic fractures propagation into the Lodgepole and Mission Canyon formations.

# Chapter 4

# 4D overburden effects from hydraulic fracturing using P-wave anisotropy tomography

Continuing with the use of the direct P-waves generated by the perforation shots, I undertook an analysis using 3D P-wave anisotropy tomography with the data acquired by well V1 and V5. In this chapter, I show the tomography results and correlate them with the Production Logging Tool (PLT) data available for the producer H2. I show that the tomography technique was able to capture the lateral P-velocity variation caused by the hydraulic fracturing of the H2 well. The use of P-wave data acquired by V1 and V5 made possible to image the same overburden area twice, before and after H2 had been hydraulically fractured. The differences between the tomography results from wells V1 and V5 correlated well with the PLT.

## 4.1 INTRODUCTION

As I shown in Chapter 3, lateral P-velocity variations are apparent. Sharp variations in the horizontal slowness, from the VSP walkaway analysis, using the direct

P-wave arrival of different shots acquired by V1 and V5 wells may indicate velocity variations along the raypaths. These heterogeneities cannot be correctly located in space using the VSP walkaway technique which assumes flat layers, each one with a constant velocity.

Given the possibility of the occurrence of this heterogeneity described above, I undertook 3D grid-based anisotropic tomographic procedure using the P-wave direct arrival traveltimes from the perforation shots. The objective was to identify possible lateral heterogeneities that could be correlated to the hydraulic fracturing process using grid tomography with size cell compatible with the ray coverage available in our data. I focused on the well H2 area which could show the most of the time-lapse difference before and after the hydraulic stimulation. Therefore, I used the same shots and receivers used in the VSP walkaway analysis discussed in Chapter 3 (Figure 3.13). Moreover, the production data of the well H2 was available in the area of the perforation shots used, allowing for comparison between the tomography results and oil production data. This is an interesting way to corroborate the effectiveness of the hydraulic fracturing in various locations of the H2 well.

The tomography studies were performed using the workflow described in Figure 4.1. The software used in tomography studies was the VSP 3D grid-based anisotropic tomography algorithm, available in the Paradigm Software Suite. The grid-based tomography performs the point-to-point ray tracing technique aiming to minimize the traveltime difference between the measured from the calculated traveltime. The measured traveltime is obtained from the picks of direct arrivals of P-wave mode. The calculated traveltime uses, in its calculation, the initial P-velocity model within each grid cell crossed by the rays defined by the point-to-point ray tracing technique. The initial velocity model is updated over a number of iterations until the difference reaches the

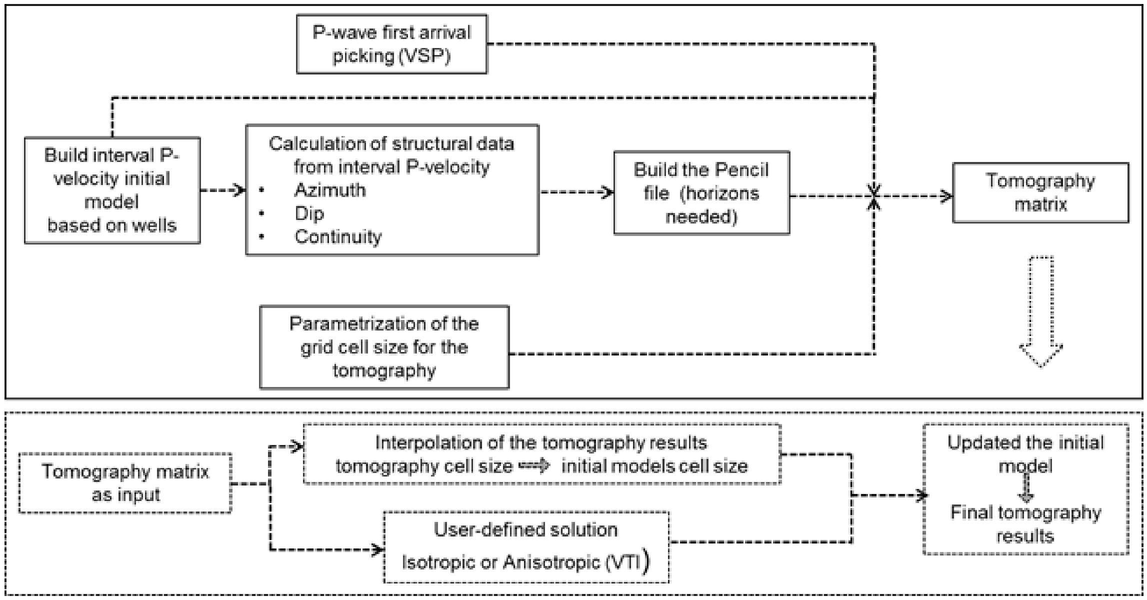


Figure 4.1: Workflow of the tomography study performed with V1 and V5 wells data according to the VSP 3D Grid-based Anisotropic Tomography algorithm, available in the Paradigm Software Suite.

threshold previously defined. In this process, to avoid spurious results, the algorithm refuses rays which show angles with the normal too different from the average angle calculated from the other rays. Seismic rays propagating too close to the refraction angle are also avoided. The Tomography Matrix construction, the solving of the tomography equations in each cell of the tomography grid, and the interpolation of the tomography results accordingly to the grid of the initial velocity model were performed by this algorithm. Additionally, other steps of the workflow, as the calculation of the structural data (Dip Azimuth, Dip, and Continuity) and the Pencil File, were carried out in the GeoDepth Software, also available in the Paradigm Software Suite. The Pencil File works as the database file responsible for input different data in the Tomography Matrix construction process. The initial velocity model was constructed using the Schlumberger Petrel Software. In the Petrel software, the horizons were obtained by the interpolation of the markers interpreted using the well log data. These horizons were used to establish the structural framework of the P-velocity initial model. Finally, the P-velocity initial model cube was calculated also using the Petrel Software via Kriging interpolation of the P-Sonic well log data available with the interpolated horizons defining the layering and structural framework.

The first input that needs to be provided is the initial P-velocity model. To incorporate the structural characteristics of the layering in the model, interpreted horizons of the area have to be used in the P-velocity model building process. It turned out that the horizons available in the area, interpreted using the surface seismic, did not show almost any dip variability. It is well accepted that the area shows a mild regional dip (between $0.5^{o}$ to $1.0^{o}$) towards the south (Dohmen et al., 2014; Grechka et al., 2016). Since the layers in the area seem to be quite flat, some local variations could not be represented if I have used the interpreted horizons using the surface seismic. As I am dealing with a small area with nine wells quite close to each other, I decided to use the top makers of some formations interpreted by the Hess Corporation personnel using the wells logs and interpolate them using a Minimum Curvature algorithm to create the horizons and the structural framework. Six horizons were interpolated using their respective top markers which, from top to the bottom, are Top Charles, Base of Last Salt, Rival, Base of Lodgepole, Top of Upper Bakken, and Top of Three Forks.

The horizons were used as structural framework trend for the P-velocity interpolation using the well logs available in the area. This interpolation was performed with an exponential isotropic Kriging algorithm with a horizontal variogram range of 400 m (approximately the distance between the wells) and 5 m for the vertical variogram range. The small vertical variogram range was necessary to preserve thin layers with high P-velocity contrast to their boundary layers. After the Kriging interpolation, the P-velocity cube of the area was converted to the SEG-Y format with the distance between

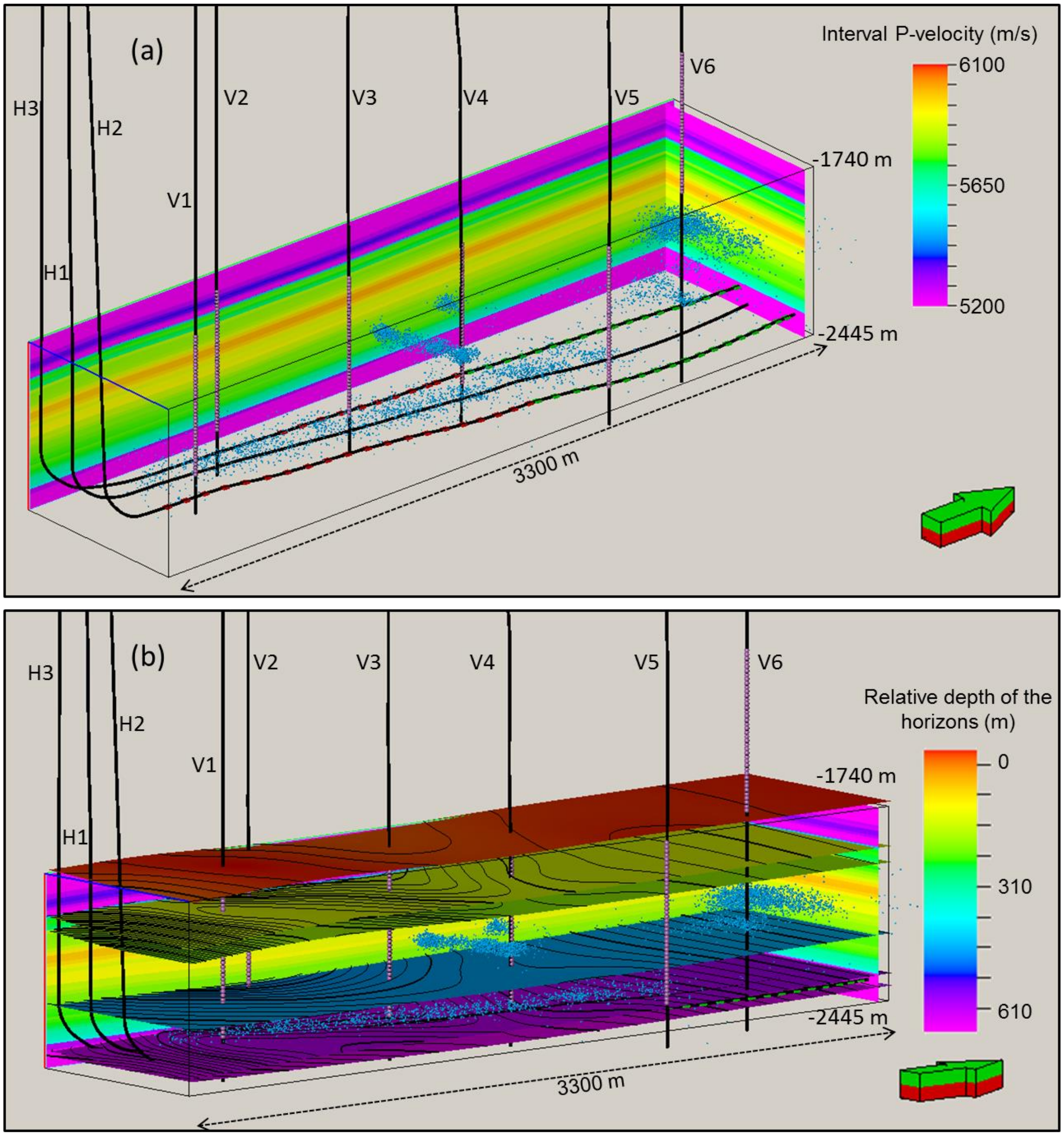


Figure 4.2: (a) 3D isotropic P-velocity initial model based on the Kriging interpolation of the P-sonic well logs and (b) the horizons used as structural frame to the interpolation. The blue dots are the microseismic events recorded in the whole survey. The purple dots in the vertical wells represent the geophone positions at each well. The red (perforation shot completion) and green (ball sleeve completion) dots represent the position of the stages at well H2 and H3. The coordinates are not annotated due to the confidentiality agreement. The depth is annotated in sub-sea true vertical depth.

both inlines and crosslines equal to 10 m and time sampling equal to 0.5 ms (Figure 4.2).

It is noteworthy that the calibration of the V3 well sonic-log with the checkshot acquired at the same well (43 checkshot points with 15 m of interval between them which totalize 630 m of logged length) has shown that only small corrections were needed to calibrate the well log data. The residual drift of the P-sonic log before the calibration was -1 ms and after the calibration with the checkshot data oscillates around 1.2 ms over the area of the Bakken, Lodgepole, and Mission Canyon formations. This means that the initial P-velocity model based on the P-sonic well logs is a good start for the tomography ray tracing; even though the frequency bandwidth of the P-sonic logs is an order of magnitude larger than the checkshot data. Such small difference between their integration times indicates that the area is characterized by a low dispersion effect in the propagation of the high-frequency components of the P wavefield within these formations (Figure 4.3).

From the P-velocity initial cube, three attributes were calculated, namely, the Dip, the Dip Azimuth, and the Continuity (Figure 4.4). They were sparsely sampled throughout the cube in order to capture the structural behavior of the area. The Dip and Dip Azimuth attributes show the values of the dip and the dip direction of the layers, locally, i.e., at specific points defined by the sparse sampling process. The Continuity attribute is a measure of the lateral continuity of the layers and is also only calculated in these sparse defined points. The sparse sampling process defines how the Pencil File will be populated with values from the Dip Azimuth, Dip and Continuity attributes. As explained before, the Pencil File collects the attributes information and it is used as input to the Tomography Matrix construction. These attributes, the P-velocity initial cube, and direct arrivals of the P-wave time pick data were yield to the algorithm so that the Tomography Matrix could be built. The Tomography Matrix is the collection of all tomography equations for each cell within the tomography grid. The tomography grid is

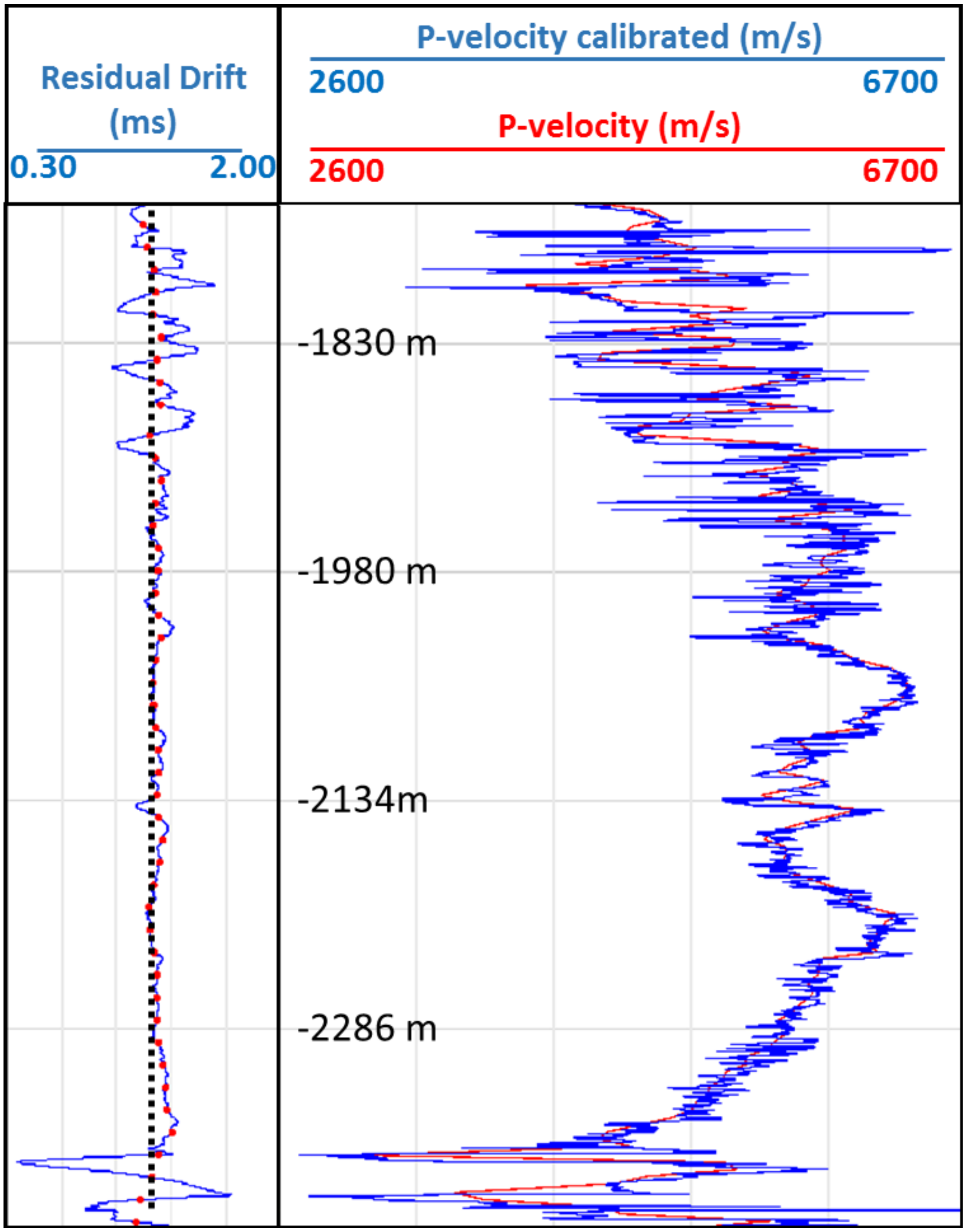


Figure 4.3: P-sonic log calibration using the VSP zero-offset data acquired in the well V3. Note that the residual drift after the calibration oscillates around 1.2 ms. This suggests that the dispersion effect over the Bakken, Lodgepole, and Mission Canyon formations is small making the 3D interval P-velocity initial model derived from the P-sonic logs interpolation a good start model for the tomography studies. The coordinates is not annotated due to the confidentiality agreement. The depth is annotated in sub-sea true vertical depth.

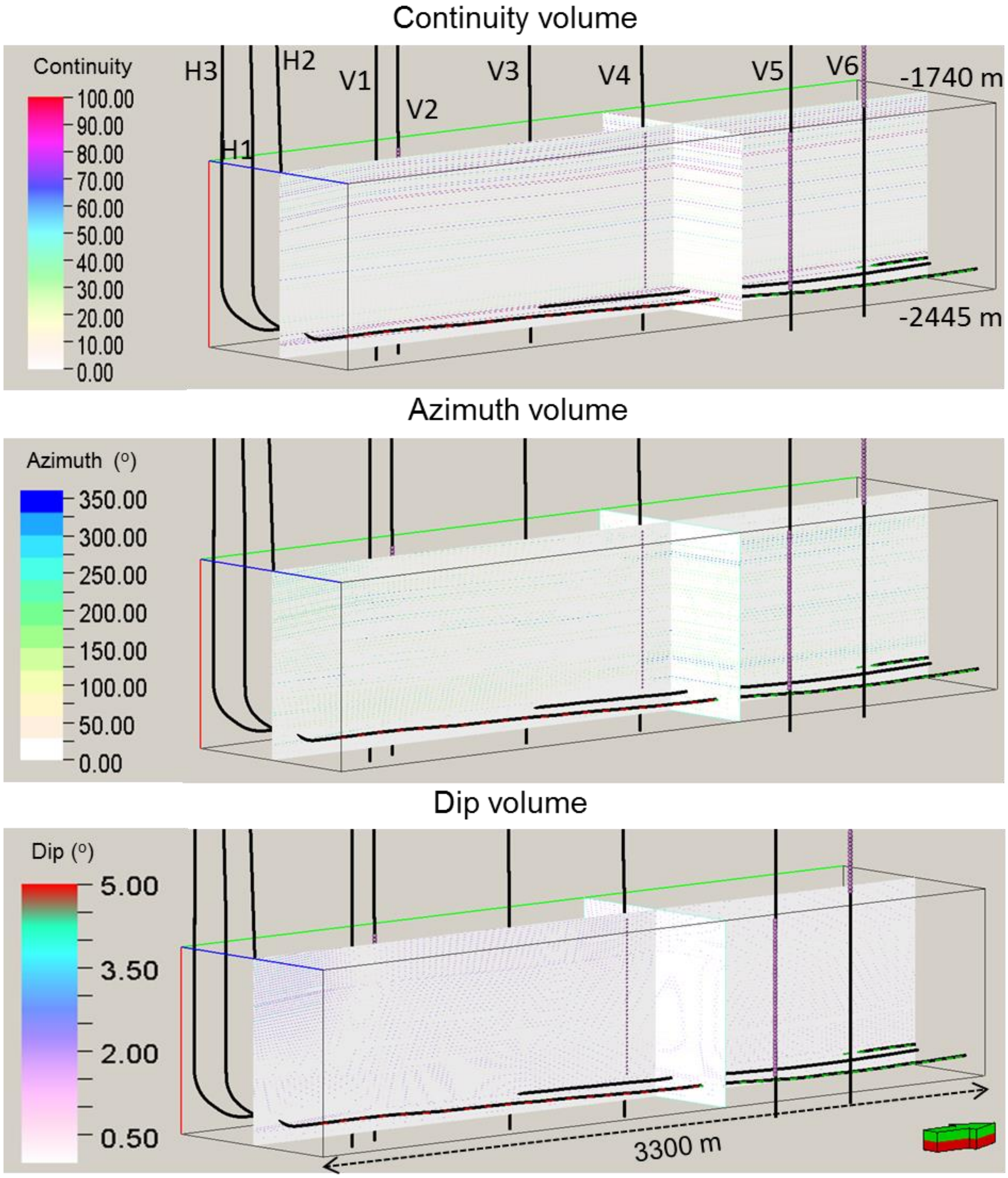


Figure 4.4: The Continuity, Azimuth and Dip of Azimuth volumes extracted from the initial 3D P-velocity model. They are sparse sampled and are used to populate the Pencil File with properties which are used in the Tomography Matrix construction. The coordinates are not annotated due to the confidentiality agreement. The depth is annotated in sub-sea true vertical depth.

spatially defined by the size of the whole volume which is meant to be ray traced and solved by the tomography process and by its cell size. The size of the cell, which is a cube in this approach, is an important parameter which is intimately linked to the resolution expected to be reached and it is dependent on the seismic ray coverage of the cells throughout the area. Therefore, the use of a small cell, seeking higher resolution, must be counterbalanced by denser ray coverage of the cells over the ray tracing process. With these considerations in mind, smearing artifacts, for instance, can be avoided. In my case, I decide to use the cell with 70 m of side and 10 m of height. Another factor which should be taken into account is the amount of memory available for the tomography job. In general, tomography is a computationally demanding process, so that the size of the cells should be parameterized accordingly.

## 4.2 TOMOGRAPHY RESULTS

As mentioned before, my criterion to select the perforation shots used in the tomography study was to select those that could measure the effects of the creation of new fractures. Thus, I could image the same stages before and after the pressure build-up in each stage, following the sequence of the stages' hydraulic fracturing which, ultimately, defines the geometry of our P-wave direct arrival acquisition.

Due to this choice of the perforation shots, I ended up with a geometry which yields two lines, both similar to a walkway geometry. Looking closely at the yield geometry, it can be seen that these two walkway lines do not fall exactly on the same line due to the slight misalignment between the wells V1 and V5 and the line of the perforation shots within the horizontal section of H2. This has obliged us to deal with the tomography as a 3D problem instead of 2D; although the size of the cell of 70 m used in both tomography studies (before and after fracturing) practically corrects this problem making both tomographies to be spatially located at the same region.

The well V5 recorded P-wave direct arrivals from 53 perforation shots whose wavefronts propagated to the north; therefore after the hydraulic fracturing. The well V1 recorded the P-wave direct arrivals from 50 perforation shots, propagating to the south; therefore before fracturing. This difference in the total number of perforation shots recorded by each observation well was caused by an operational problem with the geophone array located in the well V1 which did not record 3 perforation shots from stage 25. Also, 40% of the perforation shots recorded by V1 only acquired 20 receiver levels instead of 40 levels due to operational issues during the acquisition. The average relative traveltime error for well 5 tomography was -3.3% while for the well 1 was +1.5%.

Figure 4.5 shows the result of the P-wave tomography carried out using the data acquired by observation wells V1 (a) and V5 (b). For comparison, the initial P-wave model is also shown (c).

The P-wave tomography results, generated with the data acquired by the well V1, a lowering in the P-velocity values, compared to the initial model, detected near V1, within a volume that extends from Middle Bakken Formation to approximately the top of Lodgepole Formation (black dashed square - Figure 4.5a). The reduction is around 3% to 5%. Halfway between the wells V1 and V5, within the region just above the horizontal section of producer H2 (base of Lodgepole Formation), an increase of approximately 4% in the P-velocity was detected (black dashed ellipse - Figure 4.5a).

Analyzing the results of the P-wave tomography achieved using the data acquired by the observer V5, a region showing higher P-wave velocity, compared to the initial model (around 4% to 5% higher), is identified and pointed out in the Figure 4.5b (black dashed ellipse).

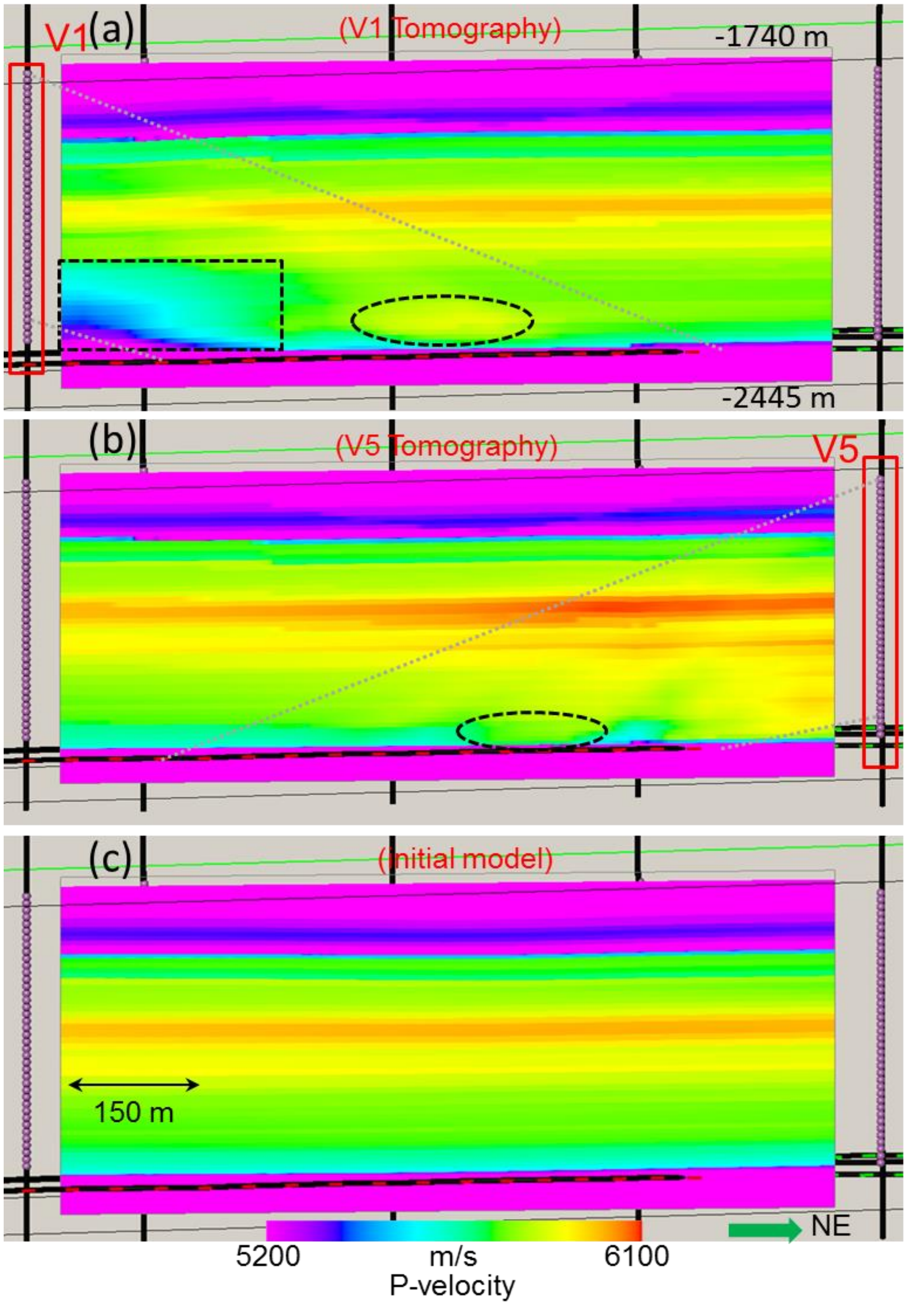


Figure 4.5: a) Tomography result with the input data acquired by V1. Note the lower P-velocity nearby the observer V1 (black dashed box) and higher P-velocity halfway between V1 and V5 (black dashed ellipse). b) Tomography result with the input data acquired by V5. Note the higher P-velocity in the area marked by the ellipse compared to the initial model in c. c) P-velocity initial model based on the well logs and horizons. The depth is annotated in sub-sea TVD. The gray-dashed lines in a) and b) represent the area where the seismic-ray coverage is adequate for the tomography study.

I subtracted the V1 from the V5 tomography results (Figure 4.6) to access the differences between both studies and analyze possible 4D effects. These differences could, eventually, show the effects of hydraulic fracturing in the Lodgepole bottom and top of Bakken formations, where the densest ray coverage is available. The differences were compared to the PLT (Production-Logging Tool) data, shown by Dohmen et al. (2017), making possible the interpretation of my results in light of the relative production level of some stages of the producer H2.

Nonetheless, a valid interpretation of my tomography results requires us to keep track of the ray-paths which effectively crossed the area analyzed. Figure 4.7 shows the

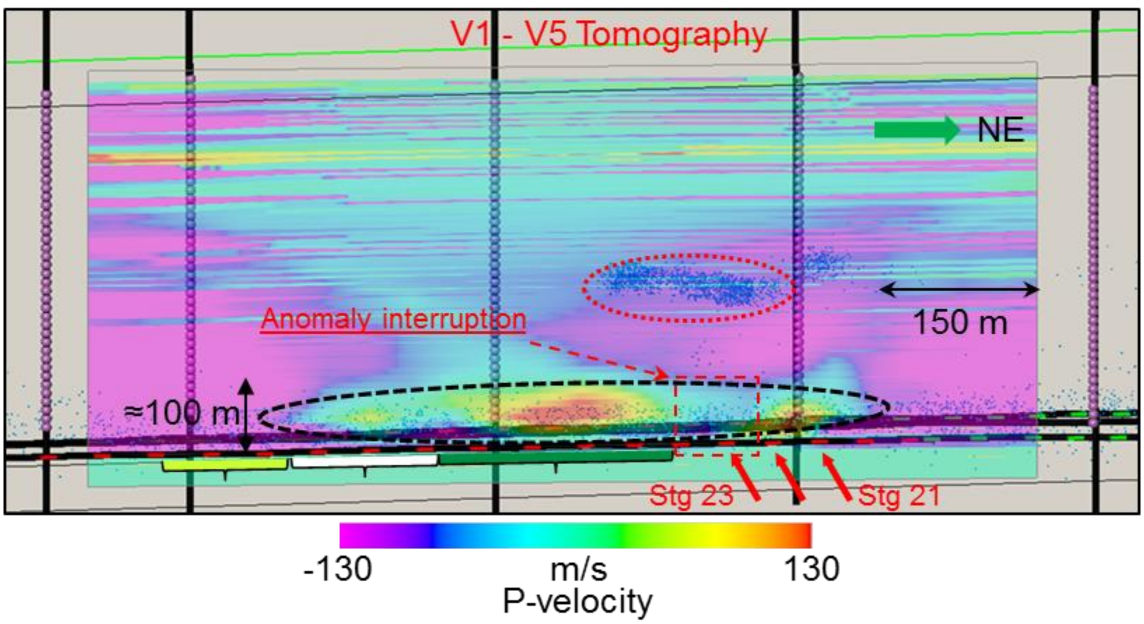


Figure 4.6: The result of the V1 tomography minus V5 tomography. The positive anomaly, indicating the decrease of the P-velocity after the hydraulic fracturing, coincides with the stages that have shown larger production (area marked by the green bracket) while the stages less prolific show anomaly with negative values (area marked by the white and light-green brackets). The brackets are shown in Figure 4.8 signaling different stages according to their relative production level. The red dashed square marks the area where the anomaly is interrupted. The red arrows mark the stages which are associated with the natural fracture reactivation. The interruption vertically coincides with the cluster of microseismic events marked by red ellipse. These events are interpreted as the result of deviation of the hydraulic fluids by the natural fractures to upper formations, triggering them during the reactivation process.

raypaths from all perforation shots to some of the receiver levels used by the two tomography studies. Figures 4.7a and 4.7b show the ray-tracing results for V1 and V5 tomography studies, respectively. Just some of the raypaths are shown. Otherwise, if all of them were shown, they would block the view of the differences between the tomographies. The raypaths for the receivers located at upper levels in the observation wells, shown in the figures, are spaced 105 m which means that there are other six receivers between them. Between the two lowest receivers shown in the figures, there are another three receiver levels. Below the lowest receiver level, there are another four receiver levels, although these receivers do not contribute much to the images. The

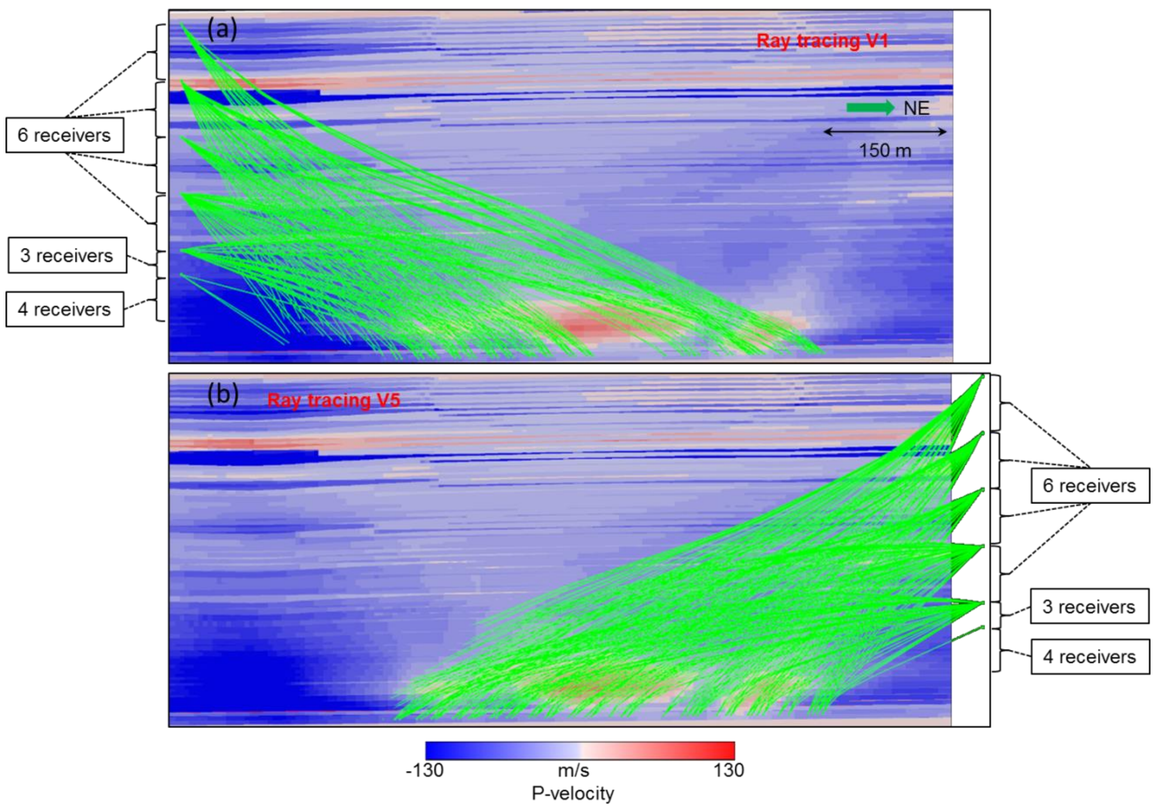


Figure 4.7: a) Section showing the ray tracing coverage of all perforation shots acquired by six receivers of the geophone array of the observer V1. The rays overlay the result of the V1 tomography minus V5 tomography. Note that the positive anomaly resultant of the V1 minus V5 images is well sampled by the rays shown. b) The same image as in a) but using the data acquired by observer V5. The numbers in the box indicated how many receivers are not shown among those which are shown. Not all rays of every receiver are shown so the positive anomaly could be seen.

reason for that is the restriction imposed by the algorithm which limits the valid rays accepted in the tomography considering a quality factor based on their properties such as the traveltime difference between nearby rays and their angle of emergence.

Dohmen et al. (2017) used the b-values, calculated from different microseismic data sets of Bakken Formation, to identify depleted pore pressure zones. They suggest that the b-values can be used as variables to delineate depleted zones since the events with higher magnitude seem to be more frequent in depleted zones, lowering the b-value. The explanation for this phenomenon is that stronger events are more frequent in depleted areas where the differential stress is larger, promoting their occurrence. Fortunately, one of the data sets used in their study was acquired in our area of study. Figure 4.8 shows a comparison between the PLT data (green disks) with the amplitude of the events (orange disks) triggered during the hydraulic fracturing of stage 4 of the producer H3, placed in the northern part of the H3 horizontal section. It is visible that the largest events in amplitude have occurred close to the H2 horizontal segment whose stages have shown smaller production. This is interpreted as a consequence of the early production carried out by producer H1, from 2009 to 2011, which has lowered the pore pressure in the area in an irregular fashion due to the heterogeneity in the creation of new fractures over its hydraulic fracturing, leading, hence, to some stages produce more than others.

The tomography result carried out with the data acquired by V1 shows a reduction in the P-velocity values compared to the initial velocity model near the V1 area (Figure 4.5a - black dashed square). We interpret this decrease in P-velocity as the result of a pervasive fracture creation due to a more efficient hydraulic fracturing process during the H1 completion. This has led to a higher production of H1 in this region with the consequent lowering of the pore-pressure of the Bakken Formation nearby V1 and to

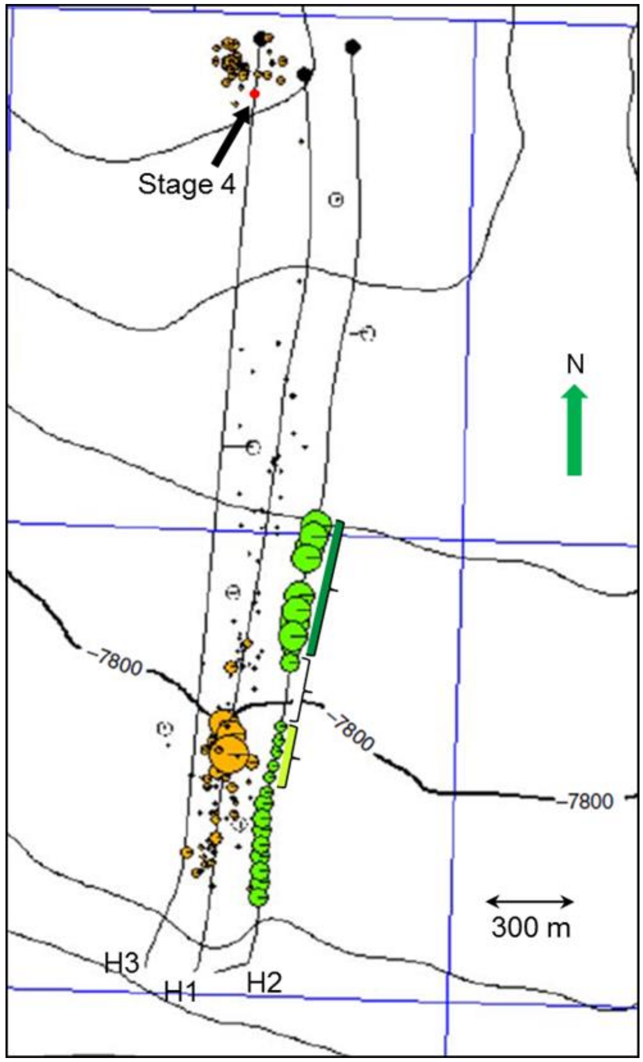


Figure 4.8: Map view showing the comparison between the microseismic-events amplitude and the relative production level of some stages of producer H2. All microsesimic events shown were triggered by the hydraulic fracturing of stage 4, located in the north end of the producer H3. The microseismic events are represented by the orange disks which have their sizes scaled according to the amplitude of the events. The relative production level of some stages of H2 is represented by the green disks and their sizes are scaled according to their production level. Note that the strongest microseismic events are close to the least productive stages measured by the Production-Logging tool (PLT). It is claimed that stronger events are more frequent in depleted areas where the differential stress is larger, promoting their occurrence. The positive anomaly observed in our tomography study is associated with the most prolific stages. The brackets follow the same color-code used in Figure 4.6 (modified from Dohmen et al., 2017).

the low production of the stages of H2 close to V1. Another region in the tomography result of V1 shows a higher P-velocity, compared to the initial model, halfway between the V1 and the V5 wells (Figure 4.5a - black dashed ellipse) which I interpreted as a pristine area, i.e. an area which was not fractured, at least not pervasively, during the completion of H1 and H3.

The difference between the tomographies (Figure 4.6) yields interesting features which can be compared to the PLT data. The stages with the largest production, pointed out in Figure 4.8 by the green bracket, coincide with the highest positive values of P-velocity change (red and yellow), also pointed out by the green bracket in Figure 4.6, indicating the reduction of the P-velocity after the hydraulic fracturing of these stages. Since the hydraulic fracturing process likely decreases the P-velocity values due to the increase of the fracture density, I am interpreting this P-velocity reduction as caused by the creation of fractures within the Upper and Middle Bakken members and the base of Lodgepole Formation. As the anomaly follows towards the south, it fades out, showing negative values (blue and purple), at the same stages that show smaller production according to the PLT data, marked by the white and light-green brackets in the figures 4.6 and 4.8. Unfortunately, the PLT data within the white bracket is not complete. The purple areas of the tomography difference, where there is low or no ray tracing coverage in at least one of the tomographies, are not considered for any interpretation since the difference analysis requires good raypath coverage for V1 and V5 tomography results (figures 4.7a and 4.7b). Therefore, in the difference result, only a central area between the observation wells can be considered valid for interpretation. It is also possible to see that this P-velocity positive anomaly extends vertically up to the same depth where most of the microseismic events associated with the reservoir fracturing are located (microseismic events located 75 to 100 m above the depth of the stimulation).

Not all microseismic events seem to be correlated to the stimulation of the reservoir. Some of them are clustered approximately 275 m above the reservoir depth. Indeed, they were triggered during the hydraulic fracturing of the stages 21, 22, and 23 of H2 and are interpreted as caused by the reactivation of natural fractures (Dohmen et al., 2014; Yang and Zoback, 2014). Interestingly, these out-of-zone events occur just above the region where the V1 minus V5 positive anomaly is interrupted, leaving the anomaly split in two (Figure 4.6). This interruption may indicate the effect of the natural fractures deviating the hydraulic fluids to upper formations which could lead to less effectiveness of the hydraulic fracturing process in this region. In this case, the tomographies data acquired before and after the hydraulic fracturing would show minimum differences between them, as we see in the area where the anomaly is interrupted.

Figures 4.9a, 4.9b, 4.9c, and 4.9d show the results of the Thomsen anisotropic parameters, ε and δ, (VTI model) obtained from the tomography study. They were calculated using the data acquired by the well V1 (Figures 4.9a and 4.9b) and by the well V5 (Figures 4.9c and 4.9d), respectively. Although it is possible to identify few lateral variations in the anisotropic parameters results, the overall behavior of ε and δ is laterally constant and horizontally layered with values indicating low anisotropy intensity. Examples of small lateral variations are the δ result close to the V1 well at the Bakken Formation (Figure 4.9b) and the ε result in the Lodgepole Formation nearby V5 well (Figure 4.9c).

Even though the resultant raypaths for the area may show a limited variation of their angle of propagation, the calculated values for the anisotropic parameters are compatible with the ε and δ results found by other authors for the Lodgepole and Mission

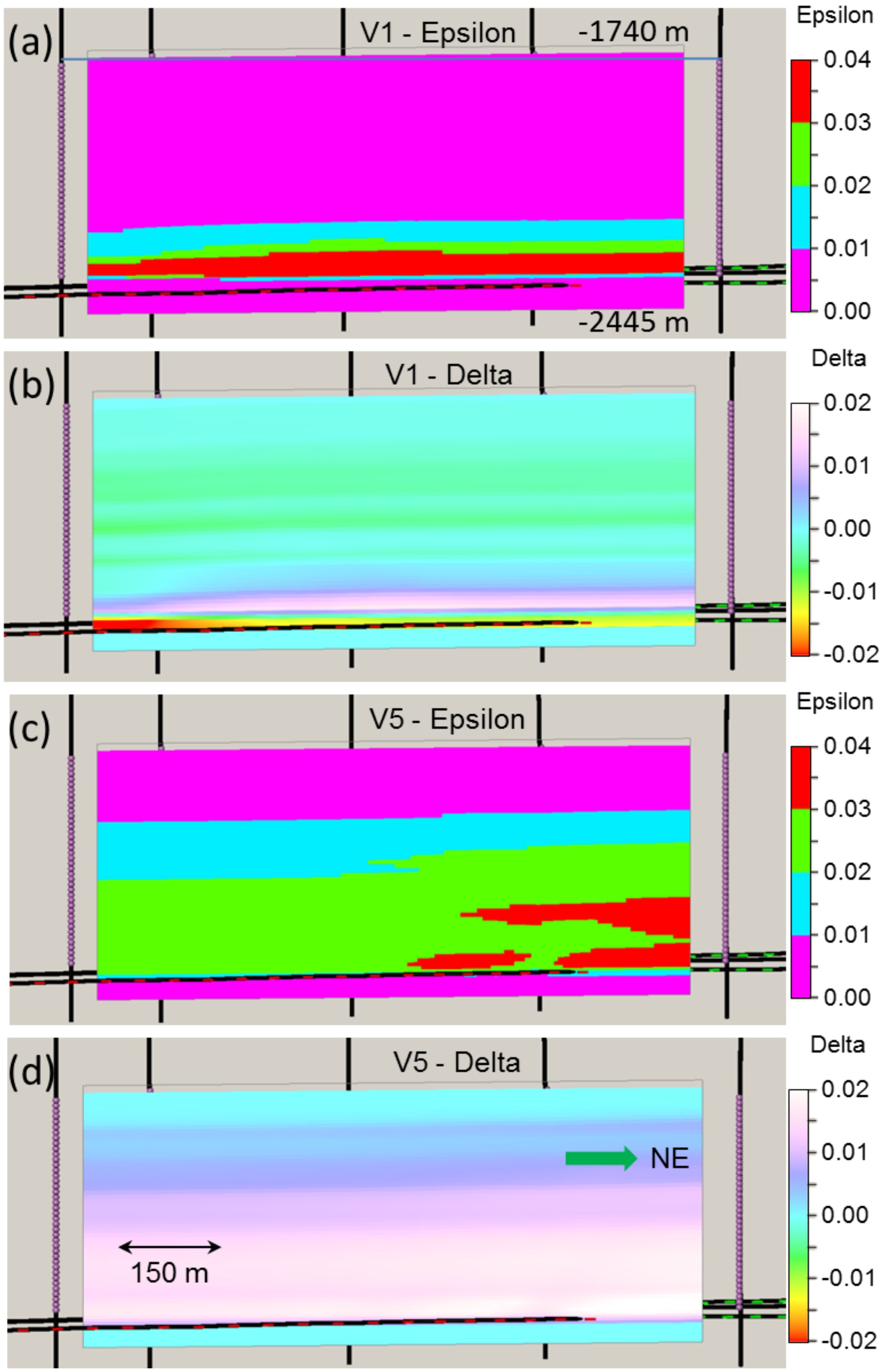


Figure 4.9: Epsilon and Delta anisotropic parameters derived from the anisotropic tomography of the data acquired by observers V1 (a and b) and V5 (c and d). Note the lower value of the parameters which is consistent with the anisotropic intensity calculated by other authors (Huang, 2016; Yuan and Li, 2017; Grechka et al., 2017) for the overburden formations. The depth is annotated in sub-sea true vertical depth.

Canyon formations (Havens, 2012; Li et al., 2014; Huang, 2016; Yuan and Li, 2017; Grechka et al., 2017). Nonetheless, the results found for the Upper Member of the Bakken Formation cannot be considered correct since laboratory measurements describe this black shale as highly anisotropic (Vernik and Liu, 1997; Havens, 2012; Li et al., 2014). This can be explained by the limit of resolution of the tomography method which cannot solve the anisotropic behavior of the Bakken Upper Member that has only 3 m of thickness in the area. Due to the geometry of acquisition and the thinness of this layer, horizontal or near horizontal raypaths that cross this member are not recorded. Moreover, the total traveltime of the vertical raypaths has little influence from this member, leading to a poor characterization of its anisotropy. Furthermore, the cell grid of 70 x 70 x 10 m of the tomography grid is quite large to solve the Upper Bakken Member.

The values of ε and δ obtained from the tomography studies and from the VSP walkaway analysis (Chapter 3, Figure 3.14) are similar, except for the δ values calculated with well V1 data. In this case, the δ value calculated using the tomography technique is lower than those achieved using the VSP walkaway procedure and they are more similar to the values found in other studies (Havens, 2012; Li et al., 2014; Huang, 2016; Yuan and Li, 2017; Grechka et al., 2017). This difference may be explained by the use of all available data in the case of the tomography study (only half of receivers of well V1 were used in the VSP walkaway processing; please, refer to Chapter 3). Moreover, the use of the vertical 3D interval P-velocity model as the initial for the tomography preserves the variation of the P-velocity in the vertical direction, improving the precision in the δ calculation. Despite the similarities between the Thomsen parameters obtained with different methods, the production data, apparently, is better explained by the P-velocity changes rather than the anisotropic parameters changes.

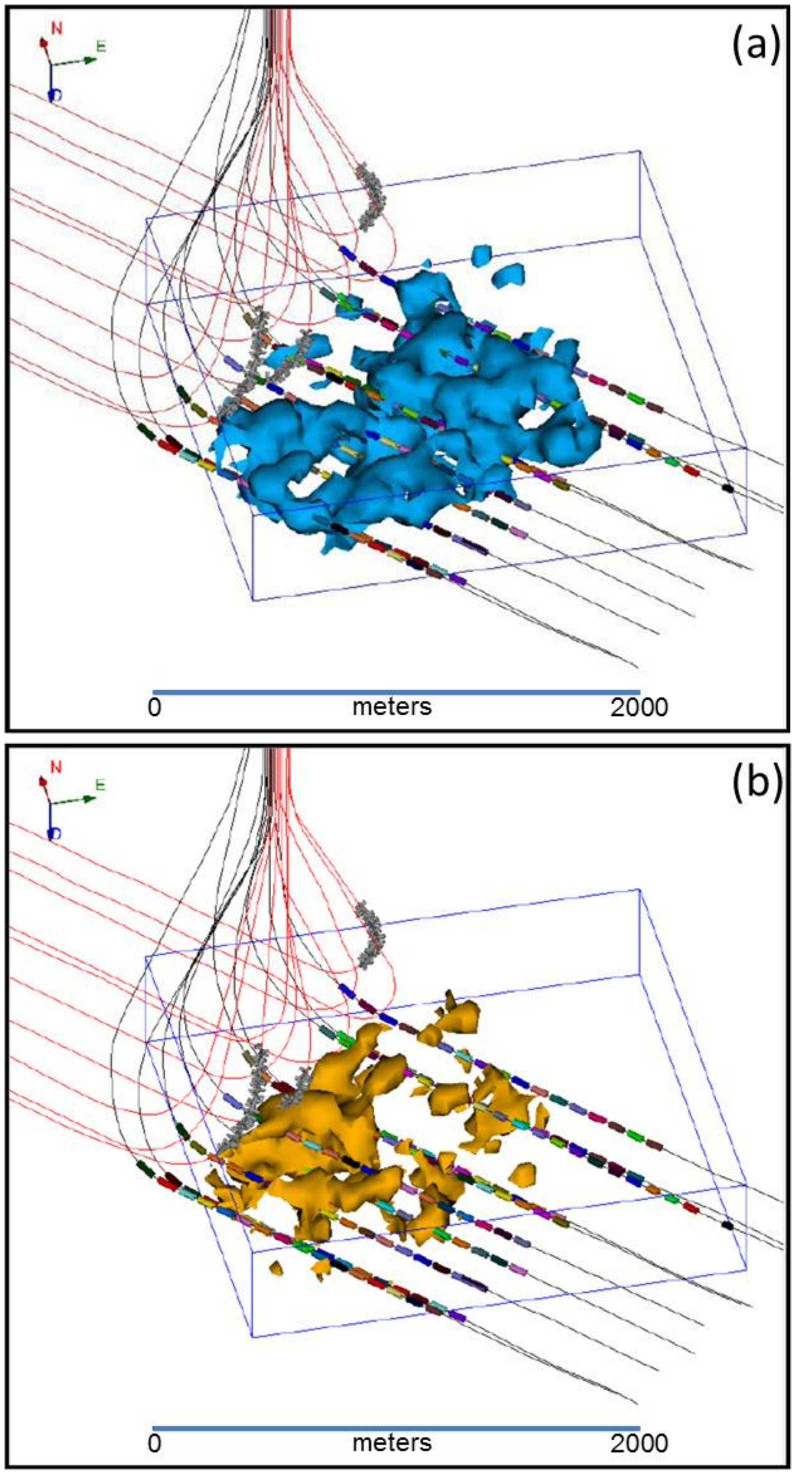


Figure 4.10: (a) Iso-surface showing the -100m/s decrease of P-velocity and (b) Iso-surface showing the 100m/s increase of P-velocity, both compared to the initial velocity model. The former is interpreted as result of the rock fracturing and the latter as result of the stress accumulation from the toe to the heel of the producers (modified from Crowley et al., 2015).

## 4.3 DISCUSSION

Our tomography results show good correlation between the P-velocity variation (before and after the hydraulic fracturing process) with the most prolific stages in the producer H2 (Figure 4.6). Two other studies are present below which help in the interpretation of my results.

Apparently, the correlation of the P-velocity changes with the production of the H2 shows that the larger the P-velocity change, the larger is the production. In that regard, Crowley et al. (2015) show a similar result (approximately 100 m/s of P-velocity reduction after the hydraulic fracturing) in a 4D tomography study which used different groups of microseismic events instead of perforation shots. Figure 4.10 summarizes their findings. These microseismic groups have passed through the same cells of the initial P-velocity 3D grid before and after the hydraulic fracturing stimulation. Note that decrease (blue iso-surface) and increase (brown iso-surface) in the P-velocity as result of their tomography study. They suggest that the decrease in the P-velocity was caused by the deformation and damage caused by the hydraulic stimulation of the formation. On the other hand, the increase in the velocity is suggested to be caused by the accumulated stress from toe to heel over the progression of the hydraulic fracturing towards the heel of the stimulated wells. This would justify the location close to the wells' heel of the majority of the cells with increased P-velocity values. Although they have not shown production data for comparison, the similarity of the P-velocity value reduction to my results may be indicative of the effectiveness of the tomography technique to differentiate produced and not produced volumes.

Another study from Crews (2015) correlates the presence of natural fractures with low hydrocarbon production which contradicts the general assumption that the presence of natural fractures benefits the oil production. He studied the production of 84 horizontal wells distributed over an area of 1900 $km^2$ which includes the area of the wells studied in my dissertation. He normalized the production of the wells by their production time and amount of proppant used in their completion. Cross-plotting the normalized production of the wells with the fractures extracted from seismic-derived products, he calculated a statistical valid relationship correlating low production of some wells with the presence of natural fractures (Figure 4.11).The natural fractures were considered as a second-order control factor of the production while the Bakken Formation thickness was interpreted as a first-order factor. He suggested that this could be caused by the breakage of the seal of the Bakken Reservoir leading to the pore pressure dissipation of the over-pressured Bakken Formation. The lack of the abnormal pore pressure in the Bakken Formation, which is an important driver of the production, would cause the lower production seen in some of the studied wells.

Although the study carried out by Crews (2015) is focused on large-scale structures, showing the influence of the natural fractures in the production of a widespread and relatively large number of wells, his results may bear some association with my findings. Figure 4.6 shows the difference between the results of the tomographies, performed before and after the hydraulic fracturing of some H2 stages. The interruption of the positive anomaly, associated to the most productive stages, happens at same stages linked to the triggering of microseismic events interpreted as the result of natural fractures reactivation (Dohmen et al., 2014; Yang and Zoback, 2014). I interpreted this interruption as a part of the H2 horizontal section less effectively fractured by the hydraulic fracturing process since the change in the P-velocity is close to zero. Moreover, the occurrence of microseismic events 275 m above the hydraulic fracturing average depth is indicative that the stress variation imposed by the hydraulic fracturing jobs at these stages was conducted to upper levels, possibly with the natural fractures working as conducts, leading the hydraulic fluids to shallower depths. If this interpretation is correct, areas associated with natural fractures may have lower production levels not only due to the low reservoir pore pressure caused by the lack of good reservoir seal, as stated by Crews (2015), but also due to the limited effectiveness of the hydraulic fracturing process in stages where natural fractures are present. A more conclusive interpretation would be possible if production data were available for the stages located where the natural fractures were interpreted.

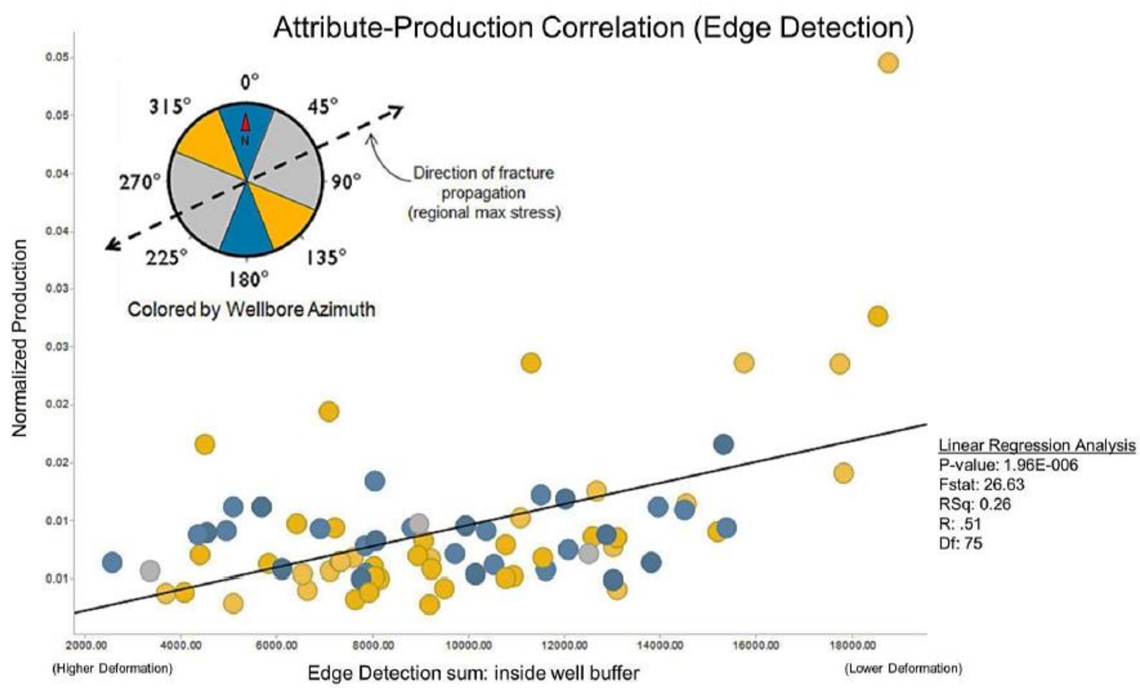


Figure 4.11: Cross-plot of normalized production of 84 wells and Edge Detection sum, a measure of seismic discontinuity of the area, showing a positive linear relationship between more productive wells and more seismic continuous regions. Areas identified as less continuous are interpreted as naturally fractured. The wells are colored by wellbore azimuth since such parameter is important to the propagation of the fractures hydraulically stimulated. Wells are preferentially oriented perpendicular to the maximum horizontal stress direction, allowing for fractures propagate parallel to that component of the stress field (modified from Crews, 2015).

One aspect inherent to the acquisition of the seismic waves originated from the perforation shots, which may be claimed to justify why this data was able to map such effect, is the proximity between source and receivers. High-frequency data benefits from this geometry of acquisition. Moreover, the raypaths observed in the tomography show that the area nearby the producer H2 is extensively sampled, at least where the P-velocity anomaly is clear, in both directions, i.e., towards the north (V5) and the south (V1). These raypaths are not only vertical or near vertical, as it would be expected in a seismic acquisition with the sources on the surface. Instead, they are more horizontal and they can travel, proportionally, throughout a larger volume of rock affected by the fracturing process compared to the vertical raypaths, especially if the created fractures are vertical.

However, one main aspect that has to be considered, which is not directly related to the acquisition geometry, is how the slow diffusivity of pressure within the fractures created by the hydraulic fracturing helps to keep them open in the first few hours after the breaking. It is important to bear in mind that the stages, in the tomography study, may have been fractured only 1 to 2 h early. It is likely that the pressure within the walls of the recently created fractures, and possibly the proppant, helps to keep the fractures width larger than in any other time in the future, lowering the P-velocity. Indeed, our result points out to a reduction of the P-velocity, after the hydraulic fracturing, in the stages associated with the larger oil production.

## 4.4 CONCLUSIONS

The statements below summarize the findings of this chapter:

- I was able to identify areas near the horizontal section of well H2 with a consistent decrease of the P-velocity after the well had been hydraulically stimulated. This decrease in the P-velocity was interpreted as the result of the propagation of fractures created during the hydraulic stimulation. The comparison between the P-velocity anomaly and the production of different stages of well H2 shows that the most productive stages are associated with areas where the P-velocity suffered the largest reduction. For that purpose, I used the direct P-wave arrivals emitted by the perforation shots and the VSP 3D grid-based anisotropic tomography algorithm available in the Paradigm Software Suite.

- This lowered P-velocity anomaly is interrupted in the stages associated with natural fractures which were reactivated during the hydraulic stimulation. At these stages, the P-anomaly is approximately equal to zero indicating that the P-velocity has not changed much after the stimulation. I interpreted that as the result of the limited effectiveness of the hydraulic fracturing process in these stages, where the hydraulic fluids were conducted to upper levels triggering microseismic events at 275 m above the Bakken Formation and not contributing to the stimulation of the reservoir.
- The results of the separated tomography studies using data acquired by wells V1 and V5, before and after the hydraulic fracturing, respectively, show interesting features. An area possibly not fractured by the stimulation of well H1, carried out 2.5 years before the well H2 had been drilled, shows slightly higher P-velocity values compared to the initial model (Figure 4.5a). Also, an area, nearby the well V1, characterized by low P-velocity value (Figure 4.5a), is associated with a lower level of hydrocarbons production and microseismic events of higher magnitude. I interpreted the low P-velocity signature of this area as the result of a more pervasive and efficient hydraulic stimulation when H1 was hydraulically stimulated, an interpretation which is corroborated by the lower H2 production level in this region and the larger magnitude of microseismic events closer to H2.

# Chapter 5

## High-resolution P-wave imaging using perforation shots as seismic sources

This chapter focuses on the use of the P-wavefield emitted by perforation shots in imaging the near section of the Bakken Formation. I used the horizontal section of well H2 as a proxy for a shot seismic line and P-wave reflections were recorded by geophone arrays placed within vertical wells, wells V1 and V5, located at both ends of this line. This geometry, similar to the typical VSP walkaway geometry, allowed for imaging of more than 600 m of the overburden above the Bakken Formation, including parts of the Lodgepole, Mission Canyon, and Charles formations, and around 1200 m of the horizontal section between the vertical wells. High-frequency images with a dominant frequency of around 300 Hz were created, revealing the usefulness of the wavefields created by the perforation shots for imaging economically interesting thin layers within the overburden or fractures and faults. These features are below the seismic resolution of seismic surveys with sources on the surface.

The steps of the VSP walkaway workflow processing are shown and discussed. The final images are compared to the 3D surface seismic data and to the seismic synthetic traces derived from the well log P-impedances data available in the area.

## 5.1 INTRODUCTION

After characterization of the area with the tomography study using the direct arrival P-waves, which aimed at the identification of the velocity variations that could be correlated with the production data, I focused on the use of the perforation shots to image the overburden region. In addition to the clear direct arrivals, P-wave reflections from the overburden were also identified and, initially, they were used to image natural faults or fractures in the overburden since clusters of microseismic events have been linked to the existence of natural fractures in the area (Dohmen et al., 2014; Yang and Zoback, 2014).

Although the images built using the reflections produced by the perforations shots were not conclusive with regard to fracture identification, reflectors more than 600 m above the reservoir depth were imaged with high-frequency content, around 300 Hz dominant frequency, identifying thin layers in the overburden.

The first step to use the perforation shots as seismic sources to image the layers above the horizontal wells was to define which perforation shots to use and what receivers were best located to keep the acquisition geometry simple and still record the reflections. In this study, I focused the seismic processing on imaging the reflectors in the overburden since all receivers were placed above the horizontal wells. Reflections from layers below the horizontal wells were also recorded but they were removed from the data in the seismic processing since they were weaker than the reflectors in the overburden. If the receivers were below the shot line, the reflections from the underburden would be possibly stronger allowing their use.

Given the data and resources available, the data chosen for the overburden imaging were the same used in the tomography study (Figure 3.13). Using these data, a reverse walkaway VSP processing workflow was considered the most appropriated to the overburden imaging and two images were produced: one using the data acquired by the well V1 and other with the data acquired by V5. As described in the tomography study, 53 perforation shots were used to image the overburden nearby the observer V5 and 50 perforation shots were used in the V1 seismic image processing. Also, approximately 40% of the shots acquired by V1 were recorded by only 20 receivers, instead of 40, due to operational issues.

## 5.2 VSP WALKAWAY PROCESSING

The reverse walkaway VSP processing workflow is shown in Figure 5.1. The first step in the workflow is the inclusion of the geometry data in the trace headers. This information includes depths and spatial coordinates of the perforation shots and receivers. Based on that, other parameters can be calculated as the shot-receiver azimuth and offset. Until the upper and lower mute application, all VSP walkaway processing steps were performed in the RokDoc software from Ikon Science. From the Spherical Divergence correction up to the end of the workflow, all steps were done in the VISTA seismic processing software from Schlumberger.

Next, the rotation of the three components was performed to separate the different phases (P, SH, and SV-waves, both up and downgoing) of the wavefield. For that purpose, an initial picking of the P-wave direct arrival was done so that a window including the wavelet of the direct arrival of this phase could be established. After that, a

3 ms window, starting from each trace pick, was defined in the raw vertical channel which, in general, has shown the P-wave direct arrival clearer. That window was used to rotate the horizontal channels, H1 and H2, yielding the radial and transverse components. The radial component tends to concentrate the P- and SV-waves which propagate within the source-receiver plane. Then, the second rotation was performed using the raw vertical and the radial channels to separate upgoing P-wave in the Pmax component and downgoing P-wavefield (and some upgoing SV-wavefield) in the Pmin component. After most of the downgoing P-wave has been isolated in the Pmin, the picking of the P-wave direct arrival was revised and verified if all traces have been picked on their onset (Figure 3.5).

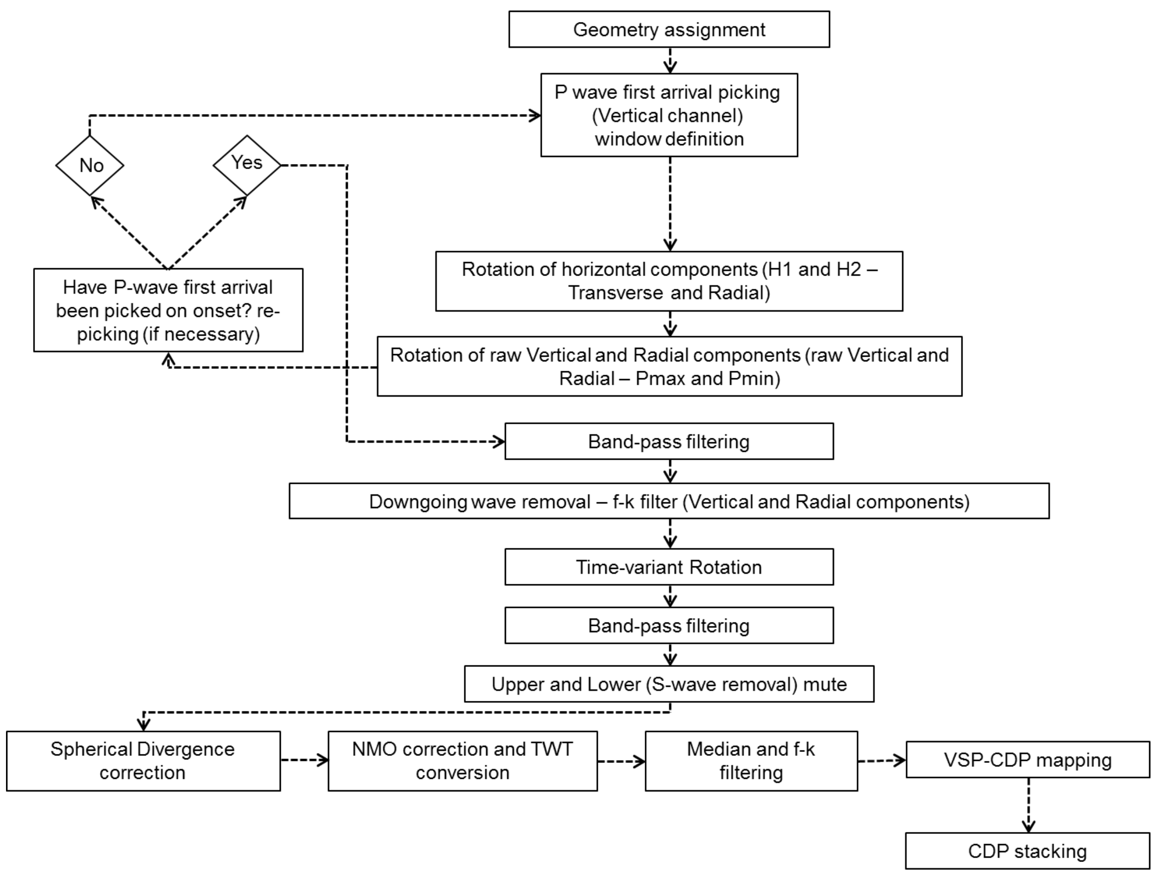


Figure 5.1: VSP walkaway processing workflow used in the 2D seismic image calculation. The perforation shots of producer H2 were used as the seismic source in this processing sequence.

Since the sources and the receivers are close to each other, a good signal-to-noise ratio for the P-wave reflections was observed showing broad bandwidth and high-frequency content. Nonetheless, some lower frequency noise, in this case around 65-85 Hz, was recorded and the P-wave reflections were not so visible above the frequency of 500 Hz. Therefore, a band-pass filter (65 – 85 – 480 – 500 Hz) was applied to the data to enhance the reflections (Figure 5.2).

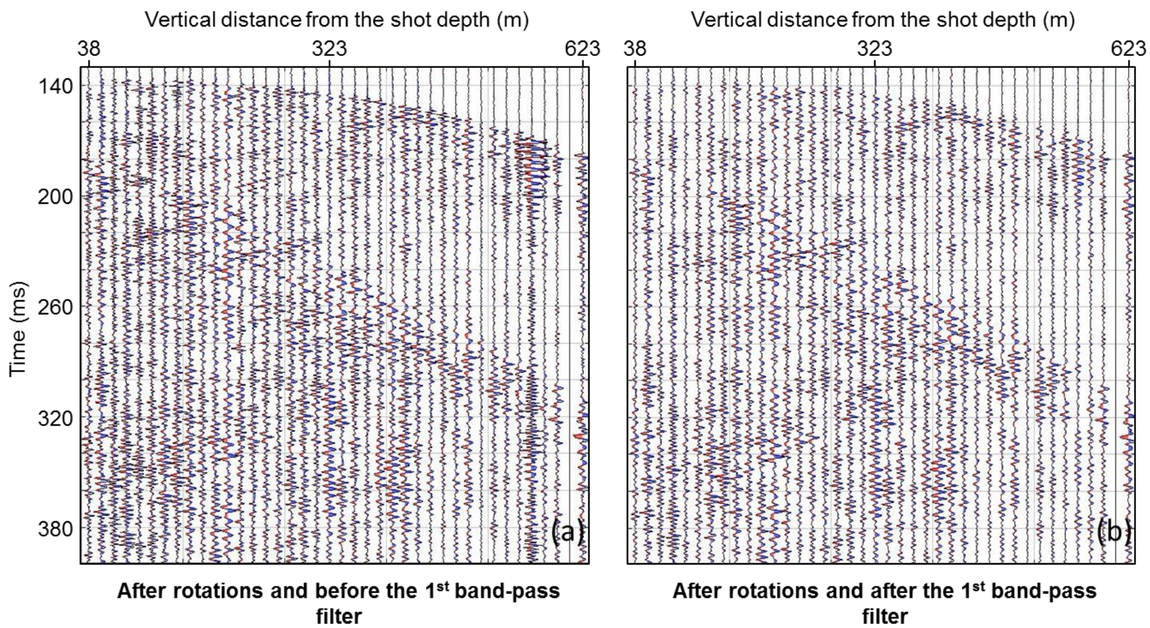


Figure 5.2: Perforation shot gather located at stage 25 of producer H2 and recorded by observation well V5 (792 m offset) with a) showing the data after the rotations of the direct arrivals (horizontal and vertical components) and b) after the application of the first band-pass filter. The data are shown in the shot domain. Automatic Gain Control (AGC) was applied to make the reflections more visible.

In the following step, the remaining energy from the downgoing P-wave was removed from the raw vertical and radial components using the f-k filter after the P-wave direct arrival picks have been flat to a user-defined time datum in the shot gather domain. The f-k rejection area was defined in the f-k domain, removing the energy aligned in the vertical direction which enhanced the P-wave reflections of the perforation shots. The Time Variation Rotation angles were calculated to separate the upgoing P-wave from the upgoing SV-wave. In the resultant upgoing P-wave, a second band-pass filter with the same parametrization of the first band-pass filter was applied to remove any possible spectral frequency changes during the downgoing P-wave removal.

An upper muting was carried out using the P-wave direct arrival picks to clean the data from any artifact or event before this time and a lower muting was also performed to avoid the introduction of the S-wave direct arrival and converted waves that could interfere in the P-wave reflection stacking process (Figure 5.3).

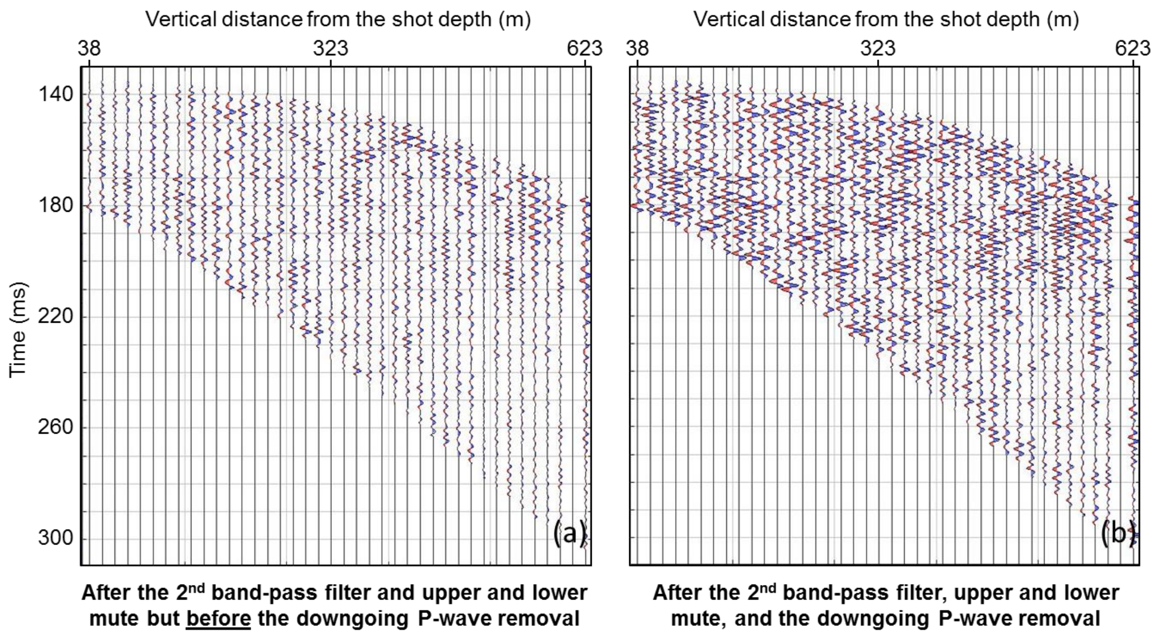


Figure 5.3: Perforation shot gather located at stage 25 of producer H2 and recorded by observation well V5 (792 m offset) with a) showing the data after application of the upper and lower mutes and b) after the downgoing P-wave removal. The data are shown in the shot domain. AGC was applied to make the reflections more visible.

With the objective of comparing the possible P-wave reflections that could be retrieved from the perforation shots in the area of study, I performed an anisotropic elastic seismic modeling and compared it with the perforation shot P-wave data. The seismic modeling geometry reproduced the same VSP walkaway geometry found in the field and the comparison was done in the shot domain. The P-velocity cube used in the modeling was the same used in the tomography study (Figure 4.2a) and the S-velocity and density data were derived following the same methodology used for the P-velocity

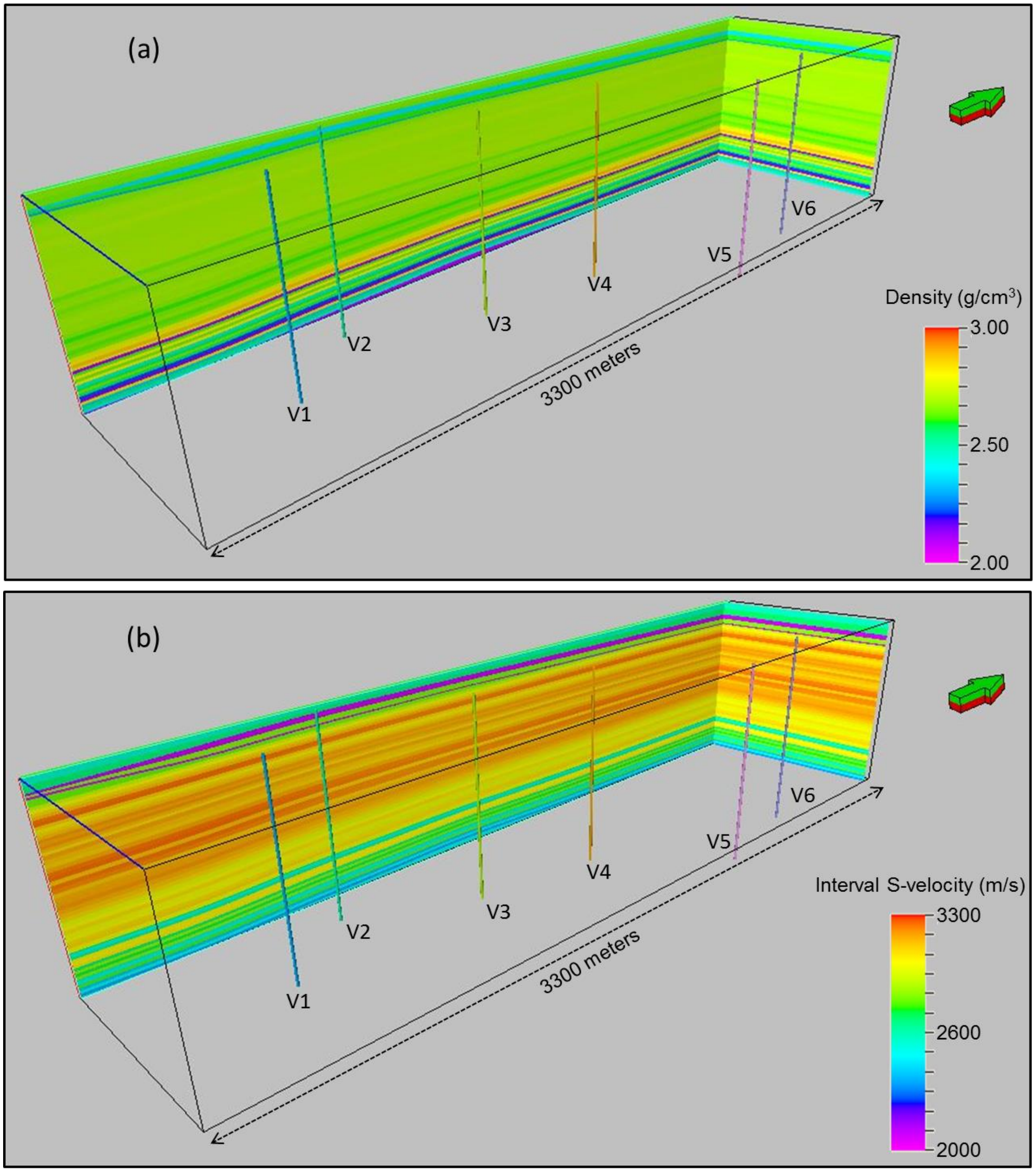


Figure 5.4: Density (a) and interval S-velocity cubes (b) used in the anisotropic seismic modeling study of a perforation shot triggered in stage 25 of the well H2 (Figure 5.5b). The cubes were calculated using the same technique used in the interval P-velocity calculation, i.e., the exponential isotropic kriging interpolation of the well logs data described in Chapter 4.

cube calculation (exponential isotropic kriging interpolation) described before (Figure 5.4). The ε and δ Thomsen parameters values were defined as 0.1 and 0.05 throughout all layers in order to impose a slight anisotropy behavior to the area (Havens, 2012; Li et al., 2014; Huang, 2016; Yuan and Li, 2017; Grechka et al., 2017); even though the Upper Bakken member is considerably more anisotropic, but with a small thickness. For an adequate comparison between modeled and field data, a Ricker wavelet parameterized with 220 Hz was used in the modeling as the field data show high-frequency content.

Figure 5.5 shows the comparison between the field data (Figure 5.5a), after the lower and upper muting have been applied, acquired with 792 m of source-receiver offset with the P-wavefield modeled data (Figure 5.5b) recorded by a vertical array of receivers with 800 m of offset from the source location. This perforation shot was located

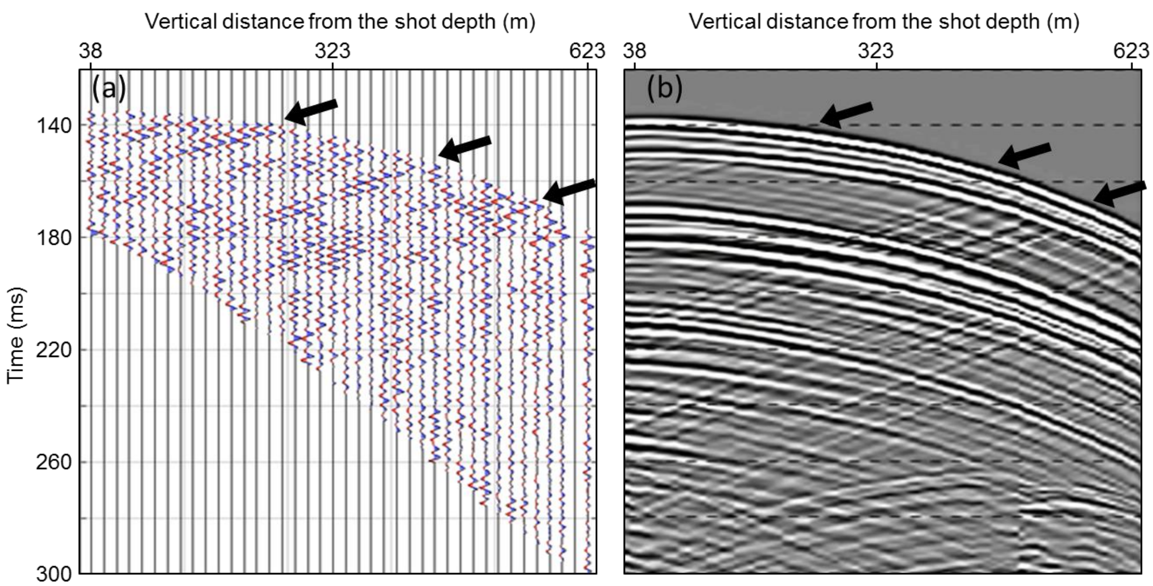


Figure 5.5: a) Perforation shot gather located at stage 25 of producer H2 and recorded by observer V5 (792 m of offset) processed until the upper and lower mute step (AGC not applied) and b) anisotropic seismic modeling result for a shot with approximately the same acquisition geometry of Figure 5.5a (800 m of offset) showing only the P-wavefield (downgoing P-wave was not removed). Note the reflection pointed out by the black arrows with the same velocity and at a similar depth. The elastic model used in the modeling is the same used as the initial model for the tomography study.

in stage 25 of well H2 and was recorded by well V5. There are visible P-wave reflectors (pointed out by black arrows) in the modeled data approximately coincident in depth to the field data. This result gave me the confidence that the P-wave reflectors observed in the field data can be retrieved and used to image the layers above the horizontal well.

The final part of the processing sequence included the correction of the spherical divergence using an exponential function gain and the normal moveout (NMO) correction using the vertical P-velocity profile acquired from the zero-offset VSP accomplished in the well V3. Next, the data was converted to two-way time (TWT) and f-k, band-pass filters (50 – 60 – 380 – 420 Hz), and median filter (window size with 6 traces and 1 sample) were used to enhance the P-wave reflectors. Figures 5.6 and 5.7 show 15 perforation shots, one per stage of well H2, recorded by the well V5, after the NMO and TWT conversion and the application of the filters mentioned. Finally, given the small lateral P-velocity variation and the simple structural framework of the area (horizontal layers), I decided to use the VSP-CDP mapping technique in order to create the CDP gathers of two seismic sections nearby the wells V1 and V5 which could be stacked and compared to 3D surface seismic acquired in the area. The binning interval used in the VSP-CDP mapping was 10 m. Figure 5.8 shows the result of the VSP-CDP mapping for the CDP number 29 located 280 m away from the well V5. Attempts of deconvolution were tried with different methods (predictive, spiking and P-wave direct arrival VSP deconvolution) and all have shown an increase in the energy in the lower part of the frequency spectrum (less than 100 Hz) which is clearly contaminated by energy not related to the reflection. Because the deconvolution mainly increased the energy in the lower part of the frequency spectrum, with almost no gain in the region of the spectrum where the P-wave reflections energy is present, I excluded the deconvolution of the workflow processing.

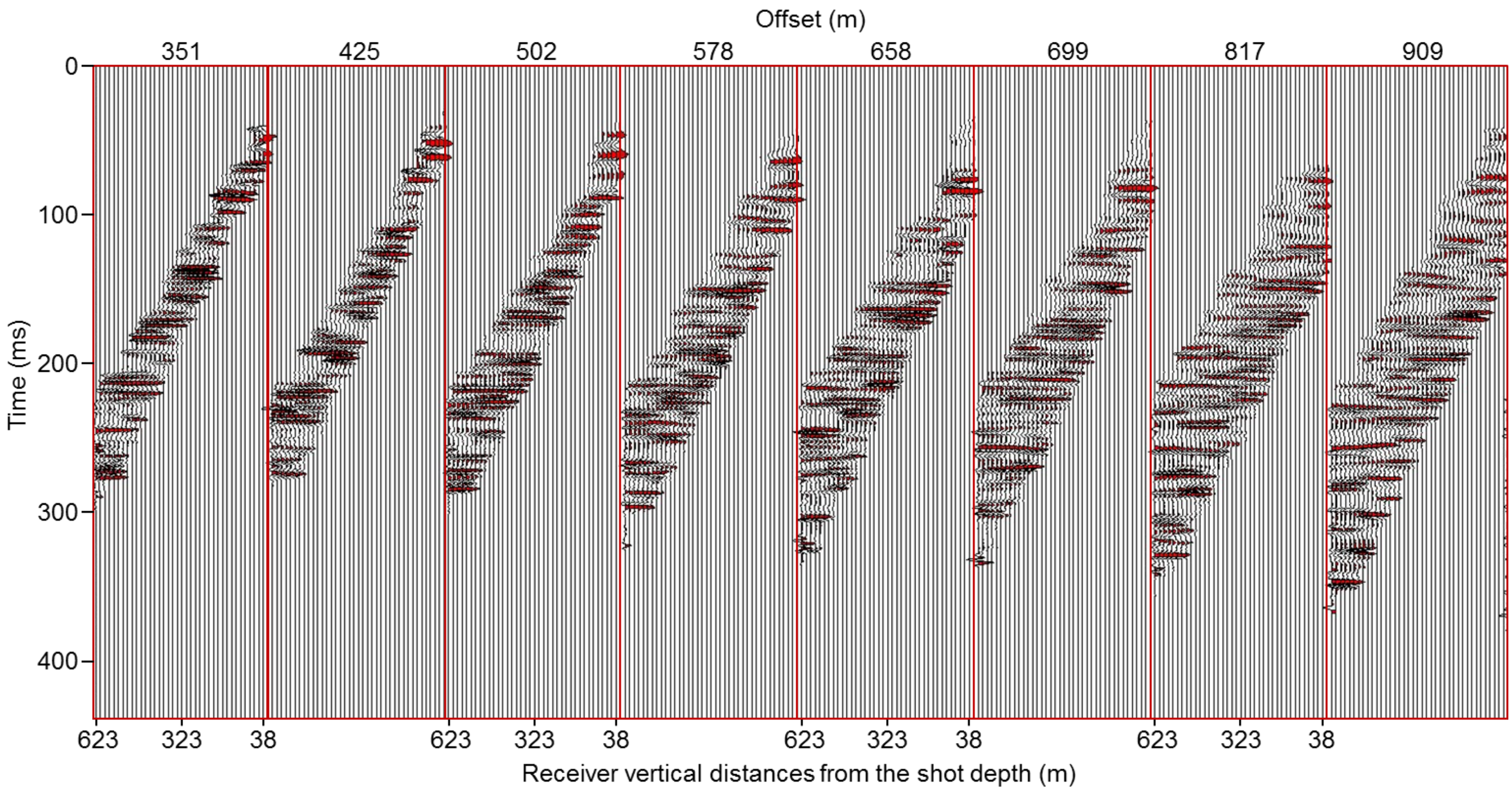


Figure 5.6: Examples of perforation shots gather triggered in stages of well H2 (one shot per stage, from stage 19 to 26) and recorded by well V5 after the application of Spherical Divergence Correction, NMO Correction, TWT conversion, and band-pass, Median, and f-k filters. Note the horizontal reflectors which are the expected direction for them in the case of layers arranged predominantly horizontal. The offset values describe the horizontal distance between the vertical receiver array in well V5 and the perforation shot position. The AGC was applied to make the reflections more visible.

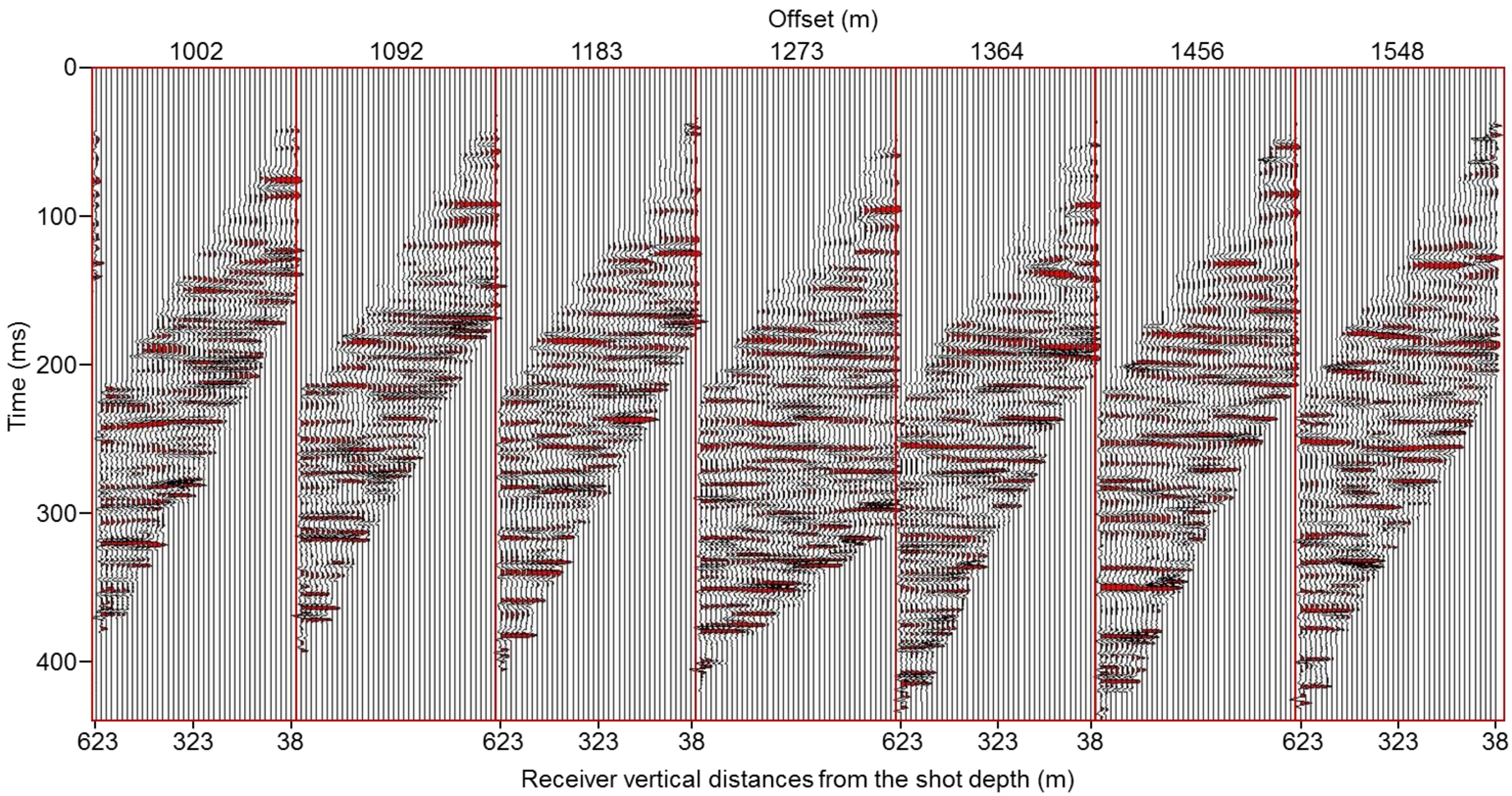


Figure 5.7: Examples of perforation shots gather triggered in stages of well H2 (one shot per stage, from stage 27 to 33) and recorded by well V5 after the application of Spherical Divergence Correction, NMO Correction, TWT conversion, and band-pass, Median, and FK filters. Note the horizontal reflectors which are the expected direction for them in the case of layers arranged predominantly horizontal. The offset values describe the horizontal distance between the vertical receiver array in well V5 and the perforation shot position. The AGC was applied to make the reflections more visible.

With the two seismic sections obtained from the perforation shots after the VSP-CDP mapping, the comparison of these images with the 3D surface seismic acquired in the area was carried out via well log synthetics. Using the P-sonic and density logs of the wells V1 and V5, seismic synthetic traces were calculated and compared with the reverse walkaway VSP and with the 3D surface seismic in order to quantify the gain in resolution derived from the use of the perforation shots as seismic sources. The wavelet used in the synthetic calculation for comparison with the surface seismic was statistically extracted from the well V3 since it had longer well logs which were necessary to extract the wavelet with the characteristic lower frequency content present in the surface seismic. Similarly, the wavelets used in the synthetic calculations compared to the reverse walkaway VSP seismic data were statistically extracted from their perforation shots image.

First, Figure 5.9 shows the comparison of the two seismic sections obtained from the perforation shots comparing them to a seismic line extracted from the 3D surface seismic. The P-impedances of both V1 and V5 wells are shown for reference. It is evident the larger high-frequency content of the perforation shots images compared to the surface seismic data. Figures 5.10a, 5.10b, 5.11a, and 5.11b show a zoom view of the synthetic seismic traces calculated with the P-impedance well logs of the wells V1 and V5. These figures show the synthetics calculated using the surface data and the reverse walkaway VSP images, for both V1 and V5 wells, side by side so that they can be easily compared to each other.

The comparisons between the high-resolution perforation shots images with their correspondent surface seismic images show how thin layers are better resolved. Observing the synthetics, one can see that the reflections become more evident at 150 m above the reservoir depth and go up to, at least, 550 m above that level with a good

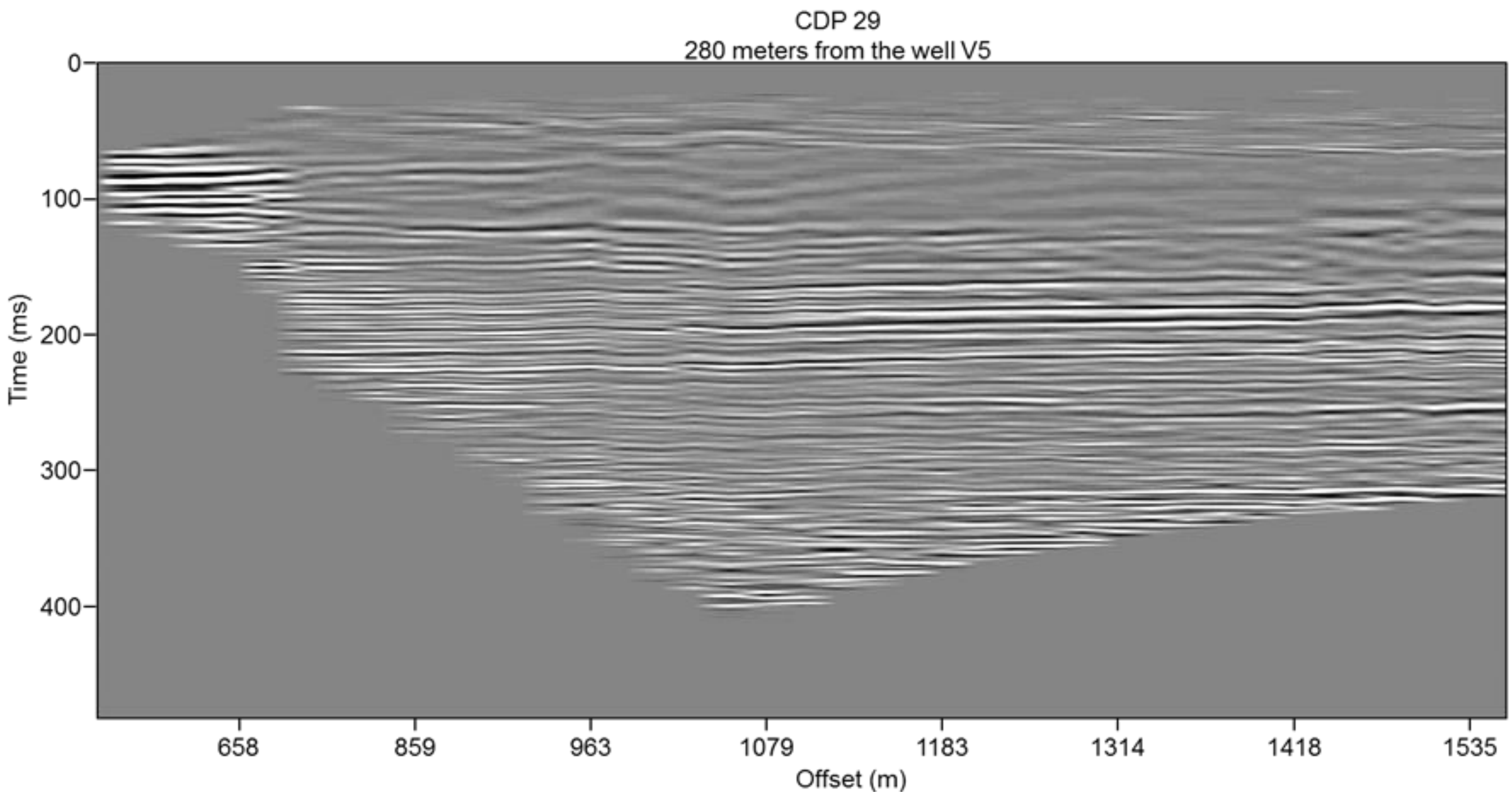


Figure 5.8: Common depth point gather (CDP) number 29 obtained from the perforation shot data acquired by well V5 after the application of the VSP-CDP transformation. This CDP is located 280 m away from the well V5. Ideally, the seismic layers observed in the CDP should be as flat as possible.

correlation with the synthetics. Reflections beyond 550 m are visible in Figure 5.9 but no logs were available to the synthetic calculations at these depths.

Regarding the synthetic of the well V1, the density log used in its calculation had to be estimated since the original density was not reliable. Hence, the density log was calculated using a neural network approach using the P-sonic, S-sonic, and the gamma-ray logs of the other five observers available in the area as the training data. Also, it is important to remember that the well V1 recorded just half of the receivers for 40% of the perforation shots, as mentioned before, reducing the data fold of its seismic section. Because of these reasons, I consider the result obtained by the well V5 more reliable. Another point was the limitation of the recorded reflections in the reverse walkaway VSP data given the maximum source-receiver offset that was able to produce reflections with signal-to-noise high enough to be processed. This limitation led to the coverage lack between the two VSP seismic images.

It is worthy of note the differences between the polarity and the frequency spectrum of the wavelets extracted with the perforation shots and the surface seismic data. For instance, the well V5 shows the wavelet extracted from perforation shot image (Figure 5.11b) with the polarity inverted (roughly 180º) when compared to the wavelet used in the calculation of the synthetic using the surface seismic data (Figure 5.11a). This is explained by the acquisition geometry of the perforation shot data (shot line deeper than the geophone array) which leads the P-wave reflections to be recorded as the downward part of the P-wavefield. This geometry is inverted compared to the surface seismic geometry. In regard to the wavelet frequency spectrum, the frequency peak of the perforation shots image (Figure 5.11b) lies between approximately 100 Hz to 300 Hz and the frequency peak in the case of surface seismic goes roughly from 10 Hz to 60 Hz (Figure 5.11a). The higher frequency content may be explained by the proximity

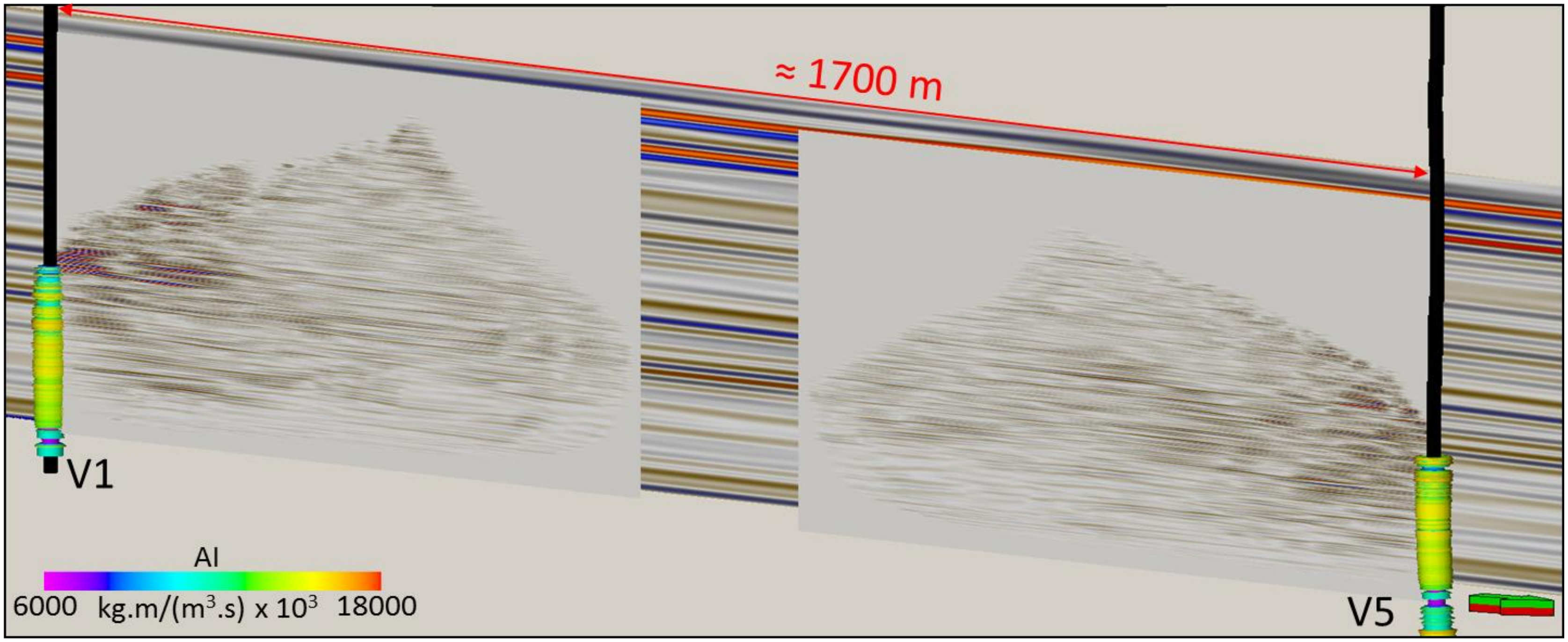


Figure 5.9: Section view of the two 2D seismic images obtained from the data acquired by observers V1 and V5 overlaying a seismic inline of the 3D seismic cube acquired in the area. Note the difference in the frequency content when the perforation shot sections are compared to an inline from the 3D seismic cube. The acoustic impedances of the observers V1 and V5 are shown for comparison.

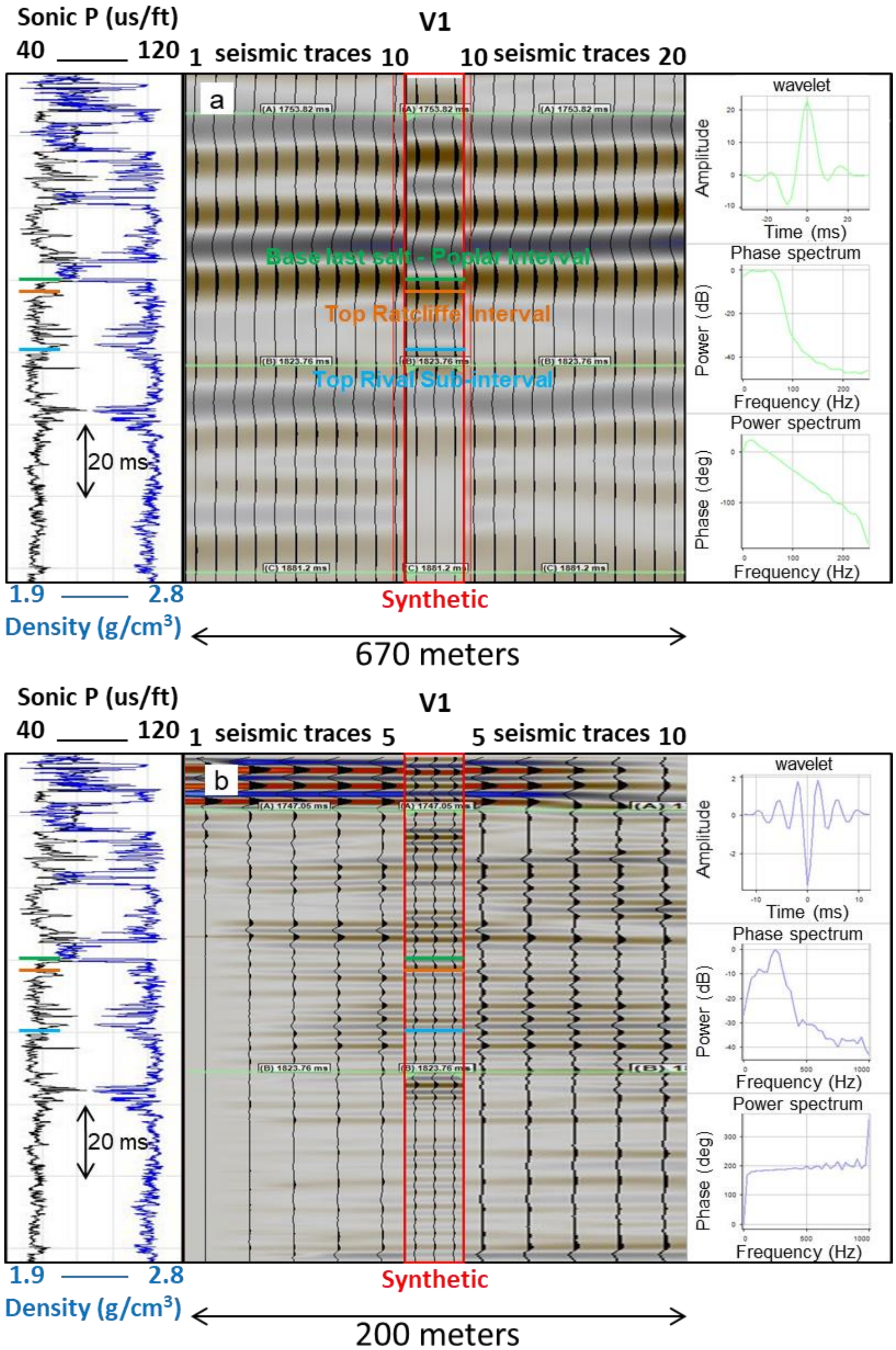


Figure 5.10: Synthetic seismic traces calculated from the reflectivity well log of well V1. a) shows the synthetics calculated using the wavelet extracted from the closest seismic inline to the well V3 acquired on surface and b) shows the same synthetic using the wavelet extracted from the 2D seismic line obtained from the perforation shots acquired by well V1. Note the difference in the frequency content and the shapes of the wavelets between the synthetics from the perforation shot and surface seismic. Geologic markers are overlaid on the synthetics and well logs to help in the interpretation of the images.

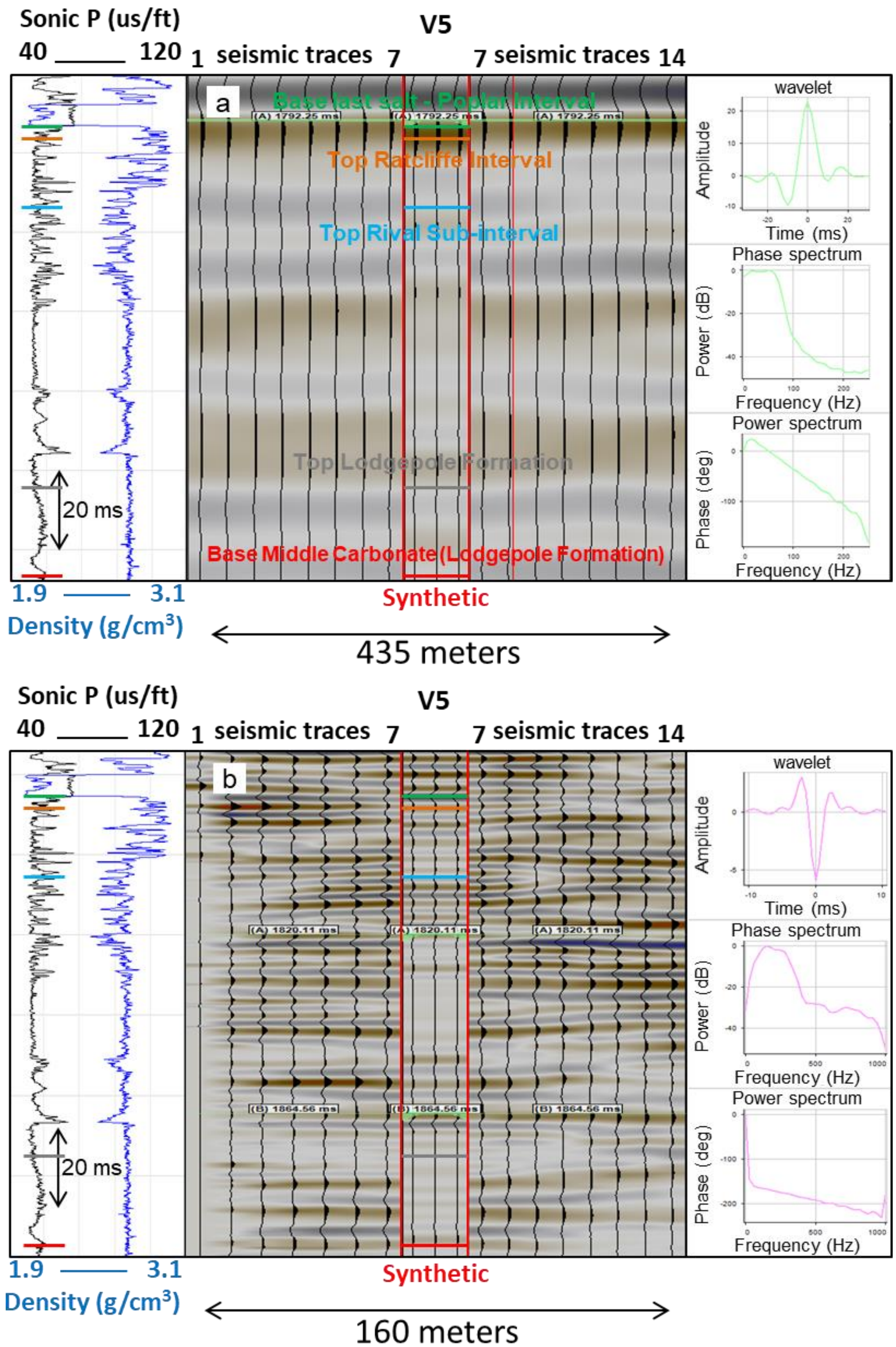


Figure 5.11: Synthetic seismic traces calculated from the reflectivity well log of well V5. a) shows the synthetics calculated using the wavelet extracted from the closest seismic inline to the well V3 acquired on surface and b) shows the same synthetic using the wavelet extracted from the 2D seismic line obtained from the perforation shots acquired by well V5. Note the difference in the frequency content and the shapes of the wavelets between the synthetics from the perforation shot and surface seismic. Geologic markers are overlaid on the synthetics and well logs to help in the interpretation of the images.

between source and receivers in the case of perforation shots images, as mentioned early. It is also necessary to consider that some other effects as near-surface-low-velocity zones and source and receiver ground coupling, which can cause issues in the surface seismic acquisition, may be less problematic when sources and receivers are placed in the subsurface.

To include an interpretative character to the obtained images and evaluates the gain associated to the use of high-frequency seismic data in the interpretation, the synthetics and well logs of figures 5.10 and 5.11 are overlaid with the interpreted geologic markers. Apparently, the high-frequency images are able to retrieve some reflectors associated with the markers' depths which are not visible when compared to the surface seismic. Also, reflectors associated with thin layers not highlighted by any marker are visible. Nonetheless, some reflectors show some lateral discontinuity. Such discontinuity may represent the lateral geologic variation of the layers or the limitation of the seismic processing sequence to retrieve the reflected P-wavefield emitted by the perforation shots. A more extensive interpretation work is necessary to validate the usefulness of the perforation shot images.

## 5.3 DISCUSSION

After the analysis of the reverse walkaway VSP images, fractures and faults have not been identified, despite the high-frequency content of the overburden images obtained from the perforation shots. A possible explanation for that may reside in the fact that the fractures and faults have a small throw, making difficult their identification even using high-frequency seismic images (K. Katahara, personal communication, 2016). Nonetheless, reflectors from thin layers have been imaged. A visual comparison between the images from the perforation shots and from the surface seismic shows the gain that was obtained in terms of resolution with the former data.

With regard to the use of unusual seismic sources to imaging purposes, it is particularly noteworthy the study carried out by Grechka et al. (2017a) which uses the same data set that I used in this dissertation for imaging. They used microseismic events triggered at stage 21 of the well H2 to image the four perforation shots holes of stage 19 of the same producer (Figure 5.12). The microseismic events used in this study were located around 275 m above the horizontal section´s depth of H2, allowing their use for imaging the stage 19 with the reflected and scattered waves from the reservoir level recorded by the geophone array located at the well V5. In spite of the necessity of more studies related to the use of unusual seismic sources for imaging, the high-resolution images achieved in this thesis and the results obtained by other authors demonstrate that this technique is feasible. The routinely use of microseismic events and perforation shots with that purpose is important in the dissemination of their use for imaging and for the improvement of the images' quality generated with them.

An objective which may foster the use of the perforation shots as a seismic source and open a new possibility in the seismic imaging is the acquisition of high-resolution images of other formations with economic interest at different depths. Probably, the most obvious basin which could benefit from these high-frequency images is the Permian Basin which has its high activity level linked to the possibility of the operators develop more than one target at the same acreage. Maybe the most visible aspect of the high activity level is the significant rise in the bidding price observed in the Permian Basin in the 2016-2017 period (Drillinginfo, 2017). Figure 5.13 shows the Wolfcamp Shale stratigraphy column in the Midland Basin, one of the three basins that form the whole Permian Basin system. Six targets are possible in the Midland Basin

Wolfcamp, namely, Wolfcamp A, B, C, Lower C, D, and Lower D with the total vertical length of, roughly, 600 m (2000 ft). Moreover, other plays as the STACK and SCOOP in the Anadarko Basin and Marcellus and Utica in the Appalachian Basin may benefit from the use of the perforation shots in the seismic imaging.

An advantage that comes from a seismic with larger frequency content is the better definition of the top and bottom of economically interesting layers, decreasing the uncertainty in the path of the laterals. Also, with more research related to the amplitude versus offset (AVO) signature and to the radiation pattern of the different kinds of perforation shot gun systems (Figure 2.6), one can use these high-frequency images to AVO studies and map fluid and lithology lateral variations. There are different set up for some parameters of the perforation shot gun systems as the number of shots per foot and phasing between the charges which need to be considered in AVO studies. These parameters may affect the radiation pattern of the wave phases. Also, although frequencies around 300 Hz were visible in the data, AVO analysis should take into account the lack of frequency below the 80 Hz.

Here, I presented two 2D images which were processed following a VSP walkaway processing flow, but there is no limitation, if a seismic migration algorithm is available, to use the data recorded by different wells to generate a 3D image of the overburden with some correction in the velocity model in order to compensate velocity variations imposed by the hydraulic fracturing. In this context, the more perforation shots, the better is the coverage of the area. Moreover, other VSP seismic processing techniques could be attempted to retrieve more reflected waves. For instance, one could remove the downgoing SV-waves through seismic modeling (instead of muting the data after the SV-wave direct arrival) or use a better deconvolution method. As usual, in most of the research projects, there is room for improvements in the work shown here.

Also, the positions of the observation wells have an important role in the total coverage. The methodology used to calculate the zero-time of the perforation shots in this study requires the horizontal distance between them and the receivers to be small so that the anisotropic effect can be largely avoided and the P- and SV-wave traveltimes be used following the near-hyperbolic approximation, as if they were propagating in an isotropic-layered media. That is a limitation which reduces the area covered by the observation wells.

Regardless the method used to calculate the zero-time of the perforation shots, the best scenario is where the zero-time information is measured instead of calculated. That would give more freedom to the positions of the wells, increasing the imaged area; although other goals as the pore pressure measurement of the reservoir may constrain such positions. Therefore, I propose that the perforation shots zero-time should be routinely measured. They would make easier the tomography and imaging studies without constraining the reach of the wells. Moreover, as the perforation shots have been acquired since the early days of the microseismic technique, it is possible that some companies may already have some data which can be used for tomography and imaging studies.

In this data, P-wave reflections from shots offset 1500 m from the receivers were observed indicating that a relatively large area may be imaged with some adjusts in the geometry. Also, higher values for the number of shots per foot of the perforation shot gun system and the use of cemented completion in the producer may increase the possible maximum offset between source and receivers for this kind of acquisition; although it is necessary to remember of other aspects as the refraction angles, for example.

Another suggestion that would lead to a reduction in the observation wells' cost is

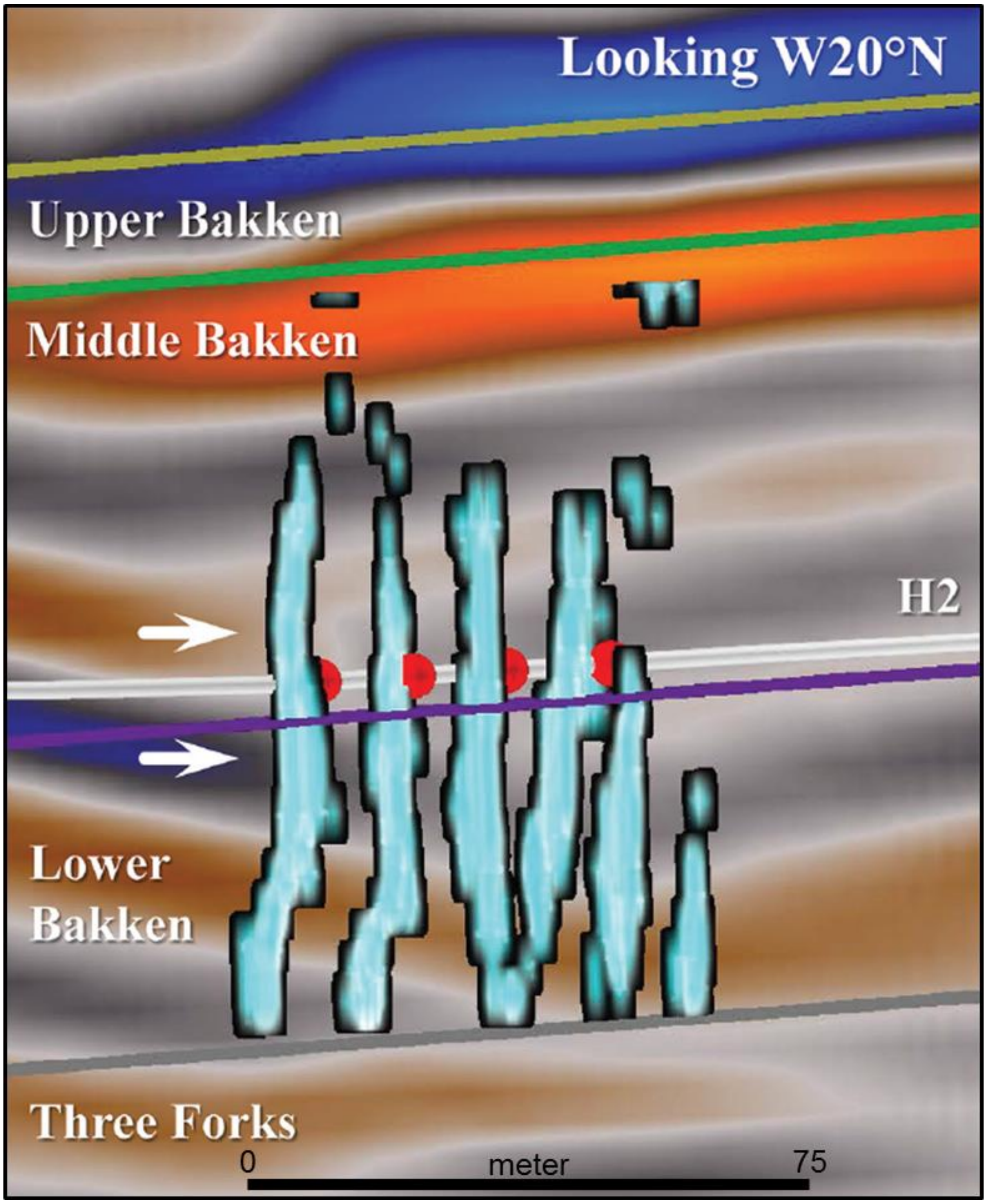


Figure 5.12: Images of holes created by the perforation shots of stage 19 of well H2 imaged by microseismic events triggered 275 m above the reservoir depth during the stimulation of stage 21. The reflected and scattered S-waves from the microseismic events of stage 21 were migrated and the blue geobodies in the image were interpreted as the hole of the perforation shots of stage 19 (modified from Grechka et al., 2017a).

to use them as observation wells in the early phase of their lives and, eventually, convert them into the vertical section of new producer whenever possible. Probably, the

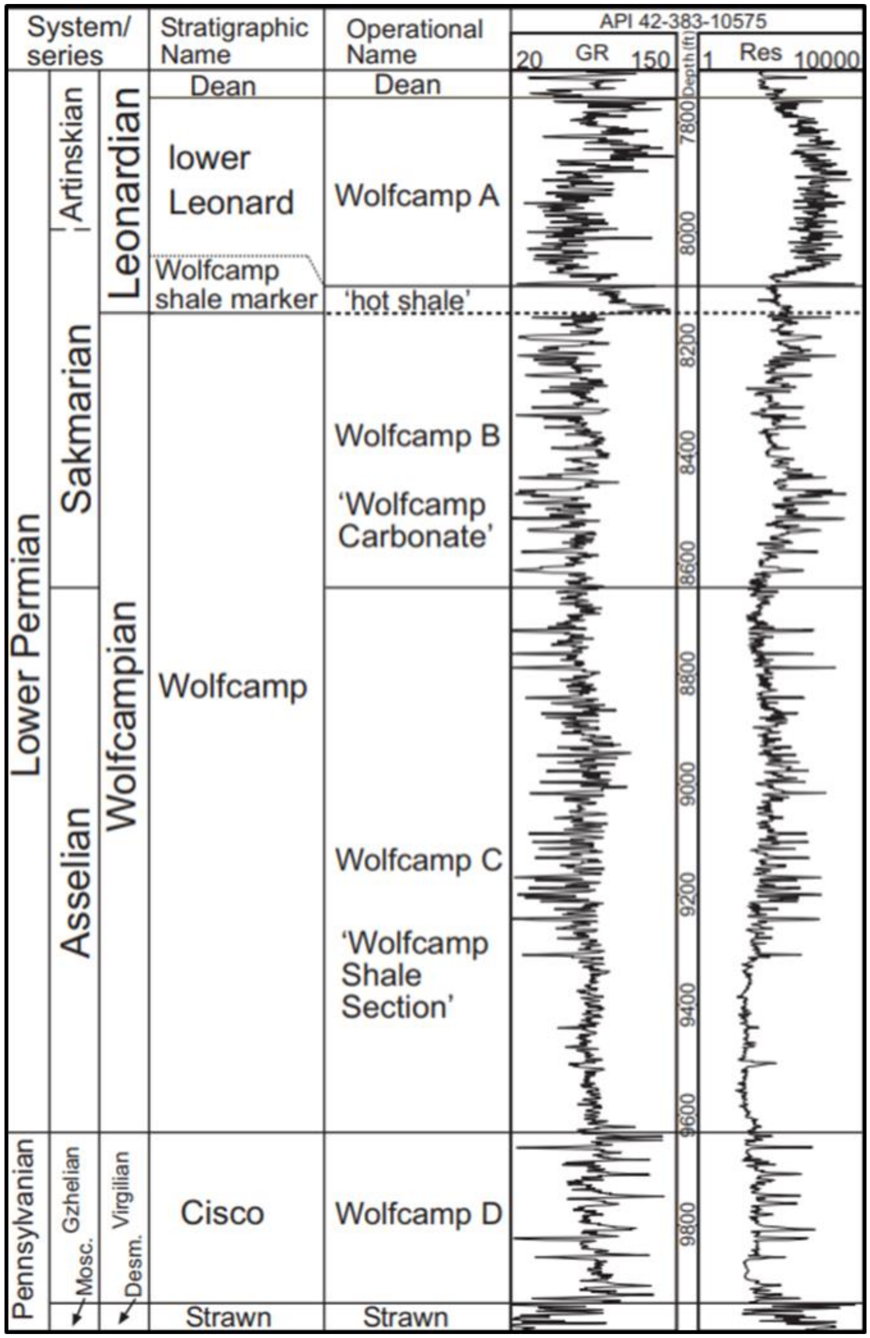


Figure 5.13: The Stratigraphic column of the Wolfcamp Formation in Midland Basin, west Texas. Note the roughly 600 m (2000 ft) of the vertical length of Wolfcamp Formation with potential targets the four different units, i.e., Wolfcamp A, B, C, and D. (modified from Baumgardner et al., 2014).

most cost-effective way to acquire seismic/microseismic data in this scenario is to instrument the observation wells with Distributed Acoustic Sensing (DAS) technology which allows for the seismic data acquisition without stopping the production. With the DAS technology, both observation wells and the vertical section of the producers could be used to acquire seismic/microseismic data.

## 5.4 CONCLUSIONS

The statements below summarize the findings of this chapter:

- Using the P-wave reflections of the perforation shots recordings, I was able to create two 2D seismic sections of the part of the Lodgepole, Mission Canyon, and Charles formations. This includes an illuminated region with more than 600 m in the vertical direction and around 1200 m in the horizontal direction. A VSP walkaway processing workflow was used and the images showed a dominant frequent around 300 Hz.
- Geologic markers interpreted using well logs data were compared to the perforation shots high-frequency images and their synthetics. Reflectors associated with the markers' depths, which were not observed in the 3D surface seismic data, are seen in the high-frequency images, revealing that the use of the perforation shots as seismic sources could be a promising tool for seismic imaging and for interpretation purposes.
- The use of the perforation shots for imaging purposes can resolve thin layers in the overburden and/or underburden. The imaging of these targets can be more easily obtained with changes in the acquisition geometry of the perforation shots. Also, the use of technologies as the measurement of the zero-time of the perforation shots and seismic acquisition using fiber optic sensors (Distribute Acoustic Sensing) can decrease the acquisition cost and allow for larger area imaged, including three-dimensional images.

- Images of other wave modes, as fast and slow S-wave, may be obtained, complementing the usual P-wave data available for interpretation. The perforation shots show a more homogeneous radiation pattern P-wave emission compared to the microseismic events which make them more reliable for imaging purpose. Low velocity zones, commonly seen at shallow depths in seismic surveys with sources and receivers at the surface, is avoided when perforation shots are used as seismic sources. Sources and receivers may also have a better coupling compared to surface seismic acquisitions.

# Chapter 6

# Conclusions and further research

I introduced a novel method to calculate the zero-time values of a set of perforation shots acquired in the Bakken region, North Dakota. The method is based on a hyperbolic approach and the values obtained throughout the minimization process are precise enough to guarantee the accuracy of the results, given that the anisotropy is weak and the offset-to-depth ratio is small (less than 1.5). The errors remain between ± 1 ms; even though the SV-wave is more sensitive to the anisotropy effects. With the zero-time values calculated, the P-wave first arrival and reflections of the P-wavefield emitted by the perforation shots were processed using VSP walkaway, VSP walkaround, and tomography techniques. These techniques allowed for the calculation of the Thomsen anisotropic parameters $\varepsilon$ and $\delta$. The identification of the zones with low P-velocities near the producer well H2, after the hydraulic stimulation, and the imaging of the layers within the overburden were also possible.

The VSP walkaround study used the perforation shots from producer wells H2 and H3. This study yielded the direction N70ºE as the P-wave fastest velocity direction when the perforation shots used in the calculation are the closest shots to the well V3 (smallest offsets). This result is in agreement with the direction of the strike of the natural fractures interpreted in the area. When using the farthest perforation shots available, the fastest P-wave velocity direction is approximately N-S aligned. The N-S direction is roughly the same orientation of the hinge line of the Nesson Anticline, a large structure associated with the depocenter of the Williston Basin. This is the expected direction for extension fractures associated with this anticline. Other study focused on focal mechanism inversion of microseismic events in this area also shown results point to possible structures with this direction.

The VSP walkaway results show values for ε and δ parameters in agreement with the values found by other authors in the area. The ε results show that after the hydraulic fracturing its value was reduced indicating a reduction in the P-velocity. This P-velocity reduction is interpreted as caused by the hydraulic fractures propagation into the Lodgepole and Mission Canyon formations. The δ parameter inversion, apparently, is less stable due to the geometry of acquisition available for the P-wave direct arrival recording. More data points showing larger horizontal slowness variation were necessary to be conclusive regards to the δ parameter interpretation results.

Using the direct P-wave arrivals emitted by the perforation shots of well H2 recorded by wells V1 and V5 and the VSP 3D grid-based anisotropic tomography algorithm, I identified areas near the horizontal section of well H2 with a consistent decrease of the P-velocity after the well had been hydraulically stimulated. I interpreted the P-velocity reduction as the result of the vertical propagation of fractures created during the hydraulic stimulation. The P-velocity anomaly was compared with the production of different stages of well H2 and indicated that the most productive stages are associated with areas where the P-velocity suffered the largest reduction.

In some stages, apparently associated with natural fractures which were reactivated during the hydraulic stimulation, the positive anomaly (lowered P-velocity zone) is interrupted. This natural fracture reactivation is corroborated by the presence of microseismic hypocenters located at 275 m above the Bakken Formation which were triggered during the stimulation of this region. At these stages, the P-velocity anomaly is approximately equal to zero leading to the interpretation that the P-velocity has not changed much after the stimulation. I interpreted that, due the presence of the natural fractures, the hydraulic stimulation of the reservoir in these stages had its effectiveness limited and the hydraulic fluids were conducted to upper levels not contributing to the stimulation of the reservoir.

Using only the P-wave direct arrivals recorded by well V1 in the tomographic study, an area nearby the well V1, characterized by low P-velocity value, apparently is associated with a lower level of hydrocarbons production by well H2 and with microseismic events of higher magnitude. I interpreted the low P-velocity signature of this area as the result of a more pervasive and efficient hydraulic stimulation when H1 was hydraulically stimulated. This more effective stimulation of H1 would be responsible for the lower H2 production in this region whose hydrocarbons would have been already produced by H1. The larger magnitude of microseismic events associated with this area would be, also, a consequence of the fracture network early created by H1 which would be easier to reactivate causing larger events.

Two 2D seismic sections were obtained based on the use of the perforation shots as seismic sources and using a VSP walkaway processing workflow to process the data. P-wave reflections of thin reflectors of the Lodgepole, Mission Canyon, and

Charles formations were retrieved. The size of the illuminated region extends for more than 600 m in the vertical direction and around 1200 m in the horizontal direction. The images showed a dominant frequent around 300 Hz. The high-frequency images obtained from the perforation shots were compared with 3D surface seismic data to evaluate a possible gain in their use for interpretation purposes. For that, geologic markers and synthetic seismic traces derived from the well logs were used in the evaluation of high-frequency images. The high-frequency images have shown reflectors associated with the markers which were not seen in the 3D surface seismic data revealing that the use of the perforation shots as seismic sources could be a promising tool for seismic imaging and for interpretation purposes.

The advantages of the use of perforation shots over the surface seismic for imaging and tomography goals include: seismic source with higher frequency content, the source is close to the target to be imaged, and data acquisition are virtually free to acquire. The source close to the target requires a simpler velocity model to the seismic processing and fewer propagation effects disturb the seismic data. Regards to the costs, since the geophones will be in place to acquire the microseismic data and the perforation is needed in the producers' completion, no extra expenditure is necessary to acquire the perforation shot data. Over the microseismic data, the advantages are: source with larger energy, simpler energy radiation pattern and geometry of acquisition, and timing and location of the source may be measured.

The use of the perforation shots for imaging purposes can resolve thin layers in the overburden and/or underburden. Other oil shale and gas shale plays in the U.S. have already shown economically interesting targets of different ages located in different depths at the same basin. Oil companies with a portfolio that includes stacked-like plays are potential beneficiaries of the use of perforation shots as seismic sources.

Further research is required to clarify how different setups of the perforation gun system change the amount of seismic energy released and its radiation pattern. These setups include the number of chargers per feet and phasing (angle) between them. The impact of the completion methods of the wells, including if they are cemented or uncemented, in the seismic energy released should be examined as well. The producers used in this dissertation were uncemented. Intuitively, it is expected that cemented wells propagate better the S-waves. Also, the perforation shots used in this dissertation show a lack of low frequencies, mainly below 85 Hz, although frequencies up to 600 Hz (P-wave direct arrivals) were recorded. The implications of this unusual frequency bandwidth in the amplitude versus offset (AVO) analysis, for instance, need to be studied.

Below, the most important achievements of this dissertation are stated:

- The zero-time values obtained in the minimization process, following the hyperbolic approach, are precise enough to guarantee the accuracy of the calculated values;
- The VSP walkaround results using the data of the smallest offsets show that the fastest P-wave velocity agrees with the direction of the strike of the natural fractures interpreted in the area;
- The $\varepsilon$ result, derived from the reverse VSP walkaway technique, shows that after the hydraulic fracturing its value was reduced indicating a reduction in the P-velocity traveling parallel to the horizontal plane which is interpreted as caused by the fractures hydraulically propagated into the Lodgepole and Mission Canyon formations;
- Areas near the horizontal section of well H2 with a consistent decrease of the P-velocity, after the well had been hydraulically stimulated, were identified and

interpreted as the result of the propagation of fractures created during the hydraulic stimulation. Stages located close to these areas have shown higher production compared to other stages situated far from the reduced P-velocity region;

- The interruption of the low P-velocity region is associated with natural fractures which were reactivated during the hydraulic stimulation;
- The area nearby the well V1 with low P-velocity signature is interpreted as the result of a more pervasive and efficient hydraulic stimulation when H1 was hydraulically stimulated;
- Two 2D seismic sections of the part of the Lodgepole, Mission Canyon, and Charles formations were processed using the perforation shot data. Each section illuminated a region with more than 600 m in the vertical direction and 1200 m in the horizontal direction. They have shown 300 Hz of dominant frequent.

# Appendix A

# The hyperbolic NMO approach and the orthorhombic anisotropy media

In this appendix, I summarize some concepts which explain how the P- and S-waves propagation change when traveling in an orthorhombic anisotropy medium and how it changes the validity of the hyperbolic normal moveout approach.

## A.1 EFFECTS OF ORTHORHOMBIC ANISOTROPY IN THE HYPERBOLIC EQUATION AND $\mathbf{V_{nmo}}$

The orthorhombic model is characterized by three planes of mirror symmetry mutually orthogonal (Figure A.1). Its stiffness matrix is defined by nine independent elements and is shown below assuming that the symmetry planes coincide with the Cartesian coordinate system:

$$\boldsymbol{c}^{(ORT)} = \begin{pmatrix} c_{11} & c_{12} & c_{13} & 0 & 0 & 0 \\ c_{12} & c_{22} & c_{23} & 0 & 0 & 0 \\ c_{13} & c_{23} & c_{33} & 0 & 0 & 0 \\ 0 & 0 & 0 & c_{44} & 0 & 0 \\ 0 & 0 & 0 & 0 & c_{55} & 0 \\ 0 & 0 & 0 & 0 & 0 & c_{66} \end{pmatrix}. \quad \text{(A.1)}$$

The orthorhombic model is well suited for cases where vertical fractures are combined with a VTI background medium. In fact, the orthorhombic model is reduced to the VTI model in its symmetry planes (for the horizontal layer case); therefore, P- and S-wave can have their anisotropic behavior described by the VTI equations along these planes.

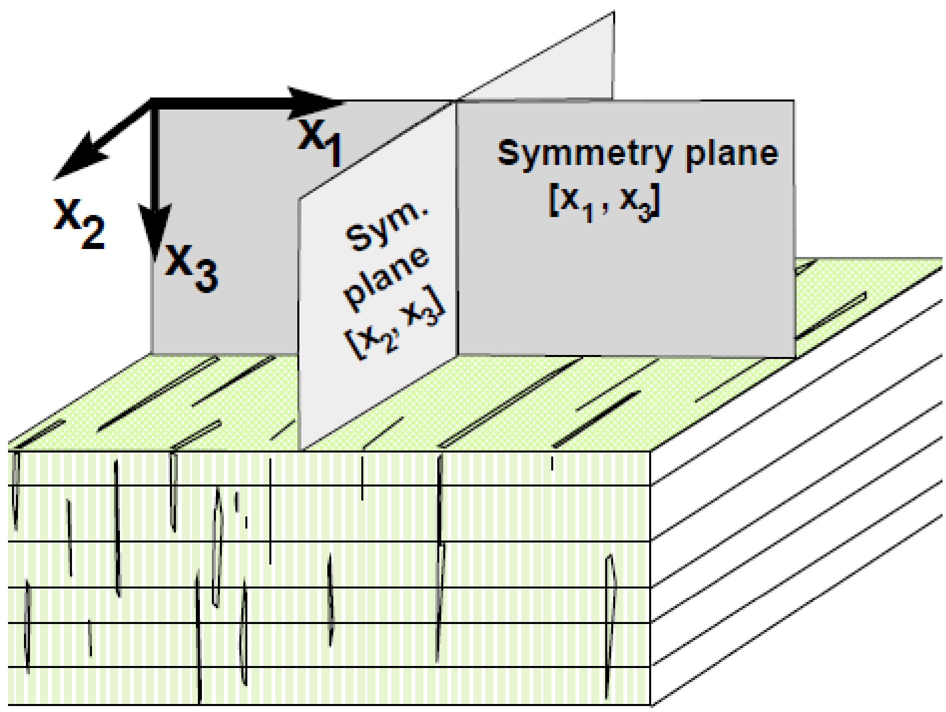


Figure A.1: Model representing the orthorhombic anisotropic case. It is made of one set of vertical fractures embedded in a VTI media background. Three planes of symmetry are present: two planes, one parallel and another perpendicular to the fractures general direction and another parallel to the horizontal layering of the VTI background (modified from Tsvankin, 1997).

The analogy between the VTI and orthorhombic model is clearer when the equivalent notation of the VTI Thomsen parameters are used to describe the orthorhombic model (Tsvankin, 1997). The parameters and vertical velocities are shown below as function of the stiffness coefficients and density $\rho$ (coordinates planes aligned with the symmetry planes of the medium):

- P-wave vertical velocity;

$$V_{P0} \equiv \sqrt{\frac{c_{33}}{\rho}}. \tag{A.2}$$

- S-wave vertical velocity polarized in the $x_1$ direction (refer to Figure A.1 for the directions definitions);

$$V_{S0} \equiv \sqrt{\frac{c_{55}}{\rho}}. \tag{A.3}$$

- VTI parameter $\epsilon$ along the symmetry plane $[x_2, x_3]$;

$$\epsilon^{(1)} \equiv \frac{c_{22}-c_{33}}{2c_{33}}. \tag{A.4}$$

- VTI parameter $\delta$ along the symmetry plane $[x_2, x_3]$;

$$\delta^{(1)} \equiv \frac{(c_{23}+c_{44})^2-(c_{33}-c_{44})^2}{2c_{33}(c_{33}-c_{44})}. \tag{A.5}$$

- VTI parameter $\gamma$ along the symmetry plane $[x_2, x_3]$;

$$\gamma^{(1)} \equiv \frac{c_{66}-c_{55}}{2c_{55}}. \tag{A.6}$$

- VTI parameter $\epsilon$ along the symmetry plane $[x_1, x_3]$;

$$\epsilon^{(2)} \equiv \frac{c_{11}-c_{33}}{2c_{33}}. \tag{A.7}$$

- VTI parameter $\delta$ along the symmetry plane $[x_1, x_3]$;

$$\delta^{(2)} \equiv \frac{(c_{13}+c_{55})^2-(c_{33}-c_{55})^2}{2c_{33}(c_{33}-c_{55})}. \tag{A.8}$$

- VTI parameter $\gamma$ along the symmetry plane $[x_1, x_3]$;

$$\gamma^{(2)} \equiv \frac{c_{66}-c_{44}}{2c_{44}}. \tag{A.9}$$

- VTI parameter $\delta$ along the symmetry plane $[x_1, x_2]$ ($x_1$ can be assumed as the symmetry axis);

$$\delta^{(3)} \equiv \frac{(c_{12}+c_{66})^2-(c_{11}-c_{66})^2}{2c_{11}(c_{11}-c_{66})}. \tag{A.10}$$

The shear-wave splitting phenomenon, in the vertical direction for an orthorhombic and horizontal layer, is described by the fractional difference between $c_{44}$ and $c_{55}$ as follows:

$$\gamma^{(S)} \equiv \frac{c_{44}-c_{55}}{2c_{55}} = \frac{\gamma^{(1)}-\gamma^{(2)}}{1+2\gamma^{(2)}} \approx \frac{V_{S1}-V_{S0}}{2V_{S0}}, \tag{A.11}$$

where $V_{S1} \equiv \sqrt{c_{44}/\rho}$ is the fast vertical S-wave velocity.

The NMO velocity for the orthorhombic media, also, can be described in a similar way as it is done for the VTI media due to the analogy between the models. For the case of a single horizontal orthorhombic layer, P-wave NMO velocity, $V_{nmo,P}$, is characterized by two equations (Tsvankin, 1997):

$$V^{(1)}_{nmo,P} = V_{P0}\sqrt{1+2\delta^{(1)}}, \tag{A.12}$$

$$V^{(2)}_{nmo,P} = V_{P0}\sqrt{1+2\delta^{(2)}}. \tag{A.13}$$

Here the superscript “1” represents the plane symmetry [$x_2$, $x_3$] and “2” is associated with the plane symmetry [$x_1$, $x_3$]. The same analogy is valid for the $S_1$- and $S_2$-wave modes. The velocities along the symmetry planes are given below:

$$V^{(1)}_{nmo,S1} = V_{S1}\sqrt{1+2\sigma^{(1)}}, \tag{A.14}$$

$$V^{(2)}_{nmo,S1} = V_{S1}\sqrt{1+2\gamma^{(2)}}, \tag{A.15}$$

$$V^{(1)}_{nmo,S2} = V_{S2}\sqrt{1+2\gamma^{(1)}}, \tag{A.16}$$

$$V^{(2)}_{nmo,S2} = V_{S2}\sqrt{1+2\sigma^{(2)}}, \tag{A.17}$$

where

$$\sigma^{(1)} \equiv \left(\frac{V_{P0}}{V_{S1}}\right)^2 (\epsilon^{(1)}-\delta^{(1)}), \tag{A.18}$$

$$\sigma^{(2)} \equiv \left(\frac{V_{P0}}{V_{S2}}\right)^2 (\epsilon^{(2)}-\delta^{(2)}). \tag{A.19}$$

Assuming the slow S-wave in the vertical direction polarized in the $x_1$, the vertical $V_{S2}$ is equal to $V_{S0}$ whereas the fast $V_{S1}$ is given by the equation

$$V_{S1} = V_{S0}\sqrt{\frac{1+2\gamma^{(1)}}{1+2\gamma^{(2)}}}. \tag{A.20}$$

The NMO velocity for all pure modes in a single layer of arbitrary strength of anisotropy can be described by the elliptical Equation A.21 introduced by Grechka and Tsvankin (1998)

$$V_{nmo}^{-2}(\alpha) = \frac{\sin^2\alpha}{\left[V_{nmo}^{(1)}\right]^2} + \frac{\cos^2\alpha}{\left[V_{nmo}^{(2)}\right]^2}, \tag{A.21}$$

where $\alpha$ is the azimuth angle assuming the symmetry plane [$x_1$, $x_3$] aligned to the north direction.

The P-wave NMO correction for a single and horizontal orthorhombic media can be performed by a variation of the Equation 2.22 defined by Alkhalifah and Tsvankin (1995) which is a function of azimuth angle $\alpha$ as well:

$$t^2(x,\alpha) = t_{P0}^2 + \frac{x^2}{V_{nmo}^2(\alpha)} - \frac{2\eta(\alpha)x^4}{V_{nmo}^2(\alpha)\left[t_{P0}^2V_{nmo}^2(\alpha)+(1+2\eta(\alpha))x^2\right]}, \tag{A.22}$$

where $V_{nmo}(\alpha)$ is the NMO ellipse velocity (Equation A.21) and $\eta(\alpha)$ is the azimuthally variant version of the $\eta$ which can be calculated by:

$$\eta(\alpha) = \eta^{(1)}\sin^2\alpha - \eta^{(3)}\sin^2\alpha\cos^2\alpha + \eta^{(2)}\cos^2\alpha, \tag{A.23}$$

where

- the parameter $\eta$ in the plane [$x_2$, $x_3$] is:

$$\eta^{(1)} \equiv \frac{\epsilon^{(1)}-\delta^{(1)}}{1+2\delta^{(1)}}, \tag{A.24}$$

- the parameter $\eta$ in the plane [$x_1$, $x_3$] is:

$$\eta^{(2)} \equiv \frac{\epsilon^{(2)}-\delta^{(2)}}{1+2\delta^{(2)}}, \tag{A.25}$$

- the parameter $\eta$ in the plane [$x_1$, $x_2$] is:

$$\eta^{(3)} \equiv \frac{\epsilon^{(1)}-\epsilon^{(2)}-\delta^{(3)}(1+2\epsilon^{(2)})}{(1+2\epsilon^{(2)})(1+2\delta^{(3)})}. \tag{A.26}$$

The accuracy of the Equation A.22 in the symmetry planes is the same seen in the VTI model and it is valid for strong anisotropic media (not limited to the weak-anisotropy case). The same is not true for off-symmetry planes where equation A.22 is valid only for the weak-anisotropy approximation case.

The use of the Equation A.22 in orthorhombic layered media, in the symmetry planes, is possible if the effective $V_{nmo}$ and $\eta$ parameters are used, according to VTI averaging expressions introduced by Tsvankin and Thomsen (1994). For off-symmetry planes, the effective NMO ellipse $V_{nmo}(\alpha)$ can be calculated using the generalized Dix equation (Grechka et al., 1999) and the effective $\eta(\alpha)$ parameter, for cases where the anisotropy is not severe, can be approximated applying the VTI averaging equation for each azimuth as shown below (Al-Dajani and Tsvankin, 1998):

$$\eta(\alpha) = \frac{1}{8}\left\{\frac{1}{V_{nmo}^4(\alpha)t_{P0}}\left[\sum_{i=1}^{N}\left(V_{nmo}^{(i)}(\alpha)\right)^4\left(1+8\eta^i(\alpha)\right)t_{P0}^{(i)}\right]-1\right\}, \tag{A.27}$$

where $V_{nmo}(\alpha)$ is the effective NMO ellipse, and $V_{nmo}^{(i)}(\alpha)$ and $\eta^i(\alpha)$ are the interval parameters in layer $i$, respectively.

Another approach for NMO correction of a single orthorhombic horizontal layer is to use the Tsvankin-Thomsen equation (1994), making the $V_{nmo}$, $A_4$, and $A$ as function of azimuth:

$$t^2(x,\alpha) = t_0^2 + \frac{x^2}{V_{nmo}^2(\alpha)} + \frac{A_4(\alpha)x^4}{1+A(\alpha)x^2}. \tag{A.28}$$

The Equation A.28 can be applied for all pure modes for a single orthorhombic horizontal layer, if the $V_{nmo}$, $A_4$, and $A$ parameters for each mode are known. For $S_1$- and $S_2$-modes, the $V_{nmo}(\alpha)$ can be calculated as it is done for P-wave (Al-Dajani et. al., 1998). The $A$ parameters is given by

$$A = \frac{A_4}{V_{hor}^{-2} - V_{nmo}^{-2}}, \tag{A.29}$$

where $V_{hor}$ is the horizontal velocity which can be obtained for all pure modes as well (Al-Dajani et. al., 1998).

The $A_4$ parameter for P-wave is given by

$$A_4(\alpha) = A_4^{(1)} \sin^4 \alpha + A_4^{(x)} \sin^2 \alpha \cos^2 \alpha + A_4^{(2)} \cos^4 \alpha, \tag{A.30}$$

where

$$A_4^{(1)} = -\frac{2\eta^{(1)}}{t_{P0}^2 \left[V_{nmo}^{(1)}\right]^4}, \tag{A.31}$$

$$A_4^{(2)} = -\frac{2\eta^{(2)}}{t_{P0}^2 \left[V_{nmo}^{(2)}\right]^4}, \tag{A.32}$$

$$A_4^{(x)} = -\frac{2}{t_{P0}^2 \left[V_{nmo}^{(1)}\right]^2 \left[V_{nmo}^{(2)}\right]^2} \left[1 - \sqrt{\frac{\left(1+2\eta^{(1)}\right)\left(1+2\eta^{(2)}\right)}{1+2\eta^{(3)}}}\right], \tag{A.33}$$

where $t_{P0}$ is the two-way zero-offset P-wave traveltime, $V_{nmo}^{(1)}$ and $V_{nmo}^{(2)}$ are given by the Equations A.12 and A.13, and $\eta^{(1)}$, $\eta^{(2)}$, and $\eta^{(3)}$ are given by Equations A.24, A.25, and A.26, respectively.

For $S_1$- and $S_2$-modes, the $A_4$ parameter are given below (Al-Dajani et al., 1998):

$$A_4^{(S_1)}(\alpha) = A_4^{(2)} \cos^4 \alpha + A_4^{(x)} \sin^2 \alpha \cos^2 \alpha, \tag{A.34}$$

$$A_4^{(S_2)}(\alpha) = A_4^{(1)} \sin^4 \alpha + A_4^{(x)} \sin^2 \alpha \cos^2 \alpha. \tag{A.35}$$

The terms $A_4^{(1)}$, $A_4^{(2)}$, and $A_4^{(x)}$ for $S_1$- and $S_2$-mode can be found in Al-Dajani et al. (1998).

Figure A.2 shows the behavior of the quartic term of P, $S_1$, and $S_2$ modes (Equations A.30, A.34, and A.35, respectively) according to the azimuth direction for a horizontal single orthorhombic layer. The symmetry planes coincide with the Cartesian planes. It is possible to see that the quartic term for P-wave shows a more complicated pattern than $S_1$- and $S_2$-wave modes. For the latter modes only around the planes normal to the polarization direction of these modes the anisotropy effect is important (±30º.); nonetheless, for all modes, small values of offset compared to the depth of the target decrease the anisotropy effect.

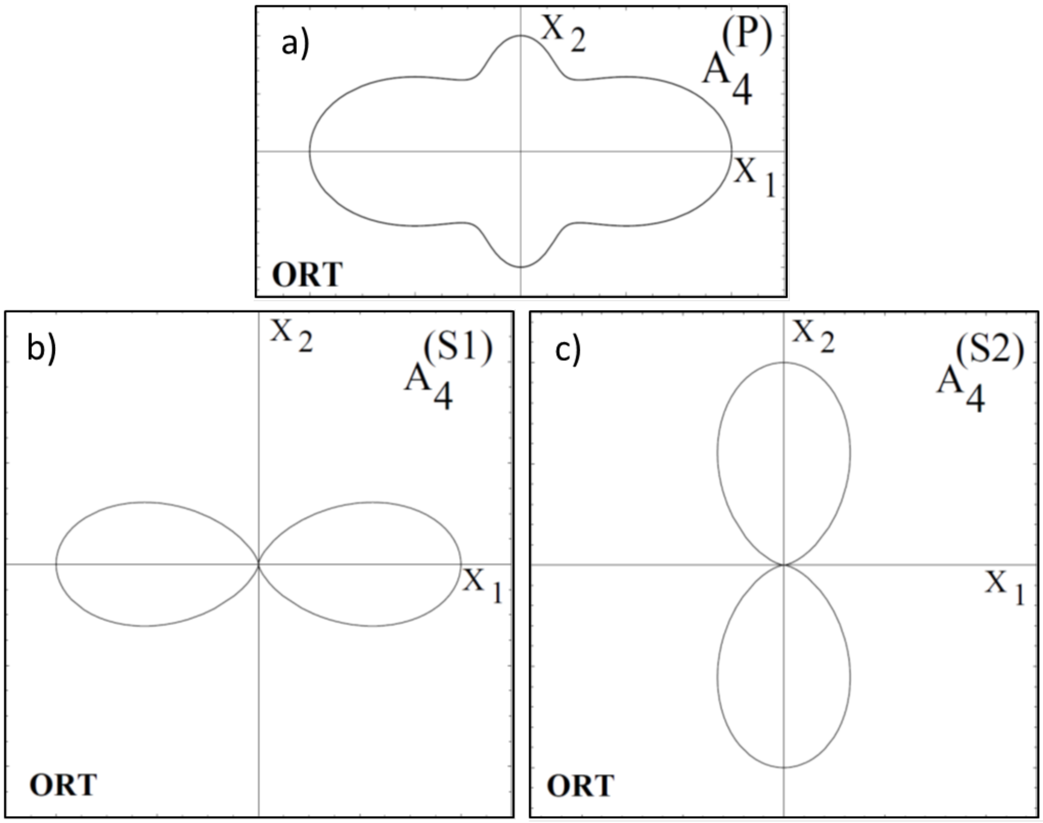


Figure A.2: Scheme (map view) showing the behavior of the quartic term of P-wave (a), $S_1$-wave (b), and $S_2$-wave for a horizontal orthorhombic single layer case towards different azimuth directions. Note that P-wave shows a more complex behavior while the S1- and S2-waves only show expressive anisotropy strength along the planes normal to their polarization directions (±30º). The proximity of the ray propagation to vertical direction diminishes the influence of the anisotropy (modified from Al-Dajani et al., 1998).

# References


Aki, K., and P. G. Richards, 2002, Quantitative Seismology, 2nd edition: University Science Books.

Akram, J., and D. Eaton, 2013, Impact of velocity model calibration on microseismic locations: SEG Technical Program Expanded Abstracts 2013, 1982-1986.

Al-Chalabi, M., 1973, Series approximation in velocity and travel time computation: Geophysical Prospecting, 783-795.

Al-Chalabi, M., 1974, An analysis of stacking, RMS, average and interval velocities over a horizontally layered ground; Geophysical Prospecting, 458-475.

Al-Dajani, A., I. Tsvankin, and M. N. Toksöz, 1998, Nonhyperbolic reflection moveout for azimuthally anisotropic media: 68th Annual International Meeting, SEG, Expanded Abstracts, 1479-1482.

Al-Dajani, A., and I. Tsvankin, 1998, Nonhyperbolic reflection moveout for horizontal transverse isotropy: Geophysics, 63, 1738-1753.

Alkhalifah, T., and I. Tsvankin, 1995, Velocity analysis for transversely isotropic media: Geophysics, 60, 1550–1566.

Baumgardner, R. W., Jr., H. S. Hamlin, and H. D. Rowe, 2014, High-Resolution Core Studies of Wolfcamp/Leonard Basinal Facies, Southern Midland Basin, Texas: AAPG Southwest Section Annual Convention, Article #10607.

Blias, E., 2007, Long-spread-length approximations to NMO function for a horizontally stratified medium: 77th Annual International Meeting, SEG, Expanded Abstracts, 1873-1877.

Crews, C. W., II, 2015, Relating stratigraphy, lithologic facies, and 3D seismic attributes to oil production in Bakken Formation wells, Red Sky area, Williston Basin, North Dakota: M.S. thesis, University of Houston.

Crowley, J. W., A. M. Baig, T. I. Urbancic, and E. V. Lunen, 2015, 4D Tomography and Deformation from Microseismic Data: 85th Annual International Meeting, SEG, Expanded Abstracts, 2537-2541.

Dohmen, T., J. P. Blangy, and J. Zhang, 2014, Microseismic depletion delineation: Interpretation, 2, SG1–SG13.

Dohmen, T., J. Zhang, L. Barker, and J. P. Blangy, 2017, Microseismic magnitudes and b-values for delineating hydraulic fracturing and depletion: Society of Petroleum Engineers, Paper 186096.

DrillingInfo, 2017, The New Permian Benchmark?, https://info.drillinginfo.com/new-permian-benchmark/ accessed 15 May 2018.

Gaswirth, S. B., P. G. Lillis, R. M. Pollastro, and L. O. Anna, 2010, Geology and undiscovered oil and gas resources in the Madison Group, Williston Basin, North Dakota and Montana: The Mountain Geologist, 47, 71-90.

Gerhard, L. C., and S. B. Anderson, 1988, Geology of the Williston Basin (United States portion), *in* Sloss, L. L., ed., Sedimentary cover—North American craton: U.S.: The Geological Society of America, The Geology of North America, D-2, 221–241.

Grechka, V., and I. Tsvankin, 1998, 3-D description of normal moveout in anisotropic inhomogeneous media: Geophysics, 63, 1079-1092.

Grechka, V., I. Tsvankin, and J. K. Cohen, 1999, Generalized Dix equation and analytic treatment of normal-moveout velocity for anisotropic media: Geophysics Prospecting, 47, 117-148.

Grechka, V., Pech, A., and I. Tsvankin, 2002, P-wave stacking-velocity tomography for VTI media: Geophysical Prospecting, 50, 151-168.

Grechka, V., and S. Yaskevich, 2014, Azimuthal anisotropy in microseismic monitoring: A Bakken case study: Geophysics, 79, KS1–KS12.

Grechka, V., Z. Li, and B. Howell, 2016, Relative location of microseismic events with multiple masters: Geophysics, 81, KS149-KS158.

Grechka, V., Z. Li, B. Howell, H. Garcia, and T. Wooltorton, 2017a, High-resolution microseismic imaging: The Leading Edge, 36, 822-828.

Grechka, V., Z. Li, B. Howell, and V. Vavryčuk, 2017, Single-well moment tensor inversion of tensile microseismic events: 87th Annual International Meeting, SEG, Expanded Abstracts, 2746-2751.

Green Plug District, 2013, Hydraulic Fracturing: What is Hydraulic Fracturing?, http://greenplug.nu/wp-content/uploads/2013/05/fracking-explained-in-simple-terms-large.jpg, accessed 15 November 2016.

Halliburton, 2017, Perforation solutions catalog, http://www.halliburton.com /public/lp/contents/Books_and_Catalogs/web/JRC_Catalog/Perforating-Solutions.pdf accessed 10 May 2018.

Havens, J. B., 2012, Mechanical properties of the Bakken formations: M.S. thesis, Colorado School of Mines.

Hendricks, M. L., 1988, Shallowing-upward cyclic carbonate reservoirs in the Lower Ratcliffe interval (Mississippian), Williams and McKenzie counties, North Dakota, *in* S. M. Goolsby and M. W. Longman, eds., Occurrence and Petrophysical Properties of Carbonate Reservoirs in the Rocky Mountain Region: Rocky Mountain Association of Geologists, 371-380.

Huang, H., 2016, Estimating seismic anisotropy: Fluid substitution theory, 3D-printed inclusion models, and multi-component 3D VSP in the Bakken shale: Ph.D. dissertation, University of Houston.

Kent, D. M., F. M. Haidl, and J. A. MacEachern, 1988, Mississippian oil fields in the northern Williston Basin, *in* S. M. Goolsby and M. W. Longman, eds., Occurrence and petrophysical properties of carbonate reservoirs in the Rocky Mountain region: Rocky Mountain Association of Geologists, 381-418.

Kerr, S. D., 1988, Overview: Williston Basin carbonate reservoirs, *in* S. M. Goolsby and M. W. Longman, eds., Occurrence and Petrophysical Properties of Carbonate Reservoirs in the Rocky Mountain Region: Rocky Mountain Association of Geologists, 251-274.

King, G. E., 2010, Thirty years of gas shale fracturing: what have we learned?: Society of Petroleum Engineers, Paper 133456.

LeFever, J. A., 2008, Structural contour and isopach maps of the Bakken Formation in North Dakota: North Dakota Geological Survey, GI-59, 5 map series.

Li, J., C. Li, S. A. Morton, T. Dohmen, K. Katahara, and M. N. Toksöz, 2014, Microseismic joint location and anisotropic velocity inversion for hydraulic fracturing in a tight Bakken reservoir: Geophysics, 79, C111–C122.

Li, Z., Y. D. Su, S. Xu, C. X. Zhuang, and X. M. Tang, 2017, Evaluation of Downhole Hydraulic Fracturing by Acoustic Logging: 87th Annual International Meeting, SEG, Expanded Abstracts, 964-968.

Lindsay, R. F., 1988, Mission Canyon Formation reservoir characteristics in North Dakota, *in* S. M. Goolsby and M. W. Longman, eds., Occurrence and Petrophysical Properties of Carbonate Reservoirs in the Rocky Mountain Region: Rocky Mountain Association of Geologists, 317-346.

Maxwell, S., 2014, Microseismic imaging of hydraulic fracturing: improved engineering of unconventional shale reservoirs: Society of Exploration Geophysicists.

Petty, D. M., 1996, Regional stratigraphic and facies relationships in the Mission Canyon Formation, North Dakota portion of the Williston Basin, *in* M. W. Longman and M. D. Sonnenfeld, eds., Paleozoic Systems Region: Rocky Mountain Section – Society for Sedimentary Geology, 193-211.

Pitman, J. K., L. C. Price, and J. A. LeFever, 2001, Diagenesis and fracture development in the Bakken Formation, Williston Basin: Implications for reservoir quality in the middle member: U.S. Geological Survey Professional Paper 1653.

Pollastro, R. M., L. N. R. Roberts, and T. A. Cook, 2013, Geologic assessment of technically recoverable oil in the Devonian and Mississippian Bakken Formation - Chapter 5 - *in* Assessment of undiscovered oil and gas resources of the Williston Basin Province of North Dakota, Montana, and South Dakota, 2010 (version 1.1, November 2013): U.S. Geological Survey Digital Data Series DDS–69–W.

Rutledge, J., X. Weng, C. Chapman, X. Yu, and S. Leaney, 2016, Bedding-plane slip as a microseismic source during hydraulic fracturing: 86th Annual International Meeting, SEG, Expanded Abstracts, 2555-2559.

Silva, A. A. C., and R. R. Stewart, 2017, Characterizing and imaging hydraulic-fractured overburden layers using perforation shots: 87th Annual International Meeting, SEG, Expanded Abstracts, 2992-2996.

Taner, M. T., and F. Koehler, 1969, Velocity spectra - digital computer derivation and applications of velocity functions: Geophysics, 34, 859-881.

Taner, M. T., S. Treitel, and M. Al-Chalabi, 2005, A new travel time estimation method for horizontal strata: 75th Annual International Meeting, SEG, Expanded Abstracts, 2273-2276.

Thomsen, L., 1986, Weak elastic anisotropy: Geophysics, 51, 1954-1966.

Thomsen, L., 2002, Understanding seismic anisotropy in exploration and exploitation, 2nd edition: Society of Exploration Geophysicists.

Tsvankin, I., 1995, Normal moveout from dipping reflectors in anisotropic media: Geophysics, 60, 268-284.

Tsvankin, I., 1997, Anisotropic parameters and P-wave velocity for orthorhombic media: Geophysics, 62, 1292-1309.

Tsvankin, I., 2005, Seismic signatures and analysis of reflection data in anisotropic media, 3rd edition: Society of Exploration Geophysicists.

Tsvankin, I., and L. Thomsen, 1994, Nonhyperbolic reflection moveout in anisotropic media: Geophysics, 59, 1290–1304

Tsvankin, I., and V. Grechka, 2011, Seismology of azimuthally anisotropic media and seismic fracture characterization: Society of Exploration Geophysicists.

U.S. Energy Information Administration, 2013, Technically Recoverable Shale Oil and Shale Gas Resources, https://www.eia.gov/analysis/studies/worldshalegas/archive/2013/pdf/fullreport_2013.pdf, accessed 19 May 2018.

U.S. Energy Information Administration, 2015, Shale gas and tight oil are commercially produced in just four countries, https://www.eia.gov/todayinenergy/detail.php?id=19991#, accessed 19 May 2018.

U.S. Energy Information Administration, 2016, Map of shale gas and tight oil plays in the lower 48 states of U.S., https://www.eia.gov/maps/images/shale_gas_lower48.pdf, accessed 19 May 2018.

U.S. Energy Information Administration, 2016a, Trends in U.S. oil and Natural gas upstream costs, https://www.eia.gov/analysis/studies/drilling/pdf/upstream.pdf, accessed 19 May 2018.

U.S. Energy Information Administration, 2018, Crude oil and tight oil production estimative in the U.S., https://www.eia.gov/petroleum/data.php#crude, accessed 19 May 2018.

U.S. Energy Information Administration, 2018a, Drilling Productivity Report – April/2018, https://www.eia.gov/petroleum/drilling/archive/2018/04/pdf/dpr-full.pdf, accessed 19 May 2018.

Vernik, L., and X. Liu, 1997, Velocity anisotropy in shales: A petrophysical study: Geophysics, 62, 521-532.

Yang, Y., and M. D. Zoback, 2014, The role of preexisting fractures and faults during multistage hydraulic fracturing in the Bakken Formation: Interpretation, 2, SG25-SG39.

Yuan, D., and A. Li, 2017, Joint inversion for effective anisotropic velocity model and event locations using S-wave splitting measurements from downhole microseismic data: Geophysics, 82, C133-C143.